Fakultät für Physik
Physik Department E18
Nuklearmedizinische Klinik und Poliklinik
Technische Universität München

Development of a PET Insert for Simultaneous Preclinical PET/MR at 7 T

Florian R. Schneider

Vollständiger Abdruck der von der Fakultät für Physik der Technischen Universität München zur Erlangung des akademischen Grades eines Doktors der Naturwissenschaften (Dr. rer. nat.) genehmigten Dissertation.

Vorsitzende:
Univ.-Prof. Dr. Nora Brambilla
Prüfer der Dissertation:
1. Univ.-Prof. Dr. Stephan Paul
2. Univ.-Prof. Dr. Franz Pfeiffer

Die Dissertation wurde am 18.06.2015 bei der Technischen Universität München eingereicht und durch die Fakultät für Physik am 14.12.2015 angenommen.

Abstract

During the last decade, a number of hybrid PET/MRI (positron emission tomography/magnetic resonance imaging) systems has been developed, after in 1997 the feasibility of simultaneous imaging with both systems has been demonstrated by [SCF+97]. This has triggered extended research especially on the PET side towards MRI-compatible system designs, detectors and materials. The MRI introduces challenges not only due to the high magnetic field but also due to the radio frequencies, which can highly affect the PET performance. Vice versa, also the PET may not destroy the MRI signal.

On the detector side, PMTs (photomultiplier tubes) have been the gold standard in PET for decades, but they are not able to operate in a magnetic field. SSPDs (solid state photon detectors) like ADPs (avalanche photodiodes) or their successors G-APDs (Geiger-mode avalanche photodiode, also called SiPM (silicon photomultiplier)) overcome this and are currently the state-of-the art choice for PET/MRI systems.

At the moment, there is no MRI-compatible PET system reported in literature which uses the SiPM technology with a higher magnetic field than 3 T. In this work, a PET insert for a commercially available 7 T preclinical small animal MRI scanner has been developed from the ground up. The development encompassed the investigation of potential detector technologies and scintillators. This work resulted in two further PET prototypes based on latest technologies. Simulation studies were used to identify optimal system configurations and were the basis for system design.

With the PET insert, simultaneous imaging with both modalities could be successfully demonstrated. It is the first insert using the SiPM technology at 7 T together with a single crystal readout. The new concepts have proven themselves and it works without any RF (radiofrequency) shielding.

Contents

1. Introduction

In this chapter, the motivation, principles, challenges and unique features of the research conducted during this thesis are given.
The basic concepts of PET and MRI are widely and excellently covered in existing literature, e.g. in [CD06, HBTV99, CSP12, BTVM05].

1.1. Background, Motivation and Goals

PET is the most sensitive metabolic imaging method available ($\sim 10^{-12}$ mol/L [DBK$^+$14]). Since it does not provide any morphological information, the idea of hybrid imaging together with either X-ray CT (computed tomography) or MRI (magnetic resonance imaging) is the logical consequence. It can provide complementary information about diseases and help with a correct diagnosis.

The **combination of PET with CT** was first proposed by Townsend, Nutt and colleagues in the early 1990s. In 2001, the first clinical PET/CT scanner became commercially available. Its impact on clinical diagnostics was significant, and in 2006 PET-only scanners were no longer obtainable and PET/CT became the standard [Tow09].

Combining **PET and MRI** is technically challenging, since the MRI introduces conditions like the magnetic field (typ. $0.2 - 9.4$ T [DBK$^+$14]) and radio frequencies (42.6 MHz/T) for the H proton [HBTV99]). Nevertheless it promises to be a further improvement for specific applications, since MRI is superior over CT in terms of soft tissue contrast, does not deliver additional radiation dose and also can provide additional functional information, although complementary and with lower sensitivity ($\sim 10^{-5}$ mol/L [DBK$^+$14]) compared to PET. Especially during the last decades with new SSPDs emerging which are insensitive to magnetic fields, intensive research on hybrid PET/MRI has been conducted. Still, especially compared to the number of PET/CT systems, only a small number of PET/MRI systems are commercially available and in clinical use. Many different types of preclinical systems used for research have been developed so far, but only a few types are in clinical routine. An excellent overview of the currently available clinical and preclinical PET/MRI systems can be found in [DBK$^+$14].
The first combined PET and MRI images were acquired with *separate machines* and merged afterwards [PCS$^+$]. This is also the concept of the first clinically available PET/MRI scanner installed in 2010 at Geneva University Hospital [ZOM$^+$11],

for which the patient bed is moved between the two scanners. In the meanwhile also two *fully integrated* whole body PET/MRI systems entered the market (Siemens mMR in 2011 [DFJ+11a], GE Signa PET/MR in 2014 [DKH+14]) which perform a co-registration of both modalities. Another approach is a to design the PET as an *insert* into a commercially available MRI system. This was also the concept for the first simultaneous clinical PET/MRI prototype, designed for brain studies (Siemens brainPET in 2008 [SPS+08, KWH+12]).

The concept of a **PET insert** for research and preclinical imaging offers on one hand the flexibility needed to test new technologies and materials, adapt to different MRI geometries and RF (radio frequency) coils and on the other hand to be able to remove or plug the insert upon requirement for the specific imaging task. The PET insert developed in this work was specifically designed for a preclinical 7 T GE/Agilent Discovery MR901.

The **applications** for the insert developed range from preclinical PET/MRI studies with ^{18}[F]-FDG (fluordeoxyglucose) for mice, rats and rabbits to high contrast tumor imaging with radio-labeled antibody fragments. Especially newly developed tracers labeled with the positron-emitters ^{124}I and ^{89}Zr are of particular interest in the research group [MFL+15]. Another focus is on metabolic studies with hyper-polarized ^{13}C [JMW+12, PLZ+10, SgSJ+14] in combination with ^{18}[F]-FDG.

These applications imply **demands** which are considered in the design and development of the PET insert. Basic points are a spatial resolution of 1 mm for mice studies, a CTR (coincidence time resolution) of < 1 ns, a usability of the whole FOV (field of view) up to 80% for rabbit studies with a spatial resolution < 2.5 mm and a high count rate capability to be able to measure high injected activities without a saturation of the front end. A PET ring composed of single scintillator crystals coupled one-to-one and read out individually by photodetectors (also called SCR, single crystal readout) is an approach, which fulfills the requirements. It improves the positioning accuracy of block detectors and the lower limit of the spatial resolution is defined by the size of the scintillator elements. Also event pile up is unlikely compared to a block detector due to the smaller scintillator volume. In addition, it provides a direct interaction localization and the identification of ICS (inter-crystal scatter) is possible which can increase the absolute system efficiency significantly by more than 30% [RBP+03, TERS+08]. Nevertheless, compared to a block detector the number of detector channels is significantly higher, which increases the complexity of the electronic signal processing and therefore the cost [Zai14]. For this reason, SCR is currently only feasible for small animal scanners with much less detector channels (~ 1000) and smaller ring diameters (~ 10 cm) compared to clinical systems (typ. > 15000 scintillator elements [DFJ+11b, CM09], 60 - 85 cm [RSB07]).

The medical physics group in the Department of Nuclear Medicine at the Technische Universität München has a long tradition in the development of preclinical PET systems based on SCR and SSPDs with the **MADPET** (Munich Avalanche Photodiode PET) series. In the late 1990s, MADPET-I [PBL$^+$98, SMKD11] was the first scanner, based on 96 APDs and LSO (Lu_2SiO_5, Lutetium Oxyorthosilicate) followed by the development of MADPET-II in the early 2000s with 1152 APDs + LSO in a dual layer ring configuration [PBB$^+$01, ZPB$^+$01, Zie05, SMO$^+$07].
Within **this thesis** during the development towards the MRI compatible insert, MADPET3 (cf. ch. 2, p. 23) was developed as a sectorized PET prototype based on SiPMs and LYSO ($Lu_2Y_2SiO_5$:Ce, Lutetium Yttrium Orthosilicate), to evaluate the feasibility of SiPMs for PET with a sub-millimeter spatial resolution [SMK$^+$10, Sch11a, Hoh12]. Based on these experiences, the MRI compatible PET insert MADPET4 has been developed with 2640 SiPMs + LYSO in a dual layer configuration (cf. ch. 6, p. 77). The choice of the matching SiPM for MADPET4 was crucial, therefore also intensive studies on potential SiPMs have been performed (cf. ch. 4, p. 49). Since in 2009 the digital SiPM as a new light detector was released, this novel sensor was evaluated as well in a PET prototype setup with recently developed GAGG ($Gd_3Al_3Ga_2O_{12}$, gadolinium aluminum gallium garnet) scintillators (cf. ch. 3, p. 35).

The **novelties of MADPET4** are its crystal arrangement, the minimal material budget without active electronic components at the front end and thus MRI transparency and its avoidance of any electrical shielding. Also it is the first reported MRI compatible PET insert working at 7 T which is based on SiPMs with a SCR of LYSO.

1.2. Combined PET/MRI

1.2.1. General

Combining PET and MRI for simultaneous acquisition of both modalities is challenging due to the presence of the magnetic field (typ. $0.2 - 9.4$ T [DBK+14]) and RF (42.6 MHz/T for the H proton [HBTV99]). The advantages of an insert such as developed in this thesis are the cost effective access to PET/MRI and that the developed PET can be customized according to the later applications. Especially within our existing infrastructure, no modifications have to be made and the insert is ready for use upon its completion. It can be easily removed within minutes to perform conventional MRI. On the other hand, technical challenges and constraints apply to the insert. Most obvious is the constraint in terms of space, which is a key factor for the design of the insert e.g. for detector and electronics arrangement. The standard equipment of the MRI like e.g. the animal bed and surface coils must still be usable and it should be even possible to remove the insert without changing the bed position. Also the magnetic field may not be disturbed by materials of high magnetic susceptibility. The MRI RF may not be shielded by the PET components while at the same time the RF may not interfere with the PET signal and render it useless. Both modalities must have as little influence on each other as possible.
An overview of different approaches towards PET/MRI system design can be found in [DZ09], a review of the challenges in [VM15].

1.2.2. Technical Challenges

PET Detector Technology The PET detector technologywas the main problem in the development of combined PET/MRI. For decades, photomultiplier tubes (PMT) combined with an inorganic scintillator crystal have been the standard. Unfortunately PMTs are not even able to operate in weak magnetic fields of several mT [Fla08] and in addition are quite bulky with typical diameters of $\sim$ cm and typical lengths of $>$ 10 cm. Only with the development of SSPDs there was a possibility to think further of combined PET/MRI, since SSPDs are not sensitive to magnetic fields. The first SSPD with internal gain and promising for the use in PET was the APD, which became commercially available in the early 1990s. SiPMs as their successors are the latest generation of SSPDs and overcome many of the disadvantages of PMTs and APDs. They have a typical active area and thickness of $\sim$ mm which allows a compact design to have still an acceptable FOV size. More flexibility in crystal arrangement, system design and robustness are also important factors.

Effects of MRI to PET The MRI gradient fields, which are rapidly switching, can induce eddy currents in conductive components of the PET. They can affect the PET signal quality, lead to vibrations and heating up of the components.

Detectors with a high temperature dependency should be regulated or cooled. The RF of the MRI may interfere with the PET electronics and render the signal useless. RF shielding can be introduced, but at the cost of more material inside the bore with potential higher disturbance of the magnetic field, increased eddy currents and heating.

Effects of PET to MRI Inhomogeneities of the magnetic field caused by the PET components inside the bore may result in artifacts in the MR image. In addition, the gradient fields may be affected as well. Therefore if possible only non-magnetic materials should be used. Also the PET components can have RF interference with the MRI signal, especially in case the electronics emits in the range of the MRI frequency. Unshielded cables or the clock frequency of the data acquisition may be possible sources. RF shielding which was already mentioned can help for both modalities.

PET/MRI System Design in this Thesis MADPET4 is a completely new development taking these requirements and limitations into account from the very beginning. It is specifically designed as an insert into the bore of a commercially available 7 T GE/Agilent MR901 for preclinical small animal imaging. Minimal amount of material and no active electronic components inside the MRI bore were one of the main design goals. Together with a digitization of the PET signals outside the MRI bore, the effects on the MRI should be kept as minimal as possible. The PET components were chosen for high performance, compactness, robustness and with the idea, to operate the insert without any additional RF shielding. The system is described in detail starting from sec. 6.5, p. 93.

1.3. Detectors

1.3.1. Requirements

The combination of a photodetector and scintillator (in the following called *detector*) is used in almost all small animal PET systems. The first step is to convert the energy of the gamma-rays (γ) to light in the visible spectrum by the scintillator. Those are preferably materials with high Z (atomic number) and thus a high stopping power. Not all energy which has been deposited in the scintillator is converted into visible light ($\sim$eV range). Typically the energy deposit for generating a single photon in the scintillator is from 20 to 100 eV, resulting in a typical conversion fraction between 0.1 and 0.02 [Zai14]. The γ interaction processes relevant for PET are the photoelectric effect and Compton scattering. Ideally a **scintillator** should have these properties [Kno10]:

- The *scintillation efficiency* to convert the deposited energy into visible light should be high.

- The light yield should be *proportional* to the deposited energy over as wide range as possible.
- *Transparency* to the wavelength of its own emission with as little as possible self-absorption.
- The *rise and decay time* of the light output should be short.
- Good *optical quality*, *producibility* in the desired size and ease of *handling* (ideally non-hygroscopic).
- The *index of refraction* should be matching to the coupled photodetector to ensure good optical transfer from scintillator to detector.

Those secondary photons from the scintillator then have to be converted by the photodetector into an electrical signal. Usually only a fraction of the generated light can be extracted due to geometrical limitations. For PET it is typically in the range of 10 to 30% [Zai14, Vel10] with a photodetector coupled to the end face of the crystal.
The requirements for the **photodetector** are [Zai14]:

- The *QE* (quantum efficiency), which is the efficiency of converting a photon into a photoelectron, should be high.
- The *PDE* (photo detection efficiency), which is the efficiency to detect a photon with the photodetector, should be as high as possible.
- Impinging photons with an energy of ∼eV result upon detection in at most one photoelectron. This means that the number of primarily generated photoelectrons is too small for direct processing. Therefore either internal or external signal *amplification* without degrading the signal quality is needed.
- A time resolution of ∼100 to ∼1000 ps is needed for PET. Since the first single photons emitted from the scintillator define the timestamp, photodetectors must have a *good SPTR* (single photon time resolution).
- The *spectral sensitivity* of the photodetector should match the emission spectrum of the used scintillator.
- An *optical coupling* material is usually a must, since the index of refraction of most scintillators ($n \approx 1.7$-2.2) is higher than for the photodetector ($n \approx 1.4$-1.5) [MS05, RL09].

The properties of both photodetector and scintillator strongly define the performance of the PET system and thus they have to be carefully chosen depending on the application criteria. Regarding the research topics of this thesis, further key demands apply to the detector:

- Energy and coincidence time resolution (CTR) should be as good as possible. Minimum requirements are $\Delta E/E < 20\%$ (FWHM) and CTR < 1 ns.
- *Insensitivity to magnetic fields* is an essential requirement.
- The detector must be *stable in operation*. A low temperature dependency, operation of many detectors with the same voltage and stability over time are required.
- A *high granularity* with a size of the detector elements in the range of (sub)millimeter corresponding to the spatial resolution has to be achieved.
- Since in this work no light sharing between photodetectors is employed but instead every scintillator is *individually coupled* to a photodetector, the active area and package size of the photodetector has to match the scintillator geometry.
- Detectors should deliver a strong signal which can be digitized without further amplification.

This narrows the choices to solid state photodetectors with internal amplification. These are avalanche photodiodes (APD), which established the basis for Geiger-mode avalanche photodiodes (G-APD) used in this thesis. Especially in the PET community, G-APDs are usually called silicon photomultipliers (SiPM). As stated by the Particle Data Group in 2008, the term SiPM should be replaced by PPD (pixelated photon detector) [ADA+08], but it could not establish itself up to now. In addition, other marketing names have been introduced by different manufacturers, e.g. multi pixel photon counter (MPPC, Hamamatsu Photonics K.K. (HPK)) or micro-pixel avalanche photo diodes (MAPD, Zecotek Photonics Inc.). To adapt to the common use in the community, in this work the term SiPM is used.

With the recent approaches to integrate electronics already on the SiPM itself, they are divided into two classes. Either the classical *analog SiPMs*, where the analog detector signal has to be digitized by dedicated readout electronics or the recently developed *digital SiPMs*, where the detector already provides a digital output.
The following concentrates on the scintillators and photodetectors used in this thesis. Excellent overviews about PET instrumentation can be found e.g. in [CD06, BTVM05, Zai14].

1.3.2. Inorganic Scintillators

For PET with the demand of high sensitivity, suitable materials are inorganic scintillator crystals. They have higher effective atomic numbers Z_{eff} and thus

higher stopping power compared to the group of organic scintillators. Detectors for PET have to be optimized for the detection of 511 keV γ-rays. The two scintillator materials used in this work are *LYSO* (Lutetium Yttrium Oxyorthosilicate, $Lu_{1.8}Y_{.2}SiO_5$:Ce) and *GAGG* (Gadolinium Aluminum Gallium Garnet, $Gd_3(Ga,Al)_5O_{15}$:Ce). LYSO is a well-established and widely used scintillator for PET. GAGG is a recently developed scintillator [KPN+12] and of interest due to a higher light yield and better intrinsic energy resolution compared to LYSO. In this work, LYSO is used for MADPET4 because it is MRI compatible and non-magnetic (cf. ch. 6, p. 77). GAGG is magnetic due to its Gd component and therefore is not used for the insert, but it was successfully used for a PET prototype based on digital SiPMs with promising results (cf. sec. 3.2, p. 36). The performance of detectors with LYSO and GAGG of the same dimensions was directly compared using analog and digital SiPMs (cf. ch. 3 and 4, p. 35 and 49).

Both crystals are co-doped with Ce^{3+} as an activator for the main luminescence. This ion is an efficient luminescence centre with a fast response and an atomic number of $Z = 58$. It has one electron in the 4f state that is excited to the empty 5d shell through interaction with radiation. The subsequent de-excitation by emitting a scintillation photon will occur by an allowed 5d to 4f electric dipole transition with a decay time in the range of 20 to 80 ns. [TGGM06, Kno10]
Excellent work about scintillation mechanisms and further PET scintillators can be found e.g. in [Kno10, TGGM06, LAG+06, CD06]

1.3.3. Characteristics of LYSO and GAGG

Interaction of γ-Rays For PET with 511 keV the interaction is either by photoelectric effect or Compton scattering. The probability for either photoelectric effect or Compton scattering depends on the effective atomic number Z_{eff} (cf. fig. 1.1). LYSO has a higher probability for photoelectric effect than GAGG at 511 keV. Photoelectric effect in the scintillator is the desired interaction for PET since all energy is deposited at once and the incoming γ is absorbed, assuring the correct localization of the interaction to the scintillator element. Its probability is roughly proportional to Z_{eff}^m with $m = 3$ to 4 at 511 keV [CD06]. Compton interaction is an undesirable interaction, since the initial photon only deposits part of its energy and changes its initial direction. This may lead to a wrong localization of the detected γ in the PET image, since it is not distinguishable if the Compton scattering happened already before the detection or in the detector. The exponential relationship $I(x) = I(0) \cdot \exp(-\mu_{att} \cdot x)$ describes the photon flux $I(x)$ at a specific thickness x of the medium with $I(0)$ as the incoming photon flux. The linear attenuation coefficient μ_{att} describes the probability per unit distance, that an interaction will occur [CD06]. As an example, the absorption efficiency $(I(0) - I(x))/I(0)$ for LYSO with varying crystal thickness is shown in fig. 1.2.

Basic Properties Table 1.1 lists the properties of GAGG and LYSO. In comparison, also BGO (Bismuth Germanate, $Bi_4Ge_3O_{12}$) and $LaBr_3$ (Lanthanum(III)

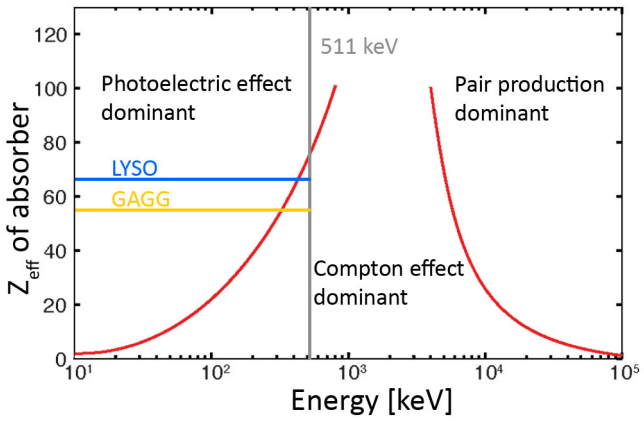

Figure 1.1.: Absorption processes of γ-rays depending on Z_{eff} and their energy. Reproduced and modified from [Eva55].

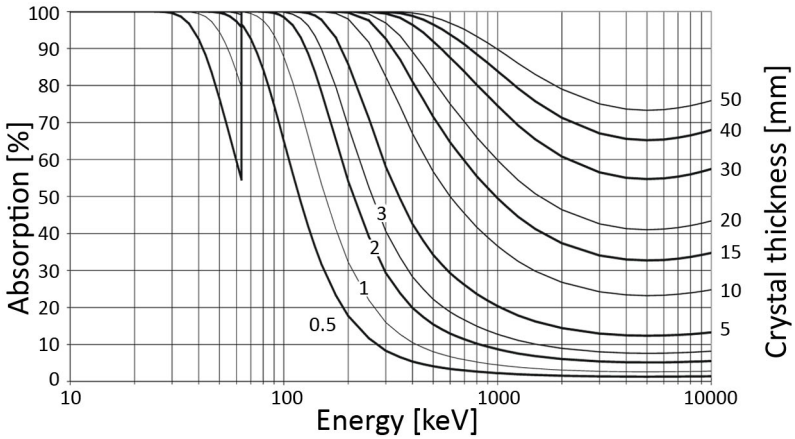

Figure 1.2.: Absorption efficiency $(I(0) - I(x))/I(0)$ of LYSO for different material thickness. Reproduced and modified from [Sai14].

Bromide) are shown. BGO represents the PET scintillator with the highest stopping power which was the material of choice before the emergence of LYSO. $LaBr_3$ on the other hand is the PET scintillator with the best intrinsic energy resolution and the fastest decay time respectively best time resolution. Its disadvantages are its lower Z_{eff} and hygroscopy. GAGG is a material which is still in the development phase, which means that for particular samples the characteristics may slightly vary. The values stated here were provided by the manufacturer [KPN+12]. Its μ_{att} at 511 keV has not been published yet.

Table 1.1.: Properties of the used scintillator crystals GAGG and LYSO, compared to BGO and $LaBr_3$.

	GAGG:Ce [KPN+12]	**LYSO:Ce** [SG04]	**BGO** [Zai14]	**$LaBr_3$:Ce** [Sai09]
Z_{eff}	54	65	74	47
Density [g/cm^3]	6.63	7.1	7.13	5.08
Peak emission [nm]	520	420	480	380
Light yield [ph/MeV]	46000	32000	7000	63000
$\Delta E/E$ at 662 keV [%]	4.7	7.1	9.0 [YCN13]	2.9
Decay time [ns]	88 (92%), 230 (8%)	41	300	16
Best reported CTR [ps]	310 [SSSSZ15]	138 [SvDV+12]	950 [SKM+13]	95 [SvDV+12]
Index of refraction	1.87 [Kam15]	1.81	2.15	1.9
Band gap [eV] [YCN13]	6 - 6.2	6.3 - 6.5	4.96	5.6
μ_{att} at 511 keV [cm^{-1}]		0.86 [KZ11]	0.96 [KZ11]	0.47 [KZ11]
Hygroscopy	no	no	no	yes [ZSW+13]

Light Emission A key feature of a scintillator is its emission wavelength for which the matching photodetector has to be chosen. Figure 1.3 shows emission spectra for GAGG and LYSO upon γ-ray excitation. GAGG shows a more narrow region of emission from about 480 to 620 nm with the peak at about 520 nm. Both crystals show a non-linear light output depending on the incident energy (cf. fig. 1.4). Above 200 keV both show a quite proportional behaviour and usually the non-linearity of the light yield is not taken into account for the calculation of the energy resolution. Usually more severe is the possible non-linearity of the photodetector response, which has to be taken into account to set an accurate low energy threshold in PET.

Intrinsic Self-Radiation LYSO has a significant intrinsic self-radiation which leads to light emission without irradiating it by an external source. This can be easily seen when coupling to a photodetector. In comparison, the intrinsic radiation due to ^{152}Gd (α) in GAGG is negligible and a coupled photodetector only very rarely detects a signal without external irradiation. In LYSO, the ^{176}Lu radioactive isotope is a naturally occuring β emitter (2.599% abundance) which decays with a branching ratio of 99.66% to ^{176}Hf to a 597 keV excited state. This state decays with a three γ-ray cascade of 307 keV, 202 keV and 88 keV. A spectrum measured with a 1 inch diameter by 1 inch long crystal is shown in fig. 1.5. It is possible that a γ can escape the crystal which leads to the four regions in the spectrum. The total rate for the activity is 39 Bq/g. [SG04]

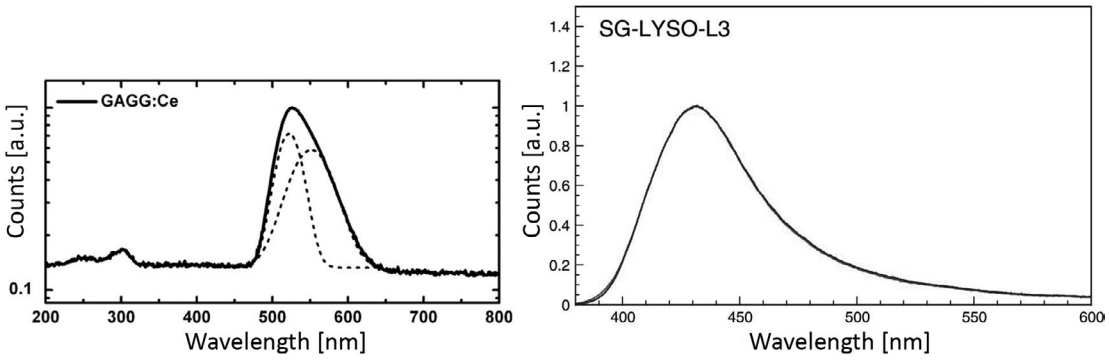

Figure 1.3.: *Left:* GAGG emission spectrum. Reproduced from [ISS+13].
Right: LYSO (St. Gobain) emission upon γ-ray excitation. Reproduced and modified from [ZMZ07].

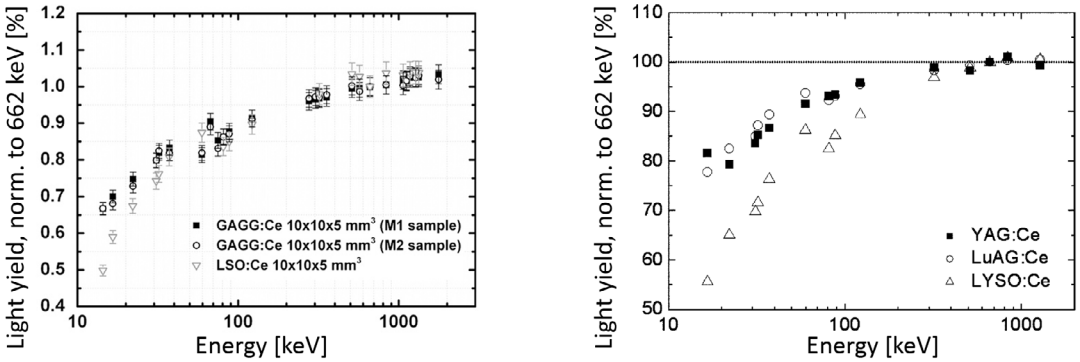

Figure 1.4.: *Left:* Non-linearity of the light yield for GAGG. Reproduced from [ISS+13], with a comparison to LSO.
Right: Non-linearity of the LYSO light yield normalized to 662 keV. Reproduced from [CSM+09], with a comparison to LuAg and YAG scintillators.

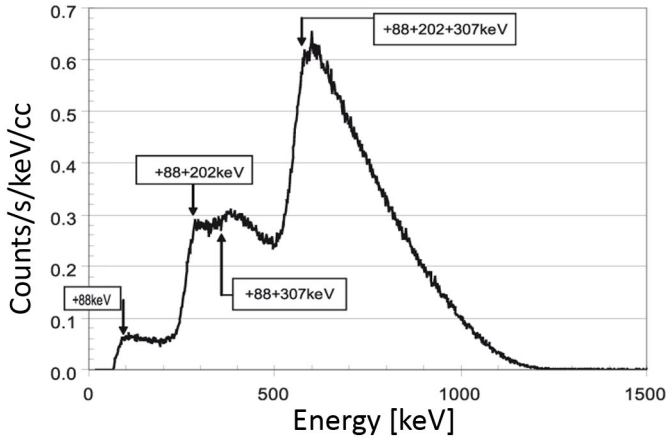

Figure 1.5.: Intrinsic self-radiation of LYSO. Reproduced from [SG04].

1.3.4. Analog Silicon Photomultipliers

SiPMs are actively developed since more than one decade, after the first device was developed by Golovin [Gol99] and Sadygov [Sad98] at the end of the last century.
The basic idea is to operate many small APDs, referred to as *cells* or SPAD (single photon avalanche diode), in Geiger-mode with a parallel connection of all cells. Typical cell pitches range from 10 to 100 μm resulting in about 100 to several 1000 of cells/mm^2. The operation voltage U_{bias} is up to several V higher than the breakdown voltage U_{bd}. The principle of the cell layout and the response to light are shown in fig. 1.6 with a histogram of the number of measured photoelectrons (pe). SiPMs can detect single photons with a very good resolution and have a high intrinsic gain. The reason is the Geiger-mode operation, where a photo-generated primary carrier in the depletion region can trigger an avalanche of carriers by impact ionization. This multiplication is self-sustaining, because of the high field strength secondary avalanches triggered by holes and generated photons are occuring and the cell does not stop the process itself. Therefore, the avalanche has to be quenched either passively by adding a series resistor to each cell or with an active quenching circuit.

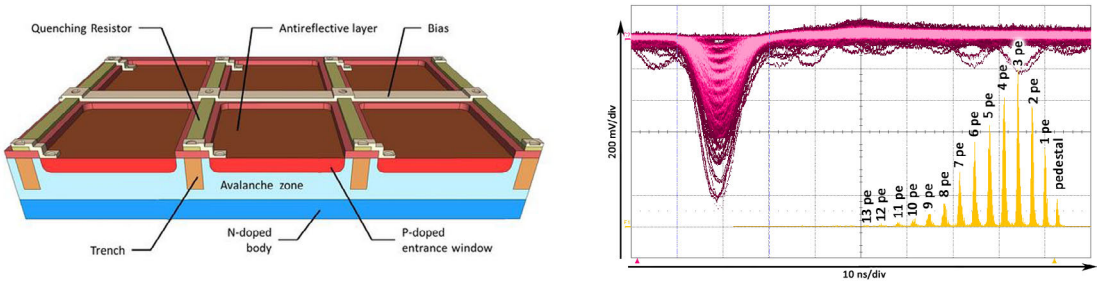

Figure 1.6.: *Left:* Cross section through the microcells of a SiPM. Trenches between cells to reduce optical crosstalk (cf. par. 1.3.4, p. 16) are an optional feature. Reproduced from [KETb].
Right: Oscilloscope screenshot of a SiPM response (*purple*) to single photons. Histogram (*orange*) shows the integrated pulse area, each peak corresponding to the number of fired cells (photoelectrons pe). Used SiPM was a KETEK PM3350. Own measurement.

Properties

Gain Since all cells have the same intrinsic structure, in principle each breakdown of a cell results in a signal with defined shape and amplitude, which is not distinguishable from a signal by any other cell in the SiPM. The amplitude A_{cell} is proportional to the cell capacitance C_{cell} times the overvoltage U_{over} and divided by the elementary charge q_e:

$$A_{\text{cell}} \sim C_{\text{cell}} \cdot U_{\text{over}}/q_e$$

and the total amplitude for cells which fire at the same time is then just the sum of all fired cells $A_{\mathrm{SiPM}} = \sum A_{\mathrm{cell}}$. The gain is typically in the range of 10^5 to 10^7, resulting in a single cell amplitude of several mV at 50 Ω load. With many photons impinging to the SiPM e.g. from a bright scintillator usually used in PET, the amplitude can be easily ~ 100 mV.

Photo Detection Efficiency The PDE is the product of QE, the probability $\epsilon_{\mathrm{Geiger}}$ of incoming photons to trigger an avalanche and the geometrical efficiency (fill factor) $\epsilon_{\mathrm{geometry}}$, which is the ratio of sensitive to total area of the SiPM [Ren09]. It depends on the wavelength λ, U_{bias} and T.

$$\mathrm{PDE}(\lambda, U_{\mathrm{bias}}, T) = \mathrm{QE}(\lambda) \cdot \epsilon_{\mathrm{Geiger}}(\lambda, U_{\mathrm{bias}}, T) \cdot \epsilon_{\mathrm{geometry}}$$

For applications demanding for high dynamic range, the number of cells has to be large enough. This has a direct impact on $\epsilon_{\mathrm{geometry}}$, since every cell needs a bias connection and a resistor which decreases the active area. The best $\epsilon_{\mathrm{geometry}}$ can therefore be achieved with large cells at the cost of limited dynamic range (cf. fig. 1.7). For PET with bright scintillators like LYSO or GAGG resulting in ~ 1000 of photons impinging on the SiPM, a larger number of cells and thus smaller cell size is needed. A good compromise between $\epsilon_{\mathrm{geometry}}$, dynamic range and overall performance is a cell pitch of 50 μm [Pul12], which is offered by all manufacturers on the market. Currently, fill factors range from about 40 to 60% for 50 μm SiPMs [FGS+14a, SGS+14].
The trigger probability $\epsilon_{\mathrm{Geiger}}$ depends on the location in the cell where the primary electron-hole pair is created. Electrons have a higher probability to trigger an avalanche in silicon. According to [OSA72], the probability is highest for the conversion of a photon in the p-layer. Therefore for shorter λ, e.g. for LYSO with its peak emission at 420 nm, a p-on-n type SiPM should be used to reach a higher PDE. Depending on the wavelength, QE can reach about 80 to 90% [Zai14] (cf. fig. 1.8).

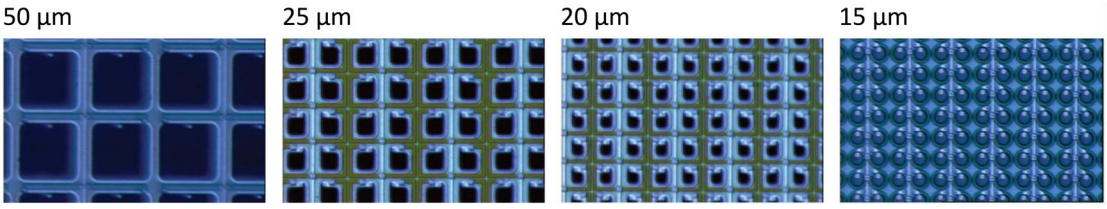

Figure 1.7.: Photomicrograph of different cell sizes of HPK MPPCs. The decrease in $\epsilon_{\mathrm{geometry}}$ for smaller cells is visible. Images from [Mus11].

Dynamic Range and Saturation As shown in figure 1.9, the output of a SiPM is only linear as long as the number of impinging photons N_{ph} times the PDE is significantly smaller than the number of available cells N_{cells}. The following

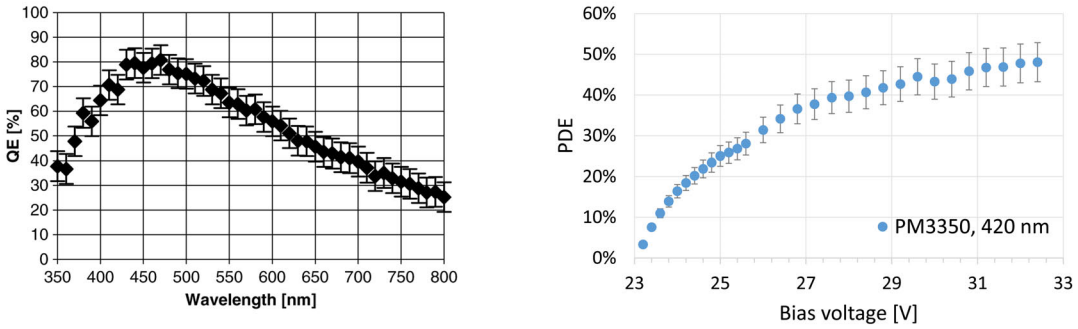

Figure 1.8.: *Left:* Example of QE for a HPK MPPC. Taken from [Ren06].
Right: PDE of a KETEK PM3350 at the peak emission of LYSO ($\lambda = 420$ nm). Own measurement.

equation [VVS+11] describes the number fired cells N_{fired} very well and includes an estimation for the scintillator decay time t_{sc} and the cell recharge time t_{r} [SKM+13]

$$N_{\text{fired}} = \frac{t_{\text{sc}}}{t_{\text{r}}} \cdot N_{\text{cells}} \cdot \left(1 - \exp\left(-\frac{N_{\text{ph}} \cdot \text{PDE}}{N_{\text{cells}} \cdot t_{\text{sc}}/t_{\text{r}}}\right)\right) \quad \text{with } t_{\text{sc}} > t_{\text{r}}$$

For bright scintillators like LYSO and GAGG, this results in a compression of the energy spectrum resulting in an artificial energy resolution better than the reality. A correction based on the described formula is needed for energy resolution comparability between different SiPM and crystal combinations. Also multiple photons hitting a cell at the same time produce only the signal of 1 pe. Figure 1.10 shows a comparison of two energy spectra using a SiPM with 400 cells/mm^2 and one with 15000 cells/mm^2.

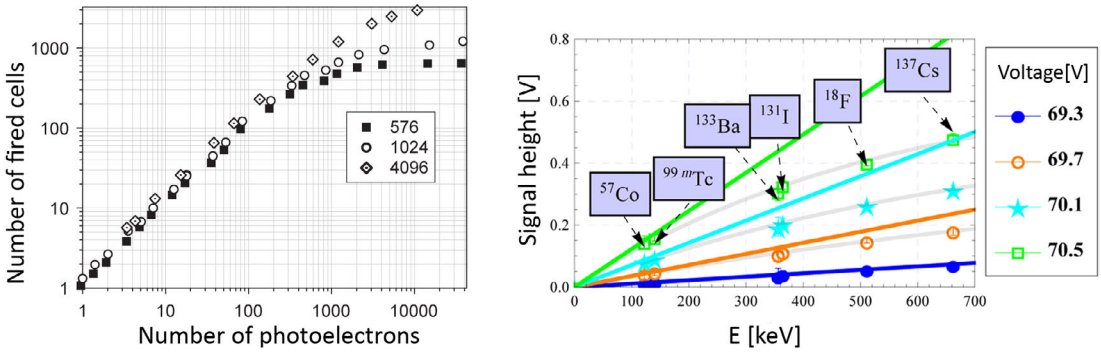

Figure 1.9.: *Left:* Nonlinear response to a 40 ps laser light signal for SiPMs with different number of cells. Reproduced and adapted from [ABB+05].
Right: Nonlinear response when irradiating with different radioactive sources for a SiPM + scintillator (HPK MPPC S10362-11-050C, $1 \times 1 \times 2$ mm^3 LYSO). Gray lines represent an exponential fit to the data points, solid colored lines the theoretical linear response. Reproduced and adapted from [PSV+12a].

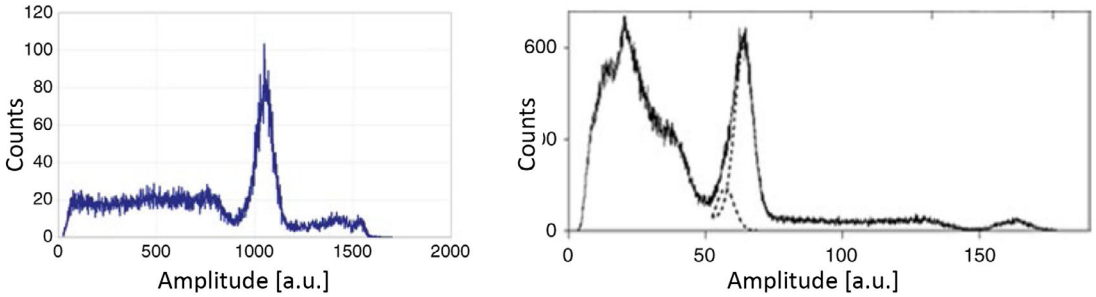

Figure 1.10.: Energy spectrum of ^{22}Na measured with $2 \times 2 \times 12$ mm^3 LYSO coupled to 3×3 mm SiPMs.
Left: Using a SiPM with 400 cells/mm^2 (Photonique/CPTA).
Right: Using a SiPM with 15000 cells/mm^2 (Zecotek MW-3).
Measurements and plots by D. Renker.

Temperature Dependency With changing temperature T, the breakdown voltage U_{bd} of a SiPM will change resulting in a different overvoltage U_{over}. Most parameters of a SiPM depend on U_{over} and therefore it is favorable to use a SiPM with as little change of U_{bd} per K as possible. Depending on the SiPM and the expected temperature variations, an electronic circuit which compensates U_{bd} for temperature changes can be used. The temperature dependency of U_{bd} can be extracted from the relative change in gain, which can be extracted from a single photon spectrum, where it corresponds to the distance between the peaks. Since the gain is proportional to U_{bias}, the interception with the bias voltage axis (cf. fig. 1.11) is U_{bd}. With a measurement at two different temperatures, the temperature coefficient of the breakdown voltage is linearly extracted. Typical values for current SiPMs range from 15 to 60 mV/K [SGS+14]. The temperature dependency of the gain M can be described by the voltage dependent coefficient

$$k_T(U_{\text{bias}}) = \frac{dM}{dT} \cdot \frac{1}{M} \cdot 100\%$$

This value should be as low as possible, since otherwise for PET measurements the photopeak position in the energy spectrum can change already significantly for small temperature changes, with potentially negative effects on the energy resolution due to a broadening of the photopeak. Sensitivity may also be decreased, since usually a fixed lower energy threshold is applied which is no longer correctly set temperature changes. An example is shown in fig. 1.11 with $k_T(U_{\text{bias}}) < 1\%$ for typical $U_{\text{over}} > 10\%$

Dark Count Rate Dark counts are cell breakdowns without photons impinging to the SiPM, instead intrinsically a free charge carrier was generated and triggered the avalanche. This is either caused by thermal generation of electron hole pairs or the field-assisted generation of electrons. The first can be effectively reduced by cooling with a reduction of a factor two in the dark count rate (DCR) by every

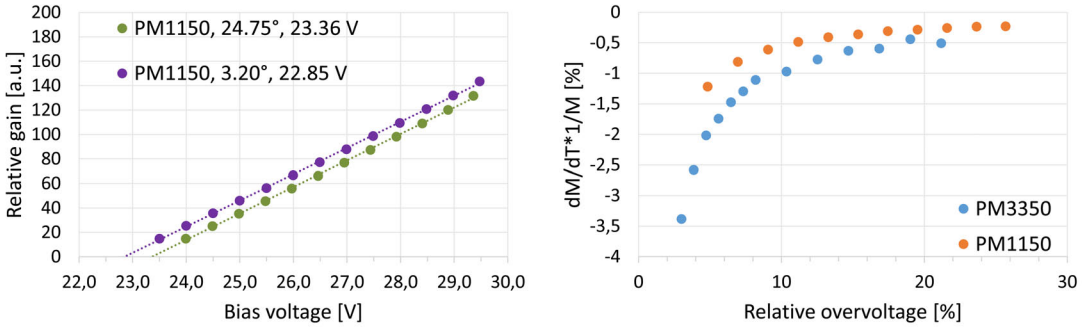

Figure 1.11.: *Left:* Linear behavior of the relative gain vs. U_{bias} at two different temperatures. The intersection with the x-axis correponds to U_{bd}. Measured with a KETEK PM1150 SiPM.
Right: Relative change of the gain with temperature for two different KETEK SiPMs.
Both plots based on own measurements.

8°C drop [Ren06]. The latter can be reduced by a smaller electric field, which is not feasible for every application. Manufacturers can consider this already in the design of the cell, the user can influence it by reducing U_{bias}. Impurities and crystal defects in the silicon have to be avoided, since they are generation-recombination centers. This strongly depends on the production process and its cleanliness. Typical DCR of the latest SiPM generations are about 100 to 400 kHz/mm^2 [Ham14, SGS+14].

Optical Crosstalk During an avalanche, an average of three photons per 10^5 generated charge carries are emitted with a photon energy > 1.14 eV (band gap of silicon) [aLZBM93]. Each of these photons is able to trigger another breakdown in a surrounding cell with a certain cross talk probability (CTP, p_{ct}). This is a stochastic process which results in a misinformation of the number of detected incoming photons. Crosstalk fired cells are indistinguishable from cells fired by impinging photons, since it occurs at the same time (in terms of the possible measurement precision). It introduces an excess noise factor F. Neglecting saturation effects, dark counts and afterpulses, it can be approximated by $F \approx 1 + p_{\text{ct}}$. The probility p_{ct} is extracted from measuring a single photon spectrum only with dark counts. It is defined as the ratio of *dark count events with crosstalk* (> 1.5 pe) divided by the *total number of dark counts* (> 0.5 pe). Operating with less gain lowers p_{ct} but also decreases significantly the PDE and signal quality. A better solution to suppress direct optical crosstalk is to implement trenches working as optical barriers in between the cells (cf. fig. 1.6). Disadvantage is the reduction in fill factor $\epsilon_{\text{geometry}}$ and therefore directly PDE typically by several percent. Altough trenches can significantly reduce direct optical crosstalk, there is still the probability for a crosstalk generated photon to be reflected at the package boundary to trigger another cell.

Afterpulsing and Recovery Time After an initial breakdown of a cell, a certain time later again a breakdown can happen in the same cell. The reason is considered to be a trapping of charge carries of the initial avalanche at lattice defects of the semiconductor [GGCZ03]. This phenomena is called afterpulsing and can be measured as following pulses after the initially triggered pulse. Since with the breakdown also the voltage across the cell drops, each cell needs a certain recharge time t_r to fully reestablish the electric field. In case an afterpulse (or another incoming photon) induces again a breakdown during this recharge time, the amplitude is less than 1 pe. Afterpulsing can be a severe problem in single photon measurements e.g. with a longer measurement gate of $\sim$100 ns to $\sim \mu$s since it falsifies the number of detected photons. For PET with bright scintillators, usually afterpulsing is not the most critical parameter. More important is a short recovery time, which is the time needed to reestablish the electric field of a fired cell. It is governed by the RC constant of a cell and typically measured from the single cell pulse as the decay time from the pulse maximum to $1/e$. A long t_r enhances the saturation causing a less linear response with negative effects on the energy resolution. Typical values range from 10 to 150 ns for currently available SiPMs [OOY+07, SGS+14].

Single Photon Time Resolution SiPMs are expected to have a good time resolution of $\sim$100 ps even for single photons due to their fast avalanche creation (several μm active layer) and a robust signal. For a comparison of different SiPMs, the single photon time resolution (SPTR) is measured. It is the timing when exactly one cell has fired after illuminating with a fast enough light source (typically a laser with several 10 ps FWHM). The main contributions to the time jitter are the lateral spread of the avalanche and fluctuations in the avalanche development itself. The vertical avalanche buildup contributes only very little [Ren06]. Results for the SPTR of several SiPMs is shown in fig. 1.12. It can be seen that for devices with the same cell properties but larger active area the SPTR gets worse. The reason is the larger capacitance caused by the longer connection lines to the cells.

Analog SiPMs in this Thesis Analog SiPMs with an active area of 3×3 mm^2 (PM33 series, manufactured by KETEK, Munich) have been characterized and their performance was evaluated with LYSO and GAGG regarding the use in PET (cf. sec. 4, p. 49). There also the methods to measure the SiPM properties introduced in this chapter are described. The results were compared with other publications of SiPMs manufactured by HPK, SensL and AdvanSiD. Based on these results, SiPMs with an active area of 1.2×1.2 mm^2 (PM11 series, KETEK) have been evaluated specifically for the demands of MADPET4.

The choice of the matching SiPM is a crucial decision to realize the design of MADPET4. The KETEK SiPMs were of specific interest, since they fulfill the demands of the insert in terms of high gain, low temperature dependency, matching package size and finally price per unit. At the time of their purchase,

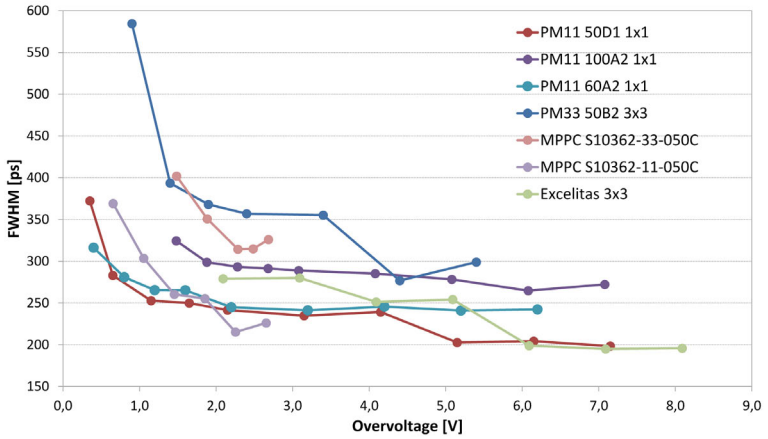

Figure 1.12.: SPTR of SiPMs with different sizes of active area and cells. Devices from KETEK (PM), HPK (MPPC) and Excelitas have been measured. All data from own measurements.

these were unique features that no other manufacturer could provide.

1.3.5. Digital Silicon Photomultipliers

In general, each cell in an analog SiPM shows an intrinsic binary characteristic, namely that either a cell does not break down or it breaks down with a certain charge released. During the last years there have been efforts to implement electronics directly on cell level to sense the breakdown. These so called digital SiPMs were first published by Philips Digital Photon Counting in 2009 [FPD+09, FPDZ10]. During the last years, other groups also started developing digital SiPMs with different approaches of electronics implementation [MC13, MJC14, TLB+15], but these are still in the characterization phase of the first chips. A general drawback of electronics implementation on cell level is the diminishing of $\epsilon_{\text{geometry}}$ and therefore PDE.
Philips markets their sensors as digital photon counters (DPC) and in 2012 they had a commercially available technical evaluation kit (TEK) with up to 4 DPCs. Up to now Philips is the only manufacturer on the market with a digital SiPM which has been tested successfully to work for PET [DRT+12, METV12, WWD+14, SSSSZ15] and has been fully characterized [SSSZ15]. The DPC technology is used for the clinical Philips *Vereos Digital PET/CT* with a system CTR of 345 ps employing time of flight (TOF) information. It was introduced to the market in 2014.

Digital SiPMs in this Thesis A PET prototype based on DPCs has been set up. A detailed introduction to the sensor and the DPC working principle is given within that context (cf. sec. 3.2, p. 36). A characterization study of the DPCs

has been published together with my colleague I. Somlai-Schweiger (first author) [SSSZ15] and is therefore not included in this thesis.

1.4. Readout Electronics

The overall performance of a PET system is not only defined by the choice of scintillator and photodetector, but also the readout electronics attached. Most important is that it may first not limit the intrinsic detector performance and second not the performance of the whole PET system e.g. in count rate capability. The required output for every event is the time stamp, the energy and the channel number for the localization of the interaction. The electronics should be scalable to read out a large number of channels and work without dead time. Ideally, the amount of data is already minimized e.g. by setting a lower energy threshold to dismiss unwanted events. While in the prototyping stage, some demands may be sacrificed for more flexibility and better adaptation to different detectors. There the choice was to use an SADC (Sampling Analog to Digital Converter) developed by the Physics Department E18 of TU München. It is configurable for the use with different detectors.
Once the detector is defined, usually a more specific development exactly for that type of output signal is the better choice in terms of performance and power consumption. Typically it also reduces the cost for the readout electronics, especially when a large number of channels has to be processed. The suitable choice for MADPET4 was a TOT ASIC (Time-over-Threshold Application Specific Integrated Circuit) specifically developed for the used SiPMs by collaborators from the Bioengineering Department at University of Tokyo [Ori14b, OST12]

1.4.1. Sampling Analog to Digital Converter

The SADC module (cf. fig.1.13) is a 6U (height units, 1U = 1.75 inch = 44 mm) VME (Versa Module Eurocard) card and provides 32 differential analog input channels. All 32 inputs are independently amplified and then digitized by 10 bit ADCs with a sampling rate of 80 MHz. Each SADC is equipped with 3 FPGAs (Field Programmable Gate Array). Two perform data buffering and signal processing for 16 channels each. They extract the timestamps of the events and the energy information by the determination of the pulse maxima. The processed data of both FPGAs is then combined in a third link control FPGA and transmitted to the USB interface card via the parallel back plane interface. A J2-USB card (J for jack, 2 refers to the connection to the second VME plug) is attached (cf. fig.1.14) to each SADC. To get a common clock bus, the master SADC with ID0 is equipped with a 40 MHz quartz, from which the 80 MHz sampling rate is derived. This clock signal is distributed to the two other slave SADCs with ID2 and ID3. The SADC module features a configuration channel for programming the firmware of both FPGAs and setting registers to parametrize and control the

firmware, e.g. invert the input signal or set individual channel thresholds, using a C++ based command line program. [Sch09]
Three SADCs with in total 96 ch are used for the readout of MADPET3 (cf. ch. 2, p. 23) and for the first tests with two modules of MADPET4 (cf. ch. 6, p. 77). More detailed information about the SADCs can be found in [Man10] and [Sch09].

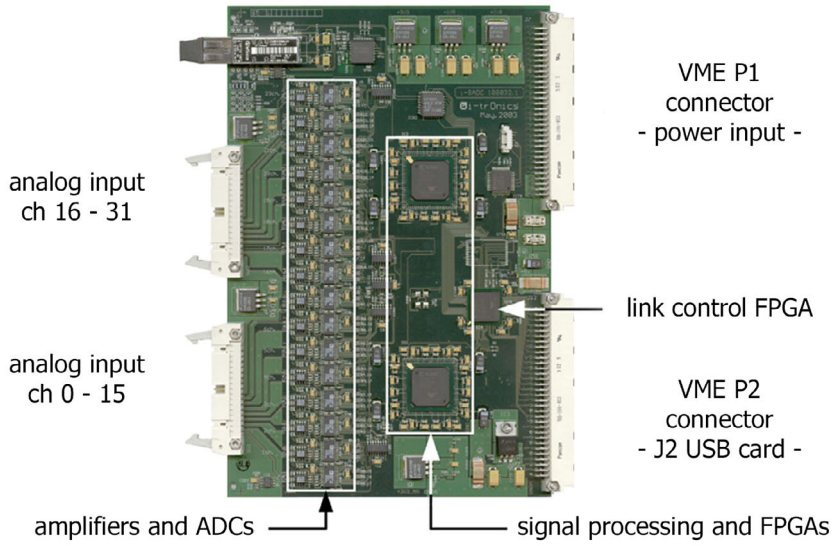

Figure 1.13.: Sampling ADC VME module. Reproduced and modified from [Man10].

1.4.2. Time-over-Threshold ASIC

ASICs are electronic devices which are customized for a particular use. Such a chip is not programmable anymore in contrast e.g. to an FPGA. In this work, an ASIC with TOT functionality has been used as a potential readout for the MADPET4 PET insert. Since the pulse shapes for the combination of SiPMs with scintillators as used for PET are well known, the basic idea is to measure energy and time information by the pulse crossing a fixed threshold. As shown in fig. 1.15, the time stamp of an event is then assigned to the first crossing of the threshold while the energy information is acquired by the time interval in which the pulse is above the threshold. The result is a digital output from which the time stamp (change to high level) and energy (time on high level) can be extracted. Advantages of this approach are a more simplified electronics design, only TDCs (Time to Digital Converter) as a logic implementation, and less power consumption than conventional ADC based readouts. Disadvantages are the non-linearity of the energy information and the compromise between best timing and energy resolution given by the threshold, since changing the threshold always impacts both.

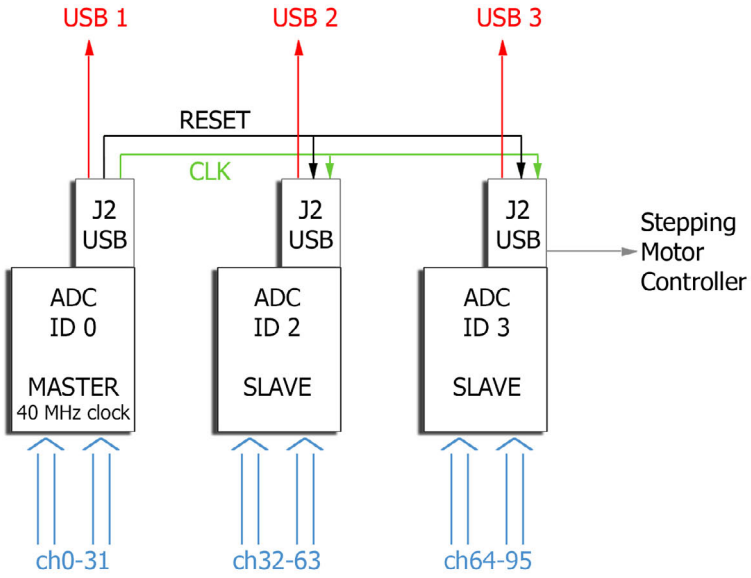

Figure 1.14.: Schematics of the interconnection of the three SADCs and the J2-USB cards. One J2-USB card additionally operates the stepping motor controller. Taken from [Sch09].

A potential readout of the ASIC output is currently under development. A schematics can be found in fig. 1.16. The ASIC has 48 parallel input channels terminated with 50, works with a supply voltage of 3.3 V, has a power consumption of < 3 mW/ch, has a bias regulation of 2.5 V and a die size 2.9×3.3 mm^2.

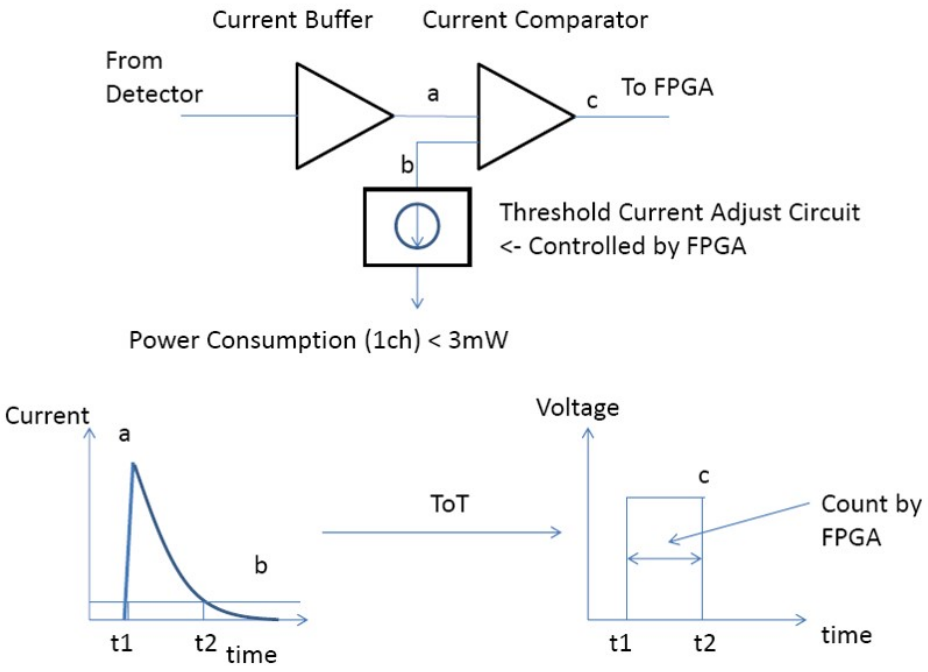

Figure 1.15.: Principle of operation for the TOT ASIC [Ori14a].

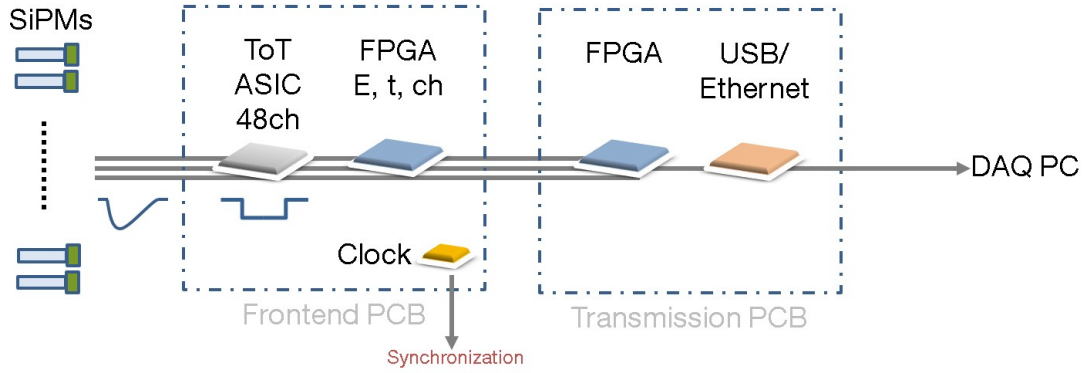

Figure 1.16.: Schematics of the SiPM readout with the ToT ASIC.

2. MADPET3: A Sub-Millimeter-Resolution PET Scanner Prototype based on Single LYSO Crystal Readout by SiPMs with MLEM Reconstruction

This chapter has been published as
Schneider, F. R., Hohberg, M., Mann, A. B., Paul, S., Ziegler, S. I. (2015). A Submillimeter Resolution PET Prototype Evaluated With an ^{18}F Inkjet Printed Phantom. Nuclear Science, IEEE Transactions on, vol.62, no.5, pp.2043-2047. doi: 10.1109/TNS.2015.2461517

Abstract: This work presents a submillimeter resolution PET (Positron Emission Tomography) scanner prototype based on SiPM/MPPC arrays (Silicon Photomultiplier/Multi Pixel Photon Counter). Onto each active area a $1 \times 1 \times 20$ mm^3 LYSO (Lutetium-Yttrium-Oxyorthosilicate) scintillator crystal is coupled one-to-one. Two detector modules facing each other in a distance of 10.0 cm have been set up with in total 64 channels that are digitized by SADCs (Sampling Analog to Digital Converters) with 80 MHz, 10 bit resolution and FPGA (Field Programmable Gate Array) based extraction of energy and time information. Since standard phantoms are not sufficient for testing submillimeter resolution at which positron range is an issue, a ^{18}F inkjet printed phantom has been used to explore the limit in spatial resolution. The phantom could be successfully reconstructed with an iterative MLEM (Maximum Likelihood Expectation Maximization) and an analytically calculated system matrix based on the DRF (Detector Response Function) model. The system yields a coincidence time resolution of 4.8 ns FWHM, an energy resolution of 20% - 30% FWHM and a spatial resolution of 0.8 mm.

2.1. Introduction

The combination of PET and MRI (magnetic resonance imaging) introduces technical challenges caused by the high magnetic fields and the radiofrequency of the MRI. This calls for photo detectors able to work under such adverse circumstances. Avalanche Photodiodes (APD) are known to operate in high magnetic fields, but have small intrinsic gain and therefore preamplifiers and electronics inside the MRI are needed. The first commercially available and fully integrated PET/MRI system is based on APDs. It allows simultaneous data acquisition of both modalities [DFJ+11b].
SiPMs (Silicon Photomultiplier) are the next evolution step which overcome the APD's disadvantage of low gain and thus the need for preamplification directly after the signal creation. They are composed of many APD cells operated in Geiger mode whose charge sum forms the detector signal resulting in a typical SiPM gain in the range of 10^5-10^7 [BMR06]. SiPMs allow to build even more compact systems with higher granularity and higher spatial resolution. The first clinical PET/MRI with SiPMs has been presented in 2014 [DKH+14]. With appropriate readout electronics, SiPMs are suitable for time of flight (TOF) measurements since they show an intrinsic time resolution for single photons down to 80 ps FWHM [GAD+13] and a CTR (coincidence time resolution) of 214 ps FWHM using $3.0 \times 3.0 \times 20.0$ mm^3 LYSO:Ce coupled to Hamamatsu MPPC S10362-33-050C [YYD+13].
The motivation for the prototype was the future development of an MRI compatible small animal PET insert based on SiPM technology in our group [SSS+14]. It has been the first step towards the insert by using the possible detector combination of SiPMs with LYSO for high resolution PET, one-to-one coupled crystals and no preamplifiers at the front end.

2.2. Materials and Methods

In this work a PET prototype based on SiPMs and LYSO with submillimeter resolution is presented. It consists of two opposing detector modules with in total 64 detector channels. The phantoms are rotated in 12 steps of 15° to cover the missing projections and emulate a ring with 24 modules (cf. fig. 2.1). Two SADCs (Sampling Analog to Digital Converter) extract amplitudes and timestamps of the detector signals. The data stream is written to a Linux PC via USB where it is sorted into a ROOT [ROO11] tree as basis for further processing and the image reconstruction.
To evaluate the spatial resolution in the order of the positron range, phantoms printed with ^{18}F labeled ink have been used as proposed in [SBP+05, SBA+08].

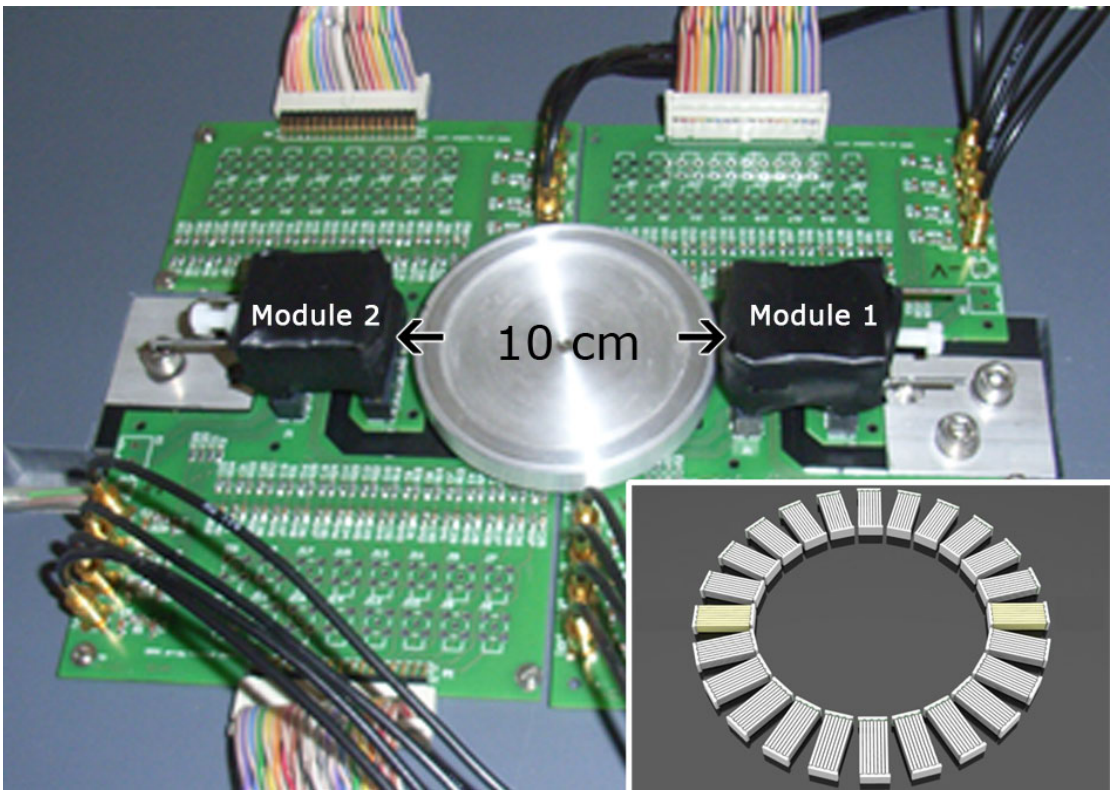

Figure 2.1.: The PET scanner prototype with two detector modules facing each other and a rotating table in the center of the FOV. The black cables supply the bias voltage, the ribbon cables route the signals into the SADCs. *Insert:* Illustration of the detector positions achieved by rotating the phantom to emulate a full ring.

2.2.1. Detectors and Scintillators

For the detector prototype, monolithic MPPC arrays have been used, custom designed by Hamamatsu (cf. fig. 2.2) based on their MPPC S10984-050P [Ham10]. The active area of each pixel is 1×1 mm^2 with a cell pitch of 50 μm and 400 cells/mm^2. To protect the wire bonds of the MPPC, the whole array is covered uniformly with epoxy with a thickness of 250μm. The pixels show a variation of 3% in collected charge between single pixels and 0.9% variation between single cells of one pixel [Pul12]. They are all operated at the same bias voltage of 70.5 V with always one row of 4 pixels sharing one bias supply channel. The characterization of the MPPC arrays can be found in [FPH$^+$12]. The wire bonds do not allow a very dense packaging of single pixels close to each other, but placing 4 pixels in a row of 1×4 mm^2 with no dead space in between is possible. The crystal array was produced by Sinocera (Shanghai, China) so that a single LYSO crystal with $1 \times 1 \times 20$ mm^3 is coupled one-to-one to each pixel representing a single detector channel. The distance between the pixel rows equals a crystal row so that the crystal columns can be read out alternatingly from front- and backside

(cf. fig. 2.3). It opens the possibility to pack the crystals as tight as possible together with minimal dead space in between. $BaSO_4$ (Barium Sulfate) with a thickness of 0.25 mm is the reflector material between the crystal columns while the crystals per row have no reflector in between. A thin layer of optical grease has been used as coupling material.
In one module one of the outermost detector columns (4 ch) broke during initial tests. One column always shares a common bias connection via one pad, which is most likely not well soldered. This limits the field-of-view (FOV) between the two modules. The 8 crystal columns cover 9.75 mm and 7 columns cover 8.5 mm. So the effective FOV width in the central slice between the modules reduces to $(9.75 + 8.5)/2$ mm $= 9.125$ mm with a height of 4 mm.
The SADCs extract the energy information based on pulse height detection. The time stamp is based on a digital implementation of a CFD (constant fraction discriminator). Each signal is first independently amplified and then digitized by 10 bit ADCs on the SADCs with a sampling rate of 80 MHz. In total two SADCs (64 ch) with a common clock are used and each of them is connected via USB 2.0 to the readout computer. Further detailed information regarding the SADCs can be found in [Man10]. They also have been previously used in a setup for PET described in [SMK+11].

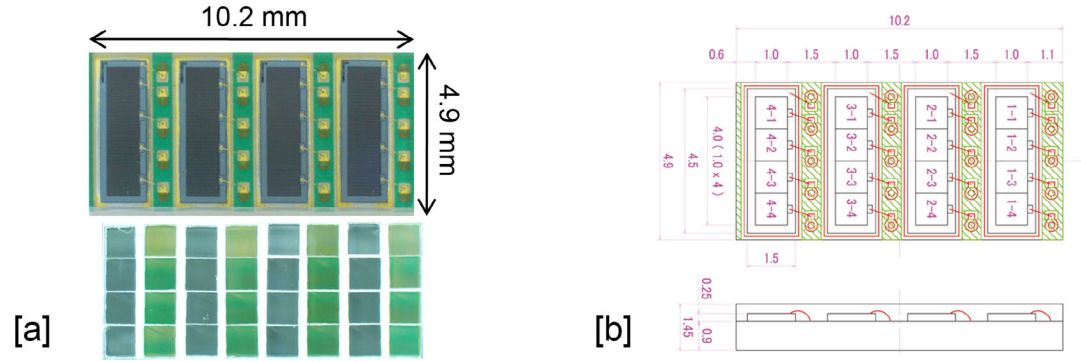

Figure 2.2.: **[a]** *Top:* MPPC array with 16 channels of 1.0×1.0 mm^2 pixels arranged in 1×4 strips. The strips are arranged such that every second row of the LYSO array is read out. Crystal rows are read out alternatingly from top and bottom of the LYSO array. *Bottom:* LYSO array with single crystals of $1.0 \times 1.0 \times 20.0$ mm^3 and $BaSO_4$ reflector.
[b] Schematic of the MPPC array provided by Hamamatsu.

2.2.2. Image Reconstruction

An iterative reconstruction based on MLEM (Maximum Likelihood Expectation Maximization) has been implemented. Using Monte Carlo generated system matrices (SM) may not always be feasible, as they take a considerable amount of time. The analytical detector response function (DRF) model has proven to be a

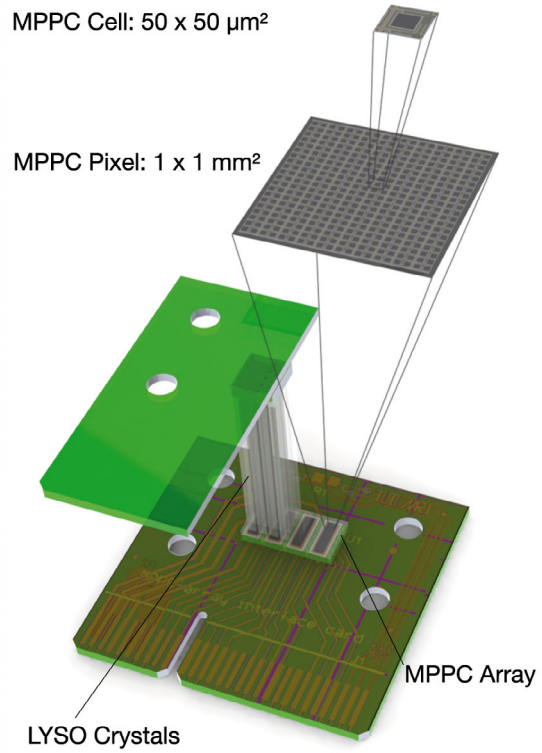

Figure 2.3.: Illustration of the detector module and the alternating frontside-backside readout of the LYSO crystal rows.

good alternative [SSD+03] which allows to rapidly calculate system matrices and thus estimate the performance of small animal scanner prototypes. The SM has been calculated for a full ring composed of 24 modules (cf. tab. 5.1). The reconstruction takes about 6 min for 30 iterations on a 48 core Linux Cluster (Xeon 2.0 GHz, 96 GB RAM).

2.2.3. Measurement and Phantom Printing

Since the radionuclide used is ^{18}F, the measured time per projection is adjusted to compensate for its radioactive decay to ensure the same weighting of events per position in the reconstructed image. One of the main challenges to test the performance in terms of spatial resolution and the calculated SM was to develop a suitable phantom with small but still well-known structures that would fit in the small FOV. Since the expected spatial resolution is in the region of the e^+ range (for ^{18}F in water: $R_{\text{mean}} = 0.6$ mm, $R_{\text{max}} = 2.4$ mm [VBTM03]), a dense material like copper around the activity is favorable to reduce the range effect in the image.
A Canon Pixma IP4200 inkjet printer was refilled with 1.0 ml ink and 0.3 ml aqueous solution of [^{18}F]-FDG with an activity of 2 GBq. A line phantom with different distances between lines was printed 50 times on the same sheet (standard

Table 2.1.: Parameters of the system matrix for the full system.

Number of crystals	768
Number of LORs	589824
Number of voxels	$400 \times 400 \times 16$
Voxel size	$0.25 \times 0.25 \times 0.25$ mm^3
Axial detector rings	4
Number of crystals per detector ring	192
Diameter	100 mm
Size of System Matrix	51 GB

copy paper, 80 g/m^2), resulting in a total activity of 2.71 MBq on the sheet. The phantom's outer dimensions were 9.2×5.6 mm^2. It is axially symmetric with respect to the central line and consists of 11 vertical lines with a thickness of 0.2 mm. The center-to-center distance between the lines decreases by 0.1 mm starting with 1.1 mm down to 0.7 mm. The phantom was trapped between 2 copper plates with a thickness of 1 mm each to reduce the positron range.

2.3. Results

2.3.1. Energy and Time Resolution

The global CTR is 4.8 ns and a mean energy resolution of $28.7 \pm 4.7\%$ FWHM (cf. fig. 2.4). A correction of the energy spectrum for non-linearity due to the limited number of SiPM cells is not necessary due to the low light yield of the used crystals. Based on a comparison measurement with well-known LYSO of the same size from another manufacturer, the light output is estimated to be about 12000 ph/MeV. Both crystals have been read out under the same environmental conditions by directly coupled single MPPC S10362-11-050C. Simulations of $1 \times 1 \times 20$ mm^3 crystals resulted in about 18% of the scintillation light reaching the active surface of the SiPM [Vel10], corresponding to $\approx$ 2160 ph/MeV. In agreement with [PSV$^+$12b], the SiPM response is still linear for this amount of light. Due to the light loss by the imperfect coupling of the crystals, their limited light output and light spreading through the epoxy layer of the detector to neighboring SiPMs ($\approx$ 10% to direct neighbors [F09]), the 511 keV photopeak is sometimes not clearly separable from the Compton background in the energy spectra. Thus for the image reconstruction the lower energy cut-off has been set to 480 keV. The coincidence time window (CTW) has been set to 13 ns for the image reconstruction. With a FWHM of 4.8 ns and this CTW, 99.9% of the events in the peak of the timing distribution (cf. fig. 2.4) are taken into account.

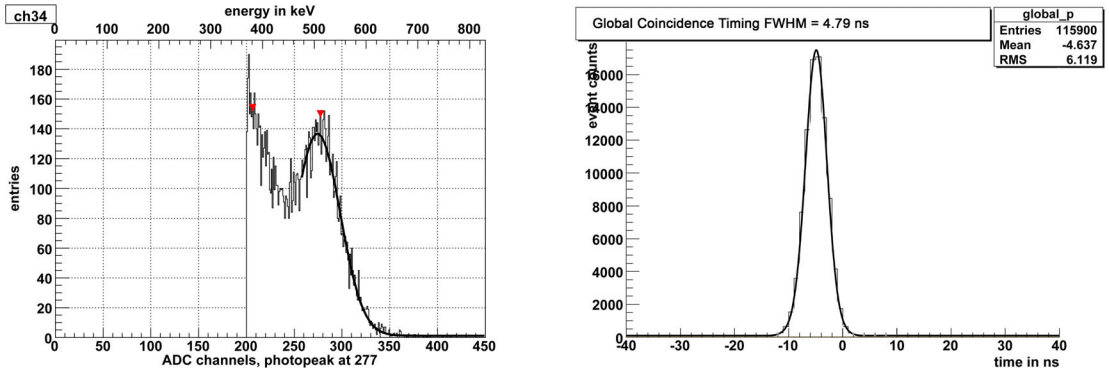

Figure 2.4.: *Left:* Exemplary energy spectrum of one detector channel irradiated by a ^{18}F source. Energy resolution $(\Delta E/E)_{\mathrm{FWHM}} = 20\ \%$.
Right: Coincidence timing histogram for all detector channels with Gaussian fit of the histogram entries. Time resolution $(\Delta t/t)_{\mathrm{FWHM}} = 4.8$ ns

2.3.2. Sensitivity Map and Homogeneous Cylinder

The calculated sensitivity maps for the central slice of the transverse, coronal and sagittal planes are shown in fig. 2.5. In the ideal case all detector channels are assumed to have the same detection efficiency. But for the prototype e.g. dead channels and different detector efficiencies are present and have to be taken into account. For the normalization correction a cylindrical flood phantom (7 mm, 20 MBq ^{18}F, 10 min) has been used. As a measure for the efficiency per detector, the number of detected singles > 480 keV has been determined (cf. fig. 2.6) and implemented as correction in the image reconstruction [Hoh12]. A significant difference of the reconstructed flood phantom can be seen with better homogeneity after the correction, which therefore has been used for all further reconstructions.

2.3.3. ^{18}F Inkjet Printed Phantom

The result of the print and its reconstruction after a total measurement time of 1 h are shown in fig. 2.7. One line has been outside of the FOV and is therefore missing in the image. MLEM with 30 iterations clearly shows the lines which can be identified also in the line profile through the sagittal plane. In the line profile through the indicated slice the peak positions match with the overlay of the phantom. Except for the smallest center-to-center distance of 0.7 mm, all lines can be separated and the spatial resolution is 0.8 mm.

2.4. Discussion

SiPMs in combination with LYSO have the advantage of a high intrinsic gain which eliminates the need for preamplifiers at the front end. This opens up new possibilities in designing new systems, since the front end can be made without

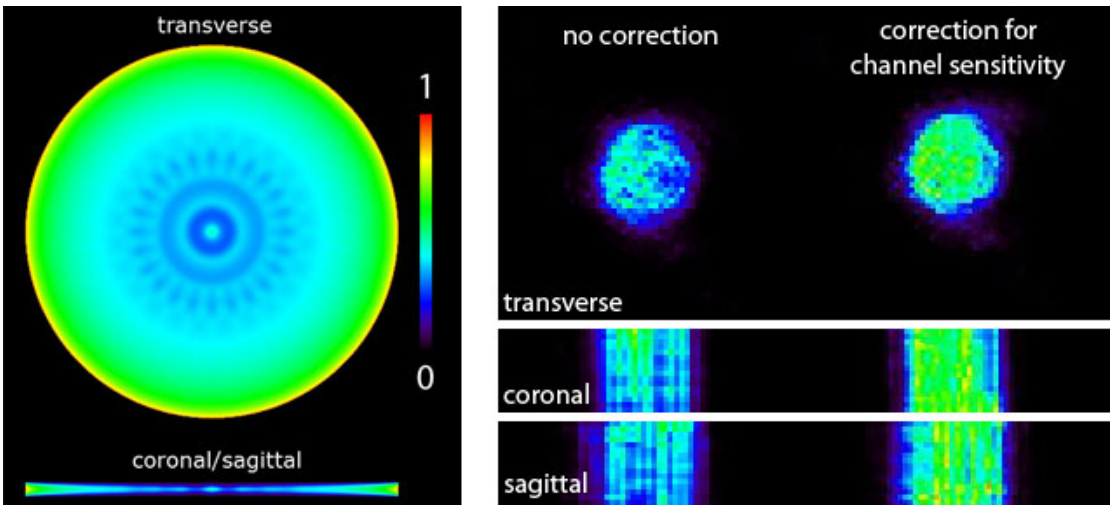

Figure 2.5.: *Left:* Sensitivity map of the DRF system matrix assuming all detectors with alike efficiency. Coronal and sagittal plane are identical due to the scanner symmetry.
Right: Reconstructed uniform cylinder phantom with 30 iterations. *Left column:* No correction for different detection efficiency taken into account. *Right column:* Individual detection efficiency of each detector channel and dead channels were considered. [Hoh12]

active electronics, which could be advantageous e.g. for combined PET/MRI. The possibility to power several SiPMs with the same bias voltage is an advantage for a system with many channels.
The single crystal readout ensures precise knowledge of the hit crystal with high granularity and spatial resolution, but on the other hand the number of electronic channels to process increases significantly compared to a block detector concept. Nevertheless the single channel readout is feasible for small animal PET with a lower absolute number of channels compared to a clinical scanner, for which it is still challenging and expensive due to the higher number of detector channels. In comparison to a block detector, when using single crystals the spatial resolution of the system is directly determined by the size of the crystal elements. Also event

Module 1

95%	90%	91%	93%	91%	88%	74%	93%
91%	82%	83%	91%	86%	87%	80%	86%
73%	78%	79%	89%	96%	88%	85%	81%
86%	69%	75%	86%	80%	83%	86%	84%

Module 2

dead	95%	100%	87%	91%	90%	88%	91%
dead	87%	100%	92%	88%	98%	84%	87%
dead	92%	87%	89%	96%	93%	90%	82%
dead	74%	79%	74%	68%	69%	74%	66%

Figure 2.6.: Detection efficiencies per detector channel for both modules. Values are normalized to the maximum number of detected singles > 480 keV.

pile up is less likely due to the smaller interaction volume which can be beneficial for studies with high activities [Zai14].
The crystal array is not perfectly rectangularly and parallelly assembled and the crystals differ slightly in length which makes the optical coupling inefficient. Furthermore, the reflecting $BaSO_4$ was only supposed to be applied in between the 8 crystal columns, but not in between the 4 crystals in one column, since the thickness of the $BaSO_4$ leads to a slight misplacement of each single crystal on top of its SiPM pixel. The thickness of the $BaSO_4$ the A single crystal of the array showed only a light output of ≈40% compared to a reference single crystal from a different manufacturer.
Due to the described loss of photons, both energy and time resolution are degraded. The CTR in addition is limited by the sampling rate of the SADCs. Despite the light spread in the epoxy layer, still the unique allocation of a single LYSO crystal is possible. In an optimal setup for a single crystal readout, the SiPMs should be optically insulated from each other. Assuming an array with no dead space due to the wire bonds, the crystals could be read out from both sides providing depth of interaction (DOI) information which would be essential to diminish the parallax error for a full ring made of 20 mm long crystals.
As visible in the photo of the printed phantom in fig. 2.7, the printing also has some limitations. The used printhead is not able to handle pure [^{18}F]-FDG(aq.) but needs a mixture with ink to still work. Therefore the deposited activity in one print is very little and multiple prints are necessary. This leads to a slight blurring of the printed lines and at some point the paper becomes saturated.
Other preclinical systems reported use light sharing methods in combination with SiPMs (block detectors), e.g. [HCJ+10, YWW+11, KCH+11, HKK+12, YKK+12, WWD+13]. Besides this work, currently three further systems based on SiPMs with one-to-one coupling to scintillators are reported in literature. Two are preclinical and have been developed in our group, one is a PET prototype based on digital SiPMs [SSSSZ15] (with LYSO: CTR 171 ps, energy resolution 12.6%) and the other the PET/MR compatible insert *MADPET4* (with LYSO: CTR 472 to 861 ps, energy resolution 8.7 to 10.4% (not corrected for saturation)) [SSS+14]. The third one is the clinical *Philips Vereos Digital PET/CT* based on digital SiPMs + LYSO with a system CTR of 345 ps [Kon14] employing time of flight (TOF) information with an energy resolution of 11.2% FWHM [MGJ+14] and a spatial resolution of 4.1 mm [Kon14]. In comparison, the reported system and the developed MADPET4 [SSS+14, Sch15] are the only ones yielding a submillimeter resolution using one-to-one coupling.

2.5. Conclusion

The presented work demonstrated a submillimeter resolution PET prototype with a spatial resolution of 0.8 mm. It has been successfully evaluated with a phantom printed with ^{18}F labeled ink. The one-to-one coupling of LYSO crystals to SiPMs

is working well, despite the described problems of limited light output and light losses and therefore limited energy and time resolution. Single individual SiPMs rather than an array with a common epoxy layer are favorable to avoid the light spread to neighboring channels. The achieved CTR is acceptable for a small animal PET without time-of-flight.

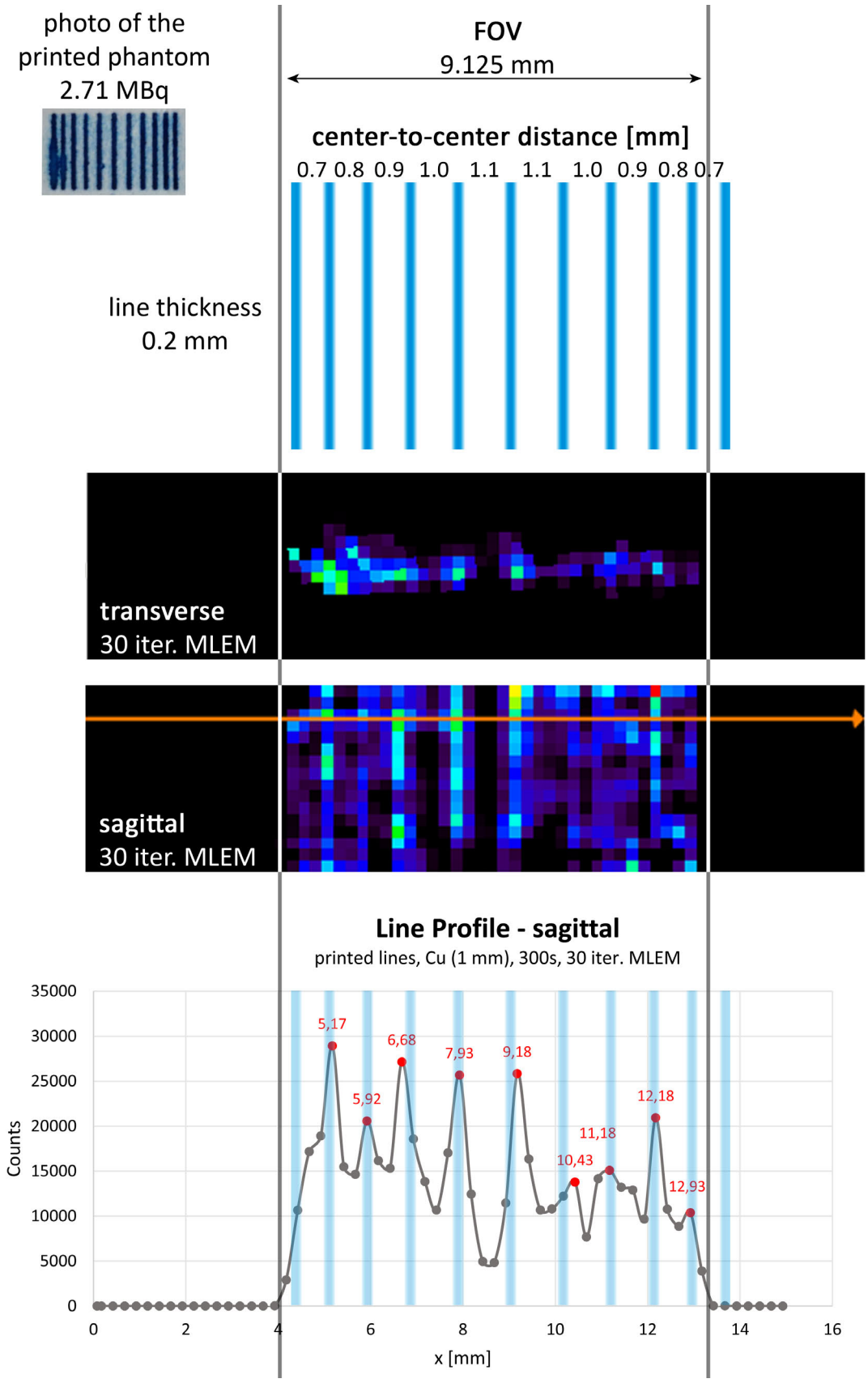

Figure 2.7.: *Top:* ^{18}F inkjet printed line phantom. *Middle:* MLEM reconstruction with 30 iterations of the line phantom for the transverse and sagittal plane. *Bottom:* Corresponding line profile through the indicated slice (orange) in the sagittal plane. The overlay of the phantom shows good agreement with the found peak positions (red, with corresponding x-value).

3. A PET Detector Prototype based on Digital SiPMs and GAGG Scintillators

This chapter has been published as
Schneider, F. R., Shimazoe, K., Somlai-Schweiger, I., Ziegler, S. I. (2015). A PET detector prototype based on digital SiPMs and GAGG scintillators. Phys. Med. Biol., 60, 1667. doi:10.1088/0031-9155/60/4/1667

Abstract: Silicon Photomultipliers (SiPM) are interesting light sensors for Positron Emission Tomography (PET). The detector signal of analog SiPMs is the total charge of all fired cells. Energy and time information have to be determined with dedicated readout electronics. Philips Digital Photon Counting has developed a SiPM with added electronics on cell level delivering a digital value of the time stamp and number of fired cells. These so called Digital Photon Counters (DPC) are fully digital devices. In this study, the feasibility of using DPCs in combination with LYSO (Lutetium Yttrium Oxyorthosilicate) and GAGG (Gadolinium Aluminum Gallium Garnet) scintillators for PET is tested. Each DPC module has 64 channels with 3.2×3.8775 mm^2, comprising 3200 cells each. GAGG is a recently developed scintillator ($Z_{\text{eff}} = 54$, 6.63 g/cm^3, 520 nm peak emission, 46000 photons/MeV, 88 ns (92%) and 230 ns (8%) decay times, non-hygroscopic, chemically and mechanically stable). Individual crystals of $2 \times 2 \times 6$ mm^3 were coupled onto each DPC pixel. LYSO coupled to the DPC results in a coincidence time resolution (CTR) of 171 ps FWHM and an energy resolution of 12.6% FWHM at 511 keV. Using GAGG, coincidence timing is 310 ps FWHM and energy resolution is 8.5% FWHM. A PET detector prototype with 2 DPCs equipped with a GAGG array matching the pixel size ($3.2 \times 3.8775 \times 8$ mm^3) was assembled. To emulate a ring of 10 modules, objects are rotated in the field of view. CTR of the PET is 619 ps and energy resolution is 9.2% FWHM. The iterative MLEM reconstruction is based on system matrices calculated with an analytical detector response function model. A phantom with rods of different diameters filled with ^{18}F was used for tomographic tests.

3.1. Introduction

Analog Silicon Photomultipliers (SiPM) are established as light sensors and already used in a recent clinical prototype for combined PET/MRI (positron emission tomography/magnetic resonance imaging) [DKH+14] [GE 14]. SiPMs are arrays of G-APD (Geiger-mode avalanche photodiode) cells, which typically consist of several $\approx 100 - 1000$ cells per mm^2. Each of these G-APD cells deliver a certain amount of released charge during a breakdown [BMR06] so they can be seen as a quasi binary device. In the case of analog SiPMs, the detector signal is the charge sum of all fired cells which then has to be digitized again by dedicated readout electronics. Traditional approaches typically use an ADC (analog to digital converter) for the energy information and a TDC (time to digital converter) for the timestamp [Kuc11], while newer approaches use ToT (time over threshold) methods by implementing TDCs e.g. in a dedicated readout ASIC [SWT+11]. Philips Digital Photon Counting has developed a different approach with electronics already attached to each G-APD cell. The so called DPC (Digital Photon Counter) uses the intrinsic digital response of each G-APD cell by directly integrating electronics on cell level, which senses the breakdown making the device fully digital from the beginning of the light detection [DZFdG10] [Phi12]. During the acquisition of one event the first firing cell gives the timestamp, while the number of fired cells of a pixel is counted for the energy information.
The focus of this work is on the feasibility as well as performance of the new DPC sensor technology together with the recently developed GAGG (Gadolinium Aluminum Gallium Garnet) scintillator. For comparison, the results with single GAGG crystals are compared with the widely used LYSO (Lutetium Yttrium Oxyorthosilicate).

3.2. Digital Photon Counters (DPC)

The layout of the DPC-3200-44-22 used in this study can be found in fig. 3.1. Specifications of the DPC-3200-44-22 are listed in tab. 3.1, where U_{bd} is the breakdown voltage and U_{over} is the overvoltage of the device. Each die with 4 pixels has one common time to digital converter (TDC). The manufacturer has implemented different triggering schemes (cf. tab. 3.2) for which one pixel is divided into 4 subpixels. The acquisition sequence can be found in fig. 3.2. Upon each fulfilled trigger condition, a time stamp per die is created. Trigger scheme 1 e.g. will always generate a trigger, when one cell has fired. Since dark counts cannot be distinguished from incoming photons that fired a cell, a high dark count rate may significantly affect the triggering. After the trigger decision for one event, a validation interval follows (5−40 ns), in which the sensor counts further fired cells to check if a certain number (validation threshold) is reached. For light emission from a scintillator, many photons impinge on the sensor during the validation time which should not be the case for a dark count induced trigger. In case the

validation threshold is not exceeded, the sensor goes into recharge ($5 - 80$ ns) and is again ready to be triggered. If the validation threshold is reached during validation time, an integration period ($0 - 20$ μs) follows, in which further fired cells are counted. Afterwards the readout of the device (680 ns) and the recharge of the cells (5-80 ns) complete the acquisition sequence for one event. The shortest possible acquisition sequence is 690 ns and the longest is 20.8 μs. Depending on the application and constraints, the trigger scheme, validation length and threshold as well as integration time have to be adapted. It should be noted that in contrast to analog SiPMs, the DPC cells can only fire once during an acquisition and have to be actively recharged in the end. A detailed introduction to the data acquisition can be found in [Sch13].

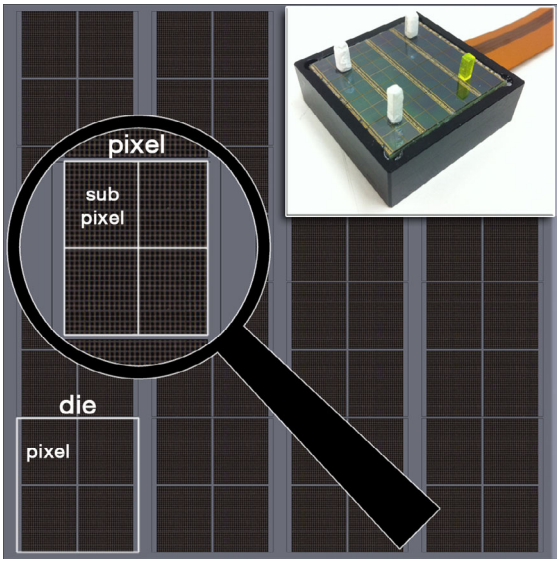

Figure 3.1.: Layout of one DPC tile. Top right an image of the sensor with different crystals coupled. A glass plate on top of the sensors protects them from damage while coupling scintillators.

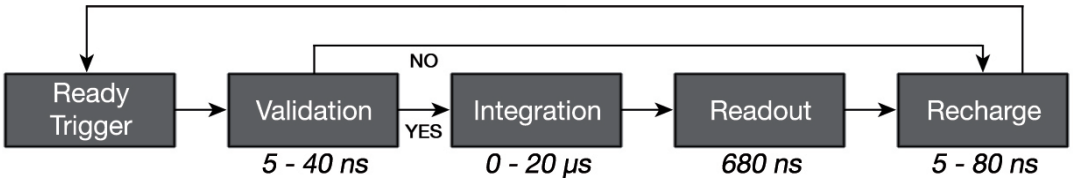

Figure 3.2.: State machine of the acquisition sequence for one event [Sch13].

Table 3.1.: Specifications of the DPC tile. All values taken from [Sch11b] and [Fra12].

Philips DPC Tile DPC-3200-44-22	
Array size	32.6×32.6 mm^2
Silicon dies	16
TDCs per die	1
Pixels	8×8
Pixel size	3.2×3.8775 mm^2
Subpixel per pixel	4
Cells per pixel	3200
Cell size	59.4×64 μm^2
Peak sensitivity	420 nm
Peak PDE	40%
Pixel fill factor	74%
U_{bd} (typ.) at 20°C	23.8 V
Operational U_{over}	3.3 V
Temp. dep. gain	0.33%/°C

Table 3.2.: Trigger scheme and the corresponding subpixel condition [Sch13].

Trigger scheme	**Average number of fired cells**	**Fired cell(s) detected on**
1	1	any subpixel
2	3.0	two different subpixels
3	6.333	two subpixels in different half of the pixel
4	8.333	all four subpixels

3.3. Experimental Methods

3.3.1. Scintillators

All measurements have been performed with the recently developed GAGG ($Gd_3(Ga,Al)_5O_{15}$:Ce) [KYE+11] and for comparison with the widely used LYSO ($Lu_{1.8}Y_{.2}SiO_5$:Ce) [SG04] (cf. tab. 4.2). The individual crystal measurements have been performed with polished crystals with a size of $2 \times 2 \times 6$ mm^3. They were always wrapped in PTFE and coupled to the sensor with Dow Corning 1-2577 silicone [DOW13] to the sensor.

Table 3.3.: Properties of the used scintillator crystals [KYE+11][SG04].

	GAGG	**LYSO**
Effective Z	54	65
Density [g/cm^3]	6.63	7.1
Peak emission [nm]	520	420
Light yield [photons/MeV]	46000	32000
Intrinsic $\Delta E/E$ at 662 keV [%]	4.7	7.1
Decay time [ns]	88 (92%), 230 (8%)	41
Hygroscopy	no	no

3.3.2. Experimental Setup and Data Acquisition

The whole front end is provided by Philips as a Technical Evaluation Kit (TEK). It consists of power supply, up to 4 DPC tiles and a base unit, which is connected via USB 2.0 to a Linux PC for control of the system and data transmission [Sch11b]. In this work, two DPC-3200-44-22 tiles were used. A detailed description of the TEK can be found in [Sch13]. The two DPC tiles are placed in a light tight box facing each other. To control the temperature of the sensors, they are mounted onto an Aluminum base which is cooled by Peltier elements combined with watercooling. With this setup temperatures below the freeze point can be achieved. All measurements have been performed at a stabilized temperature of $\approx 5°$C to reduce the dark count rate (DCR). Its mean value per cell becomes < 150 Hz with 10% inhibition of the cells with highest DCR [SSSS+13]. The temperature is measured by the sensor located on the tiles. It was not cooled below the dew point to avoid condensation due to air humidity. The basis for cell inhibition is that the DPCs allow to measure a dark count map (DCM). This mode measures each cell one after another for a specified time and counts how often the cell fires. With the specified time and the absolute number of counts per cell, the DCR in Hz can be calculated. Afterwards cells showing high DCR can be selected and inhibited. In addition, measuring a DCM with a coupled crystal and a radioactive source allows to visualize its coupling.

Further common conditions in all measurements are inhibition of 10% of the cells with the DCR and triggering on the 1st photon to achieve best possible timing performance. The validation threshold is always set to 4 fired cells within a validation time of 10 ns, integration time is always 85 ns, and the default overvoltage of 3.0 V is used. An estimation of events triggered by scintillation can be done with the energy spectrum, in which dark count triggered events are histogrammed close to 0. They result in a peak which can be clearly distinguished from the low energetic Compton background. For the measurements with the single $2 \times 2 \times 6$ mm^3 crystals and the used ^{22}Na point-like source (3.7 MBq), the ratio of counts not in this peak and the total counts results in approximately 10% of total events which have been triggered by scintillation.
To control, configure, and read out the DPCs, Philips also provides their open source software *dpcshell* which is command line based and capable of executing scripts. The incoming datastream is written to the hard disk in ASCII format and then processed further by customly written bash, C++ and ROOT programs.

3.3.3. PET Prototype

The PET prototype is equipped with a 8×8 GAGG array matching the pixel size, coupling each $3.2 \times 3.8775 \times 8$ mm^3 GAGG crystal one-to-one to a DPC pixel (cf. fig. 3.3). The sources in the FOV are rotated in 5 steps by 36° to simulate a full ring with 10 modules. With the two DPCs a field of view (FOV) with a diameter of 30.4 mm and an axial extent of 31.8 mm is covered.
An iterative reconstruction based on Maximum Likelihood Expectation Maximization (MLEM) is used [SV82] with system matrices calculated with the detector response function (DRF) model [KPS$^+$10] [SSD$^+$03].

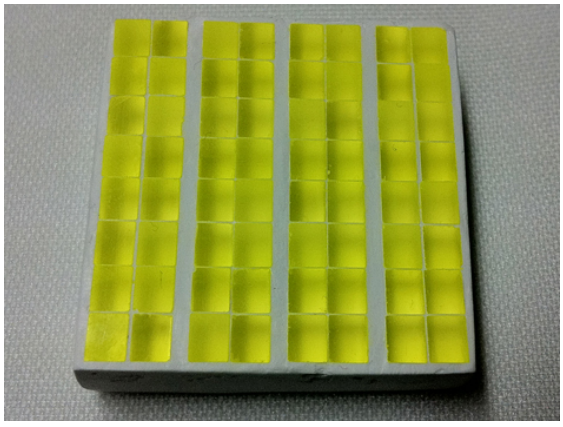

Figure 3.3.: GAGG array matching the pixel size of the DPC. Each crystal is $3.2 \times 3.8775 \times 8$ mm^3 and embedded in $BaSO_4$ reflector.

3.3.4. Energy and Coincidence Time Resolution

Energy spectra and the coincidence time resolution (CTR) were acquired with a ^{22}Na point-like source (3.7 MBq). $\Delta E/E$ was obtained by a Gaussian fit with linear background estimation while the CTR was a single Gaussian fit. To suppress compton events in the CTR, an energy window corresponding to the FWTM (full width at tenth maximum) of the 511 keV peak was applied.
Saturation effects in the energy spectrum are to be expected, since both LYSO and GAGG have a high light yield (cf. tab. 4.2) compared to the number of cells on the DPC pixel. Assuming no inhibition of high dark count rate cells, for the individual crystals there are ≈ 1054 cells directly under the end face area of 2×2 mm^2, reduced to ≈ 949 cells with the 10% inhibition used in this study. In the case of the GAGG array, 3200 cells are available for each crystal, reduced to 2880 cells with 10% inhibition.

With crystals not matching the pixel size the number of effective cells m which are able to fire is larger than those directly under the crystal end face, since the glass plate between crystal and sensor introduces a spread of the light making it possible to fire also surrounding cells (cf. fig. 3.4). The theoretical number of detected photons p_E for linear response can be calculated with [DPF$^+$09]

$$p_E = -m \cdot \ln(1 - k_E/m) \tag{3.1}$$

where k_E is the number of detected photons for a certain energy E. By the known relation of the photopeak energies $c = 1275$ keV/511 keV ≈ 2.49 for ^{22}Na, the effective number of cells $m > k_{1275\text{ keV}}$ can be iteratively determined, so that with the corrected numbers of photons p_E the following holds

$$\frac{p_{1275\text{ keV}}}{p_{511\text{ keV}}} = \frac{\ln(1 - k_{1275\text{ keV}}/m)}{\ln(1 - k_{511\text{ keV}}/m)} = c \tag{3.2}$$

With determined m, the ratio p_E/k_E can then be defined as the saturation correction factor.

3.4. Results and Discussion

3.4.1. Optical Coupling

Using the dark count map acquisition of the DPCs the coupling of the crystals is visualized (cf. fig. 3.4). Especially in case of the individual $2 \times 2 \times 6$ mm^3 GAGG crystals the light spread due to the glass plate between sensor and crystal is visible. The single crystals are coupled with Dow Corning 1-2577 silicone while the array is coupled with optical grease. Both images are corrected for dark count background and have been acquired with an ^{18}F filled water cylinder in the FOV.

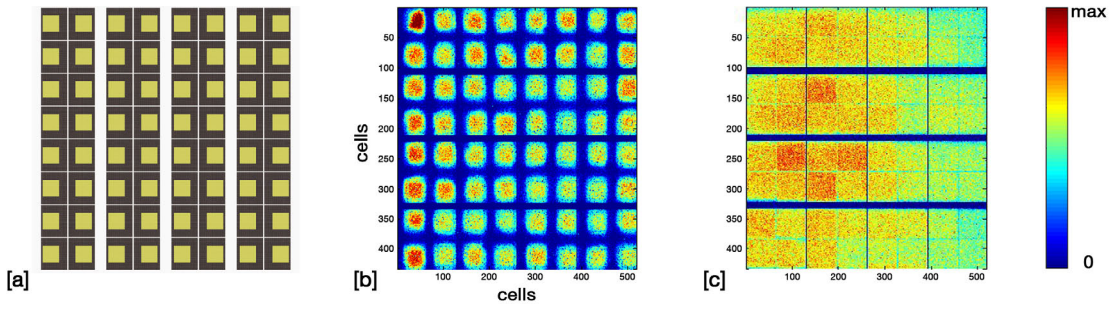

Figure 3.4.: Visualization of the coupling with help of the dark count map acquisition. *[a]* Illustration of the equidistantly placed $2 \times 2 \times 6$ mm^3 crystals on the sensor with a pitch of 4 mm, *[b]* DCM with the single $2 \times 2 \times 6$ mm^3 GAGG crystals, and the *[c]* GAGG array matching the pixel size.

3.4.2. Energy Resolution

Figures 3.5 and 3.6 show energy spectra of ^{22}Na and single $2 \times 2 \times 6$ mm^3 crystals. The spectra show saturation effects with significant compression of the spectra to lower energies. $\Delta E/E$ FWHM for LYSO is 7.9% before and 12.6% after saturation correction, for GAGG it is 5.0% uncorrected and 8.5% corrected. In the case of GAGG the 511 keV photopeak starts to have a shoulder to higher energies due to the strong compression of the 1275 keV Compton background which was the reason to exclude this part in the Gaussian fit for the energy resolution. The saturation correction factors of 1.6 for LYSO and 1.7 for GAGG are significantly higher than e.g. for analog Hamamatsu MPPCs where a correction factor of 1.1 with GAGG has been reported [YYD+13]. The reason is that during the acquisition sequence of the DPC cells can only fire once and are then not active anymore. This results in a loss of available cells during the integration phase and thus higher saturation compared to analog SiPMs where cells can fire multiple times during one scintillation event. Although GAGG has 1.5 times higher light output, the photopeak position is only about a factor 1.15 higher in photon counts (ratio 0.77). It could be explained by the PDE of the DPCs which is 39% at 420 nm (LYSO) and 30% at 520 nm (GAGG), resulting in the same ratio of 0.77 [Fra12]. In the case of the PET prototype with the GAGG array, the energy spectrum is less compressed since all cells per pixel except the 10% inhibited are available. For a randomly chosen pixel, $\Delta E/E$ FWHM is 5.35% before and 9.2% after saturation correction (cf. fig. 3.7). Another publication with the same sensor reports 10.7% with $4 \times 4 \times 22$ mm^3 LYSO [DPF+09]. In comparison with analog SiPMs (all values saturation corrected), the best currently reported values with $3 \times 3 \times 5$ mm^3 crystals are 9.5% for LYSO and 7.0% for GAGG with FBK-RGB-HD SiPMs [FGS+14b]. With the same $2 \times 2 \times 6$ mm^3 crystals as used on the DPCs, 12.3% for LYSO and 10.8% for GAGG with KETEK PM3350 SiPMs have been measured [SGS+14].

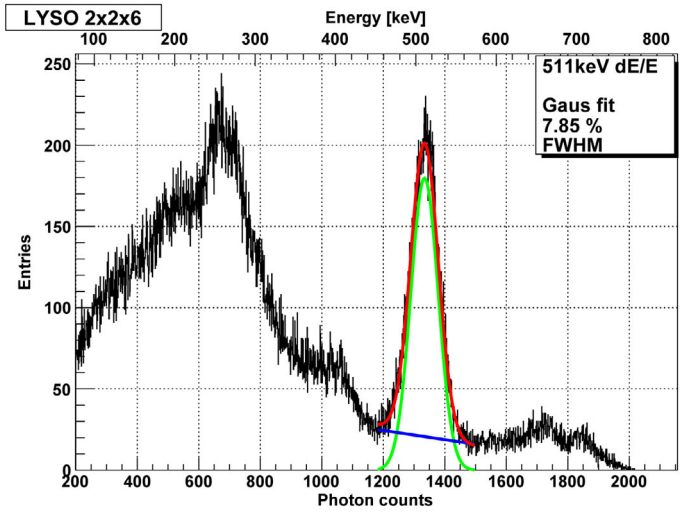

Figure 3.5.: Energy spectrum of ^{22}Na and a $2 \times 2 \times 6$ mm^3 LYSO crystal covered in PTFE. Not corrected for saturation.

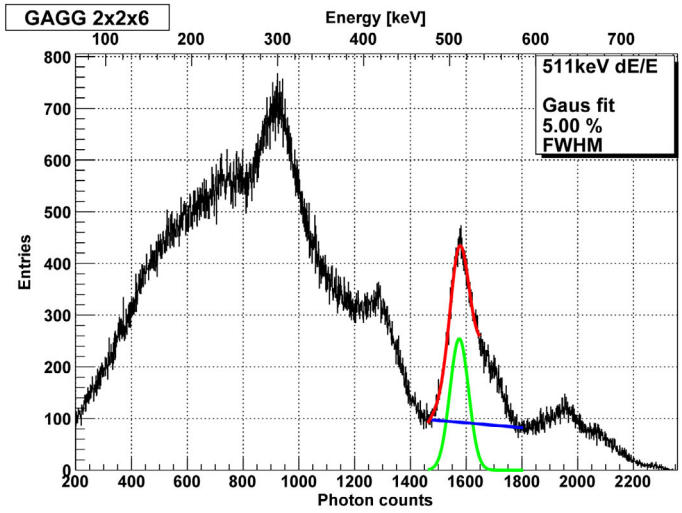

Figure 3.6.: Energy spectrum of ^{22}Na and a $2 \times 2 \times 6$ mm^3 GAGG crystal covered in PTFE. Not corrected for saturation.

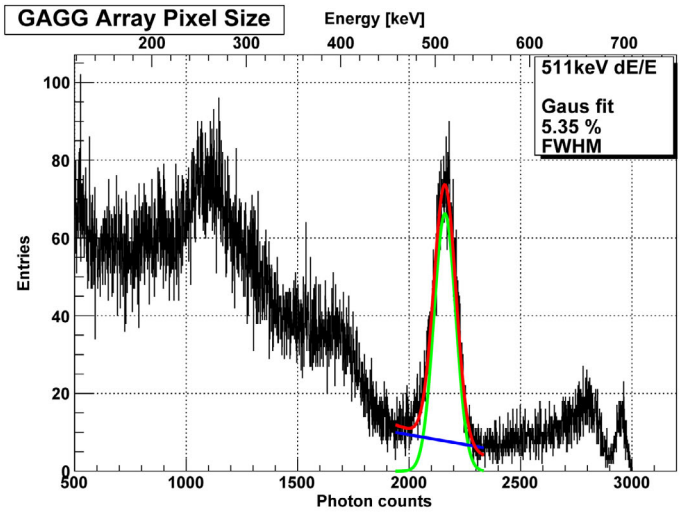

Figure 3.7.: ^{22}Na energy spectrum of one $3.2 \times 3.8775 \times 8$ mm^3 pixel when using the GAGG array. Not corrected for saturation.

3.4.3. Coincidence Time Resolution (CTR)

The results for the CTR of two opposing DPC pixels, each equipped with a single $2 \times 2 \times 6$ mm^3 crystal are shown in fig. 3.8 and 3.9. With LYSO 171 ps FWHM and with GAGG 310 ps FWHM could be achieved. In the case of the PET detector prototype, where each DPC pixel is equipped with a $3.2 \times 3.8775 \times 8$ mm^3 GAGG crystal (128 total), the CTR degrades to 619 ps FWHM (cf. fig. 3.10). Reasons could be the larger crystal size and the signal runtimes between the different pixels and/or TDC skew depending on the position on the DPC tile. Since for the DPCs there is one TDC per die (4 pixels), the recorded timestamp can not definitely be assigned to a pixel. It is assumed, that per acquired event always the pixel per die with the highest photon count also generated the timestamp.
In comparison [DPF+09] reports with two $3 \times 3 \times 5$ mm^3 LYSO a CTR of 153 ps. With analog SiPMs, the best currently reported value with $3 \times 3 \times 5$ mm^3 crystals is 138 ps for LYSO on a HPK MPPC S10362-33-050 [SvDV+12] and 255 ps for GAGG on a FBK RGB-HD SiPM [FGS+14b].

3.4.4. PET Detector Prototype

Figure 3.11 shows the sensitivity maps of the system matrix for the ring with the 10 DPC modules equipped with the GAGG array. The system matrix has a size of 1.2 GB with $60 \times 60 \times 60$ voxels with an edge length of 0.5 mm, which corresponds to the dimensions of the reconstructed images and the FOV that can be covered with two opposing DPCs.

Different ^{18}F filled rods (∼MBq, length: 9 mm, diameters: 2.5 mm, 3.5 mm, 4.5 mm, 5.5 mm) were used as test sources in the PET detector prototype. The distances of the rod's center from the center of FOV increase in 1 mm steps

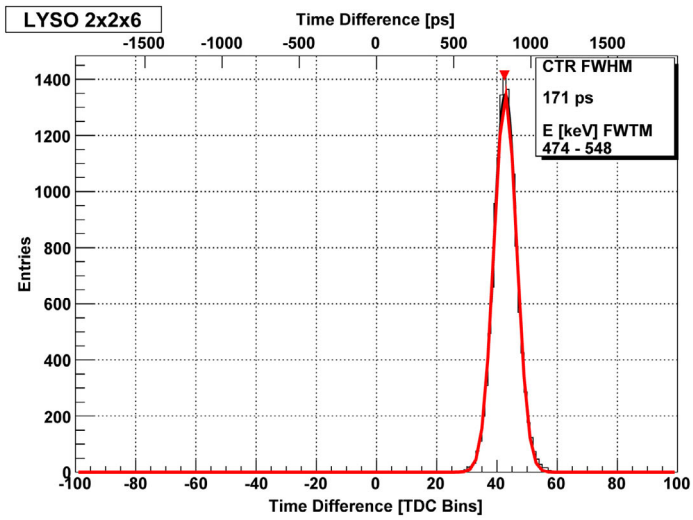

Figure 3.8.: CTR between two $2 \times 2 \times 6$ mm^3 LYSO crystals with energy cut to FWTM of the 511 keV peak.

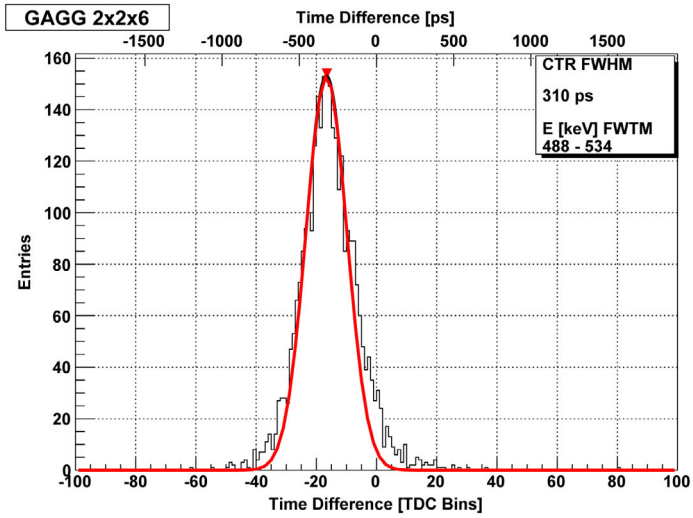

Figure 3.9.: CTR between two $2 \times 2 \times 6$ mm^3 GAGG crystals with energy cut to FWTM of the 511 keV peak.

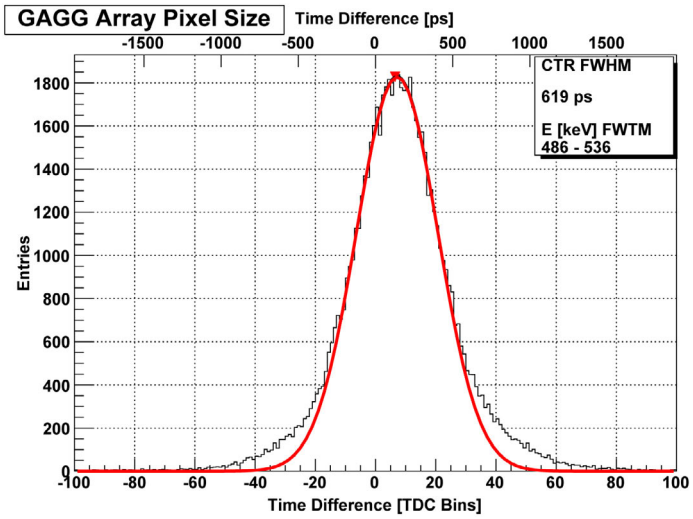

Figure 3.10.: CTR of two DPC tiles equipped with the GAGG array. All channels have been taken into account with an energy cut to the FWTM of the 511 keV peak.

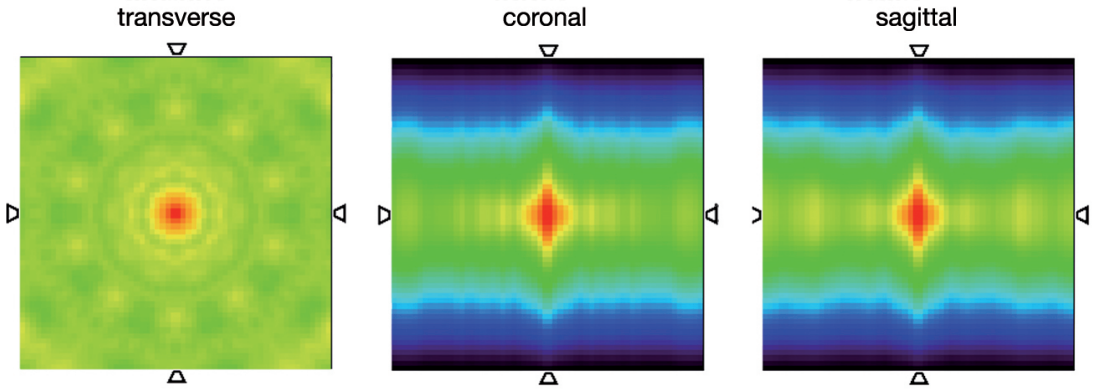

Figure 3.11.: Central slices of the sensitivity maps of the DRF calculated system matrix.

from 7.5 mm (innermost rod) to 11.5 mm (outermost rod). Figure 3.12 shows a sketch of the hot rods inside the scanner together with the covered FOV. The reconstructed rods with 10 iterations MLEM with a coincidence time window and a lower energy threshold set to the corresponding FWTM of $\approx$ 1.5 ns and 486 keV based on the measurements with the GAGG array (cf. fig. 3.10). With 5 rotations the total measurement time is 100 s resulting in 33588 true coincidences. The reconstructed rods (cf. fig. 3.13) can be clearly separated and the different diameters are reflected. The outermost rod shows an artifact which could be caused by the vicinity to the edge of the FOV. Due to a little misalignment of the phantom in the center of the FOV, this rod could be slightly outside of the FOV during the rotation.

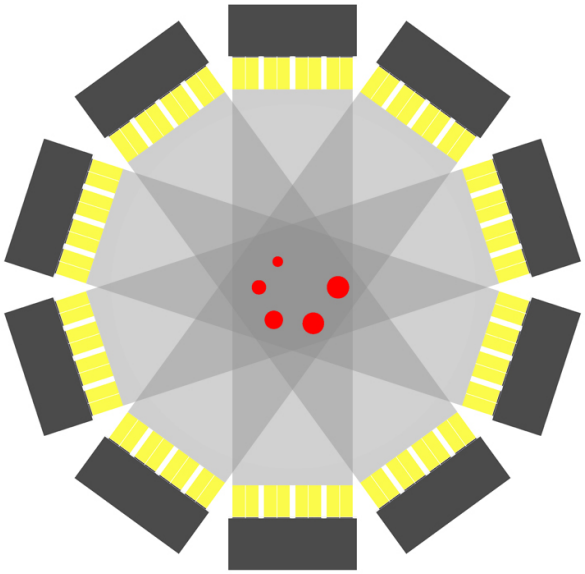

Figure 3.12.: Model of the ring with 10 DPCs with the GAGG arrays. The hot rod phantom is rotated in 36° steps. Inner diameter is 100 mm.

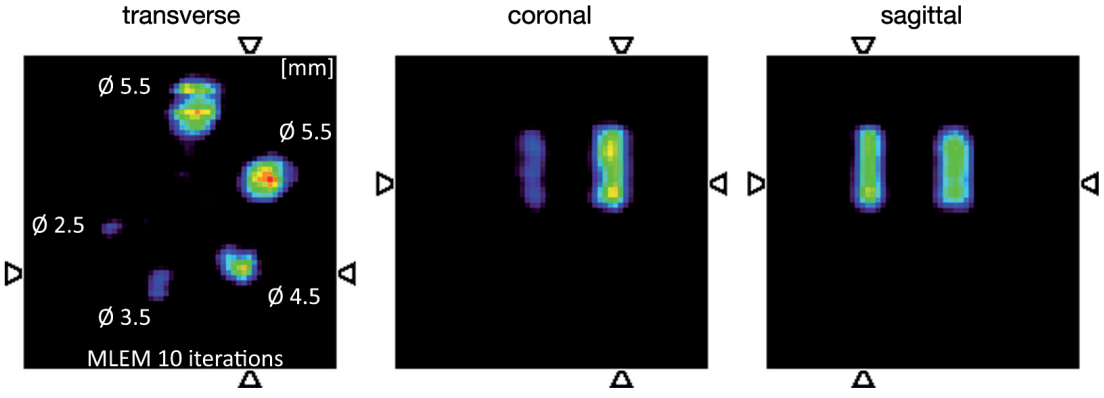

Figure 3.13.: Reconstruction of the rod-phantom and its dimensions.

3.5. Conclusions

The DPCs with GAGG show a good performance and the combination works well as a PET detector. GAGG on one hand is brighter than LYSO with a better intrinsic energy resolution. On the other hand, it shows about a factor 2 higher CTR and has a lower probability for photoelectric effect of 511 keV photons due to its lower effective Z. Its intrinsic self-radiation is negligible which may be advantageous for the measurement of very low activities with a low energy threshold. For small animal PET applications, GAGG can be an alternative since usually time-of-flight is not the main focus because of the small ring diameters. Due to the better energy resolution of GAGG, the recovery of inter-crystal scattered events when measuring with a low energy threshold may potentially make up for the lower interaction probability.
The DPCs work well with both LYSO and GAGG and provide very good time resolution. The sensors are capable for time-of-flight PET. Due to the DPC architecture where cells can only fire once during an acquisition, the energy spectra are significantly nonlinear with such bright scintillators, which demands for a correction. GAGG shows a higher saturation than LYSO which gets more visible in the spectrum for the crystals smaller than the DPC pixel size. Especially for small animal PET with high demands to spatial resolution, the used one-to-one coupling limits the spatial resolution due to the relatively large pixel size.

Acknowledgments

Dr. R. Schulze from Philips Digital Photon Counting for the always helpful and available support. Prof. Dr. Kei Kamada from C&A Corporation Japan for providing the GAGG crystals and manufacturing the GAGG array.
The research leading to these results has received funding from the European Union Seventh Framework Program (FP7) under Grant Agreement No. 294582 ERC Grant MUMI.

4. Characterization of Blue Sensitive 3×3 mm^2 SiPMs and their Use in PET

This chapter has been published as
Schneider FR, Ganka TR, Şeker G, Engelmann E, Renker D, Paul S, Hansch W, Ziegler SI (2014). Characterization of Blue Sensitive 3×3 mm^2 *SiPMs and their Use in PET. Journal of Instrumentation, 9(07), P07027P07027. doi:10.1088/1748-0221/9/07/P07027*

Abstract: Three types of SiPMs (Silicon Photomultiplier) with an active area of 3×3 mm^2 manufactured by KETEK with cell sizes of 50 μm (PM3350), 60 μm (PM3360) and 75 μm (PM3375) have been investigated. All devices have optical trenches in between the cells to suppress direct crosstalk. Their breakdown voltage at room temperature is about 23 V and the gain at an overvoltage $U_{\text{over}} = 3.4$ V is $> 6 \cdot 10^6$. The temperature variation of the breakdown voltage is < 16 mV/K and the gain coefficient with temperature is $< 1\%$ for overvoltages $U_{\text{over}} > 1.7$ V. The photodetection efficiency (PDE) at 420 nm and $U_{\text{over}} = 3.4$ V is 51% for PM3350, 55% for PM3360 and 58% for PM3375. At $U_{\text{over}} = 3.4$ V, the dark count rates are < 470 kHz/mm^2 at 20°C and the afterpulse probability is $< 9\%$ at -20°C. Single photon timing of 230 ps FWHM for PM3350, 320 ps for PM3360 and 375 ps for PM3375 have been achieved. To test their performance in PET (Positron Emission Tomography), energy spectra of ^{22}Na with LYSO (Lutetium Yttrium Oxyorthosilicate, $Lu_{1.8}Y_{.2}SiO_5$:Ce) and GAGG (Gadolinium Aluminum Gallium Garnet, $Gd_3(Ga,Al)_5O_{15}$:Ce) scintillators with a size of $2 \times 2 \times 6$ mm^3 have been acquired. The saturation corrected energy resolution (FHWM) at 511 keV was with LYSO 12.3% for PM3350, 13.4% for PM3360, 12.4% for PM3375 and with GAGG 10.8% for PM3350. Coincidence timing (FWHM) at $U_{\text{over}} = 3.4$ V was with LYSO 174 ps for PM3350, 178 ps for PM3360, 157 ps for PM3375 and with GAGG 430 ps for PM3350.

4.1. Introduction

SiPMs (Silicon Photomultiplier, also called e.g. G-APD Geiger-Mode Avalanche Photodiodes or PPD Pixelated Photo Detectors) have been established for detecting visible light in recent years [BMR06]. Their application ranges from counting single photons to the readout of bright scintillators with thousands of photons impinging onto the SiPM. Their advantages are compactness, insensitivity to magnetic fields and their high gain in the range of 10^5-10^7 with the potential for a high PDE [BMR06]. As it is common for every avalanche diode, the excess noise factor (ENF) of SiPMs is > 1 but lower for SiPMs than e.g. for avalanche photodiodes (APD) [BMR06] [McI66]. SiPMs in particular have the disadvantages of dark counts, optical crosstalk, afterpulsing and limited dynamic range due to the limited number of cells and their recovery time. Depending on the application these properties have to be considered. The motivation for this work was the basic characterization of the SiPMs and their usability in Positron Emission Tomography (PET) for which the KETEK 3×3 mm^2 series is interesting since the manufacturer promises a low temperature dependency, high photo detection efficiency (PDE) and a high gain. Furthermore, the thin depletion region of the investigated devices allows a low operating voltage. The operation at high overvoltages, where the Geiger probability saturates, is possible.

4.2. Detectors

The investigated SiPMs have been developed by KETEK during the last years [Wie11] and are of p-on-n type with their peak sensitivity at 420 nm. KETEK's current PM33** series with an active area of 3×3 mm^2 and cell sizes (**) of 50, 60 and 75 μm has been investigated. All three tested types feature optical trenches in between the cells to reduce crosstalk. The active area is covered by a protection layer of ≈ 300 μm epoxy with an index of refraction of 1.53 [KETc]. The package is either SMD (Surface Mount Device) or with soldering pins. Basic properties of the detectors are listed in tab. 4.1.

Table 4.1.: Geometrical properties of PM33** [KETb].

	Active Area [mm^2]	**Cell Pitch** [μm]	**Cells**	**Fill Factor** [%]	**Package Size** [mm^2]
PM3350	3.0×3.0	50	3600	60	3.8×4.3
PM3360	3.0×3.0	60	2500	66	3.8×4.3
PM3375	3.0×3.0	75	1600	72	3.8×4.3

4.3. Theoretical and Experimental Methods

4.3.1. Experimental Setup

In this study the SiPMs have been measured in a light tight and temperature controlled box. The output of the SiPM has been preamplified with a gain of ≈ 10 (Photonique, AMP-0611) and was then routed directly to a digital oscilloscope (LeCroy WaveRunner 64MXi-A) terminated with 50 Ω. Bias supply and current measurement were done with a picoammeter/voltage source (Keithley 6487). The used light source was a picosecond light pulser (Hamamatsu Photonics K.K. (HPK) PLP-10-040) with a full width at half maximum (FWHM) of the optical output pulse of 60 ps (typ.) and 405 nm emission [Ham]. All measurement data are taken by the scope and then processed with custom LabView or Matlab applications.

4.3.2. Breakdown Voltage and Gain

From the single photon spectra at different operating voltages, it is possible to extract the breakdown voltage U_{bd} which is defined as the voltage where the gain M is close to zero. The relative gain Δ is the distance between the equidistant peaks in the single photon spectrum and is proportional to the overvoltage $U_{\mathrm{over}} = U_{\mathrm{bias}} - U_{\mathrm{bd}}$, where U_{bias} is the applied voltage. The intercept with the x-axis of the linear fit of Δ versus different U_{over} determines the breakdown voltage U_{bd} [ESSCS09]. The absolute gain M of the SiPM can be calculated with known single cell charge. Using

$$Q_{\mathrm{cell}} = C_{\mathrm{cell}} \cdot U_{\mathrm{over}} \tag{4.1}$$

and the elementary charge e it follows that

$$M = \frac{C_{\mathrm{cell}} \cdot U_{\mathrm{over}}}{e} \tag{4.2}$$

The measurements where performed at controlled laboratory temperature of 20 °C and in a refrigerator at -18 °C to extract the temperature dependency of gain and breakdown voltage. From the total measured charge in the waveforms the absolute gain was calculated by

$$M = \frac{V_{\mathrm{meas}} \cdot t}{R \cdot N_{\mathrm{cells}} \cdot e} \tag{4.3}$$

with $V_{\mathrm{meas}} \cdot t$ as the total area under the waveform, R the input resistor and N_{cells} the total number of fired cells. This calculation can only be valued as approximation, because of the influence of afterpulsing during the recovery of the detector. Compared to the integration of the total charge of single pe pulses, the used method delivers a more robust result for long (> 700 ns) gates.

4.3.3. I-V and C-V Characterization

For the measurement of the dark current versus bias the SiPM was directly connected to the picoammeter without preamplifier (current resolution 10 pA). Every cell has its individual poly-silicon resistor R_{cell}. All cells are connected in parallel forming the SiPM resistivity R_{SiPM} and therefore $R_{\text{cell}} = N_{\text{cells}} \cdot R_{\text{SiPM}}$ holds. At high enough voltages in forward bias direction the I-V curve has a linear slope $m = 1/R_{\text{SiPM}}$ and the SiPM resistivity R_{SiPM} can be calculated [PBB+07].
The cell capacity is measured with a semiconductor parameter analyzer (Keithley 4200-SCS). It combines a DC source to deplete the junction and an AC source to charge and uncharge the device. The DC voltage was increased in steps of 0.1 V after each capacitance measurement. A charging and uncharging frequency of 10 kHz and a amplitude of 10 mV peak to peak was used. The connection capacitance of the setup was compensated before the measurement.

4.3.4. Photo Detection Efficiency (PDE)

The PDE of SiPMs, which depends on the wavelength λ, can be written as

$$\text{PDE}(\lambda) = \text{QE}(\lambda) \cdot \epsilon_{\text{Geiger}} \cdot \epsilon_{\text{geometry}} \tag{4.4}$$

where $\text{QE}(\lambda)$ is the quantum efficiency and ϵ_{Geiger} is the probability for a carrier created in the active cell volume to initiate a Geiger-mode avalanche. The geometrical efficiency or fill factor $\epsilon_{\text{geometry}}$ is the fraction of the active area of the SiPM and the total area of the SiPM [Ren09]. For a practical measurement, the absolute PDE can also be obtained via the relative PDE, which is determined by measuring the total number of counts and the counts in the pedestal of a single photon spectrum. Its statistics follows a Poisson-distribution with $k = 0$ for the pedestal [Mus07]:

$$P(k, \delta) = \frac{\delta^k e^{-\delta}}{k!} \tag{4.5}$$

$$k = 0 \quad PDE_{\text{rel,SiPM}} = \delta = -\ln \frac{\text{countspedestal}}{\text{countstotal}} \tag{4.6}$$

To determine the absolute PDE of the tested device we used a reference detector with known absolute PDE, in our case a KETEK PM3350 (measured by Yuri Musienko, FNAL). When illuminating the reference SiPM with the same light source, same light intensity, same light pulse frequency and under alike geometrical conditions as the tested SiPM, the following equation holds:

$$PDE_{\text{abs,SiPM}} = PDE_{\text{abs,ref}} \cdot \frac{PDE_{\text{rel,SiPM}}}{PDE_{\text{rel,ref}}} \tag{4.7}$$

With this method, afterpulses and crosstalk are not affecting the stated absolute PDE.

A tunable light source (FWHM = 6 nm; $390 - 1200$ nm) was used to measure the spectral response. First, the wavelength dependent power density was measured with a reference photodiode which is calibrated according to NIST (National Institute of Standards and Technology). Afterwards, the photodiode was replaced by the SiPM and the wavelength dependent output current could then be set in relation to the spectral power density, resulting in the relative quantum efficiency of the SiPM [LH08].

4.3.5. Dark Count Rate (DCR)

The DCR is determined by analyzing waveforms which have been randomly recorded by the scope in a gate of 10 μs. The analysis algorithm counts every peak (dark count) with an amplitude >0.5 pe. For each measurement point 2500 waveforms are taken into account. With the mean value of counts per waveform N_{avg} the dark count rate was calculated by $N_{\mathrm{avg}}/10$ μs.

4.3.6. Crosstalk Probability (CTP)

The CTP is determined by the single photon spectrum recorded at a trigger level of 0.5 pe in darkness. It is the ratio of counts > 1 pe and the number of total counts in the spectrum. The gate width of the area measurement was set to 10 ns to exclude afterpulses. With this method not only the initial crosstalk events are taken into account, but also further induced crosstalk events since an initially crosstalk triggered cell can again trigger further cells. The SiPMs have been measured without covering the epoxy surface which means that also photons reflected at the boundary of epoxy to air contribute.

4.3.7. Afterpulse Probability (AP)

The AP is measured by triggering on dark pulses with 1 pe amplitude. In a gate of 100 ns before the initial trigger pulse the waveform was checked for other pulses, which could also initiate afterpulses. These waveforms were excluded from the analysis. The triggered pulse is followed by a gate of 0.95 μs length in which the time and amplitude of occurring pulses are recorded. For each measurement point 25000 events are analyzed.
A characteristic of afterpulses is their smaller amplitude compared to the initial dark count. Since the electric field in the SiPM cell is not fully reestablished during recharging, the amount of charge released in a breakdown is lower.
The first afterpulses which could be distinguished from noise occurred approximately 30 ns after the triggering pulse. For the calculation of the AP, the following method was used: Every subsequent pulse and its delay time after the initial triggering pulse was recorded and a histogram of the temporal distribution was generated. The distribution was fitted with a superposition of two exponential decay functions (cf. fig. 4.1). One fits the thermal dark noise (long decay time) and

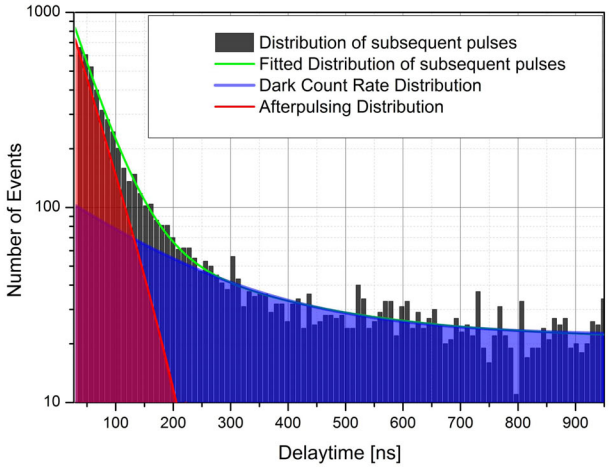

Figure 4.1.: Time distribution of subsequent pulses. The red area corresponds to afterpulsing events and the blue area to dark count events.

the other fits the afterpulse distribution (short decay time). No weighting function was used to decrease the contribution of early occurring afterpulses. This means that the contribution of every afterpulse is the same and independent of the released charge of the afterpulse. The afterpulse probability has been calculated as the ratio of the integral of the afterpulse fit to the total area.

4.3.8. Single Photon Time Resolution (SPTR)

In addition to the first preamplifier a second one (CAEN N979) was used which produced two identical output pulses. Each was fed into a fixed threshold discriminator (LeCroy 621S), the first opening a gate if the threshold of 0.5 pe was exceeded and the second opening a gate if exceeding 1.5 pe. Both gates have been fed into a coincidence unit (CAEN N455), where the first gate determined the timing and the second gate acted as a veto. This setup filtered only events where exactly one cell has fired. To decrease the probability of triggering on dark counts the measurement has been performed at $-18°$C. The delay between the laser output and the gate produced was histogrammed and the FWHM of the temporal distribution is the SPTR. Its FWHM was extracted with linear interpolation.
The time resolution of the preamplifier and the NIM electronics have been measured with a strong laser pulse onto the SiPM to fire all microcells at once. In this state the time resolution of the SiPM is a few ps and negligible due to FWHM $\sim 1/\sqrt{N_{\text{photons}}}$ with N_{photons} being the number of incident photons. The overvoltage of the SiPM was set to a small level ($50 - 100$ mV) where the output pulse shape of the SiPM was assumed to be identically to a 1 pe pulse. Subsequently the signal was fed into the same preamp and NIM electronics. The

resulting time resolution of the setup was $\mathrm{FWHM_{NIM}} = 170$ ps and had a gaussian shape. The $\mathrm{FWHM_{meas}}$ from the single photon timing spectrum has been corrected for this contribution. $\mathrm{FWHM_{SPTR}}$ is then given by:

$$\mathrm{FWHM_{SPTR}} = \sqrt{\mathrm{FWHM_{meas}^2} - \mathrm{FWHM_{NIM}^2}} \tag{4.8}$$

4.3.9. Measurements with LYSO and GAGG

A potential application for the investigated SiPMs is PET where typically bright and dense scintillator materials are used. The measurements have been performed with the recently developed GAGG ($Gd_3(Ga,Al)_5O_{15}$:Ce), Gadolinium Aluminium Gallium Garnet [KPN+12] and the widely used LYSO ($Lu_{1.8}Y_{.2}SiO_5$:Ce, Lutetium Yttrium Oxyorthosilicate) [SG04] (cf. tab. 4.2). For comparability of the results the size of the polished crystals was always $2\times2\times6$ mm^3, they were always wrapped in Teflon and coupled with Dow Corning 1-2577 silicone [DOW13]. Energy spectra of a ^{22}Na have been acquired by histogramming the pulse area on each trigger. The coincidence time resolution (CTR) has been measured between the two amplified signal outputs at an absolute threshold ≥ 1.5 pe. To suppress compton events, also an energy filter was set, with the condition for both pulse areas to exceeded the minimum of the valley between compton edge and 511 keV photopeak. The energy filter limits the time walk of the rising edge. By replacing both SiPMs with a pulser the intrinsic coincidence time resolution of the setup has been measured to be 117 ps. All CTR values have been corrected for that (cf. eq. 4.8).

Table 4.2.: Properties of the used scintillator crystals.

	GAGG	**LYSO**
Effective Z	54	65
Density [g/cm^3]	6.63	7.1
Peak emission [nm]	520	420
Light yield [photons/MeV]	46000	32000
Intrinsic $\Delta E/E$ at 662 keV [%]	4.7	7.1
Decay time [ns]	88 (92%), 230 (8%)	41
Hygroscopy	no	no

4.4. Results and Discussion

4.4.1. Detector Signal, Cell Capacitance and Resistivity

The shown waveforms were measured with 12.4 Ω load at 26.0 V bias (cf. fig. 4.2). All three detectors have rise times between 665 ps and 700 ps. The measurement is mainly limited by the 1 GHz input bandwidth of the oscilloscope. Further about 5% of the total charge is within the first fast signal component suggesting that the capacitance of the poly-silicon resistor has measurable influence on the signal shape. The decay constants τ have been extracted from an exponential fit

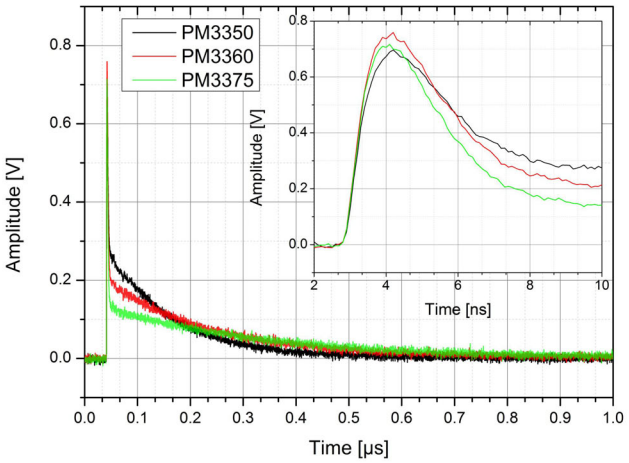

Figure 4.2.: Detector signal of PM33** under illumination with a 405 nm Laser pulse (60 ps FWHM). The intensity of the laser was set to a level at which the detector is fully saturated.

to the tail of the waveforms (cf. tab. 4.3). A long recovery time and therefore cell recharge time passively suppresses the afterpulse occurrence since charge carriers are released before the cell has been recharged. But on the other side, pile-up is more likely. For applications with a high count rate, this may be not acceptable. Fig. 4.3 shows the SiPM capacitance C_{SiPM} versus bias voltage. The resulting cell

Table 4.3.: Waveform and cell characteristics of PM33**.

	Rise Time [ps]	**Area Fast** [nVs]	**Area Total** [nVs]	$\mathbf{C}_{\mathrm{cell}}$ [fF]	$\mathbf{R}_{\mathrm{cell}}$ [kΩ]	τ [ns]
PM3350	665	2.0	40.6	270	540	145
PM3360	690	2.2	42.0	405	510	208
PM3375	700	2.1	37.2	650	500	327

capacitance is $\mathrm{C}_{\mathrm{cell}} = C_{\mathrm{SiPM}}/N_{\mathrm{cells}}$ where $\mathrm{C}_{\mathrm{cell}}$ includes the parasitic capacitance of the polyresistor, which is about 5% of the total capacitance. The included

contribution of the parasitic capacitance of the substrate to the metal lines, which connect the cells, is negligible [CDM+07]. The product of resistance and cell capacitance gives a result very close to the measured and fitted recovery time (cf. tab. 4.3). The slight variation of C_{SiPM} between the different devices could be caused by their differences in geometrical fill factor and parasitic capacitance.

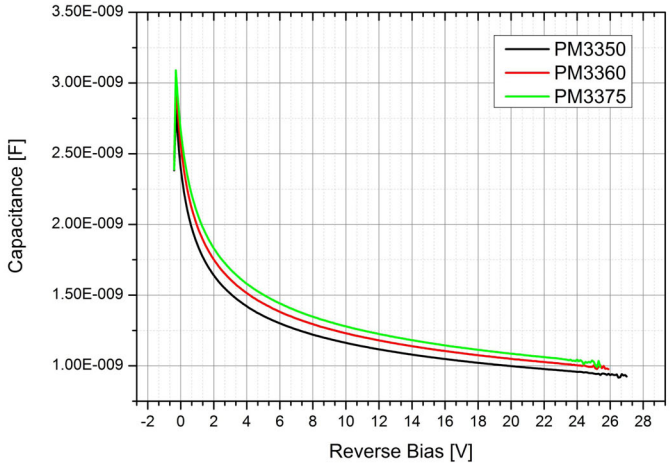

Figure 4.3.: Capacitance of PM3350, PM3360 and PM3375 versus reverse bias.

4.4.2. Breakdown Voltage, Temperature Dependency and Gain

Fig. 4.4 and 4.5 show the reverse I-V curve and its normalized differential slope $dI/dV \cdot 1/I$ indicating the operating range of the devices which is in between the spikes of the curve. All three types have a similar breakdown voltage and at least an operation range of 4.6 V overvoltage. A high temperature dependency demands for bias voltage regulation to compensate temperature changes. PM33** show a small temperature dependency of the breakdown voltage $dV/dT < 16$ mV/K (cf. tab. 4.4). In comparison, the reported value for a HPK MPPC S10362-33-050C is $dV/dT = 58.5$ mV/K [DBC+10], for HPK MPPC S12572-050 $dV/dT = 60$ mV/K [Ham14], for the SensL B-Series $dV/dT = 21.5$ mV/K [Sen13] and for FBK (RGB and NUV technology) $dV/dT = 25$ mV/K [PFG+13]. This may diminish the demand for a voltage regulation circuit with temperature since the gain variation with temperature is $< 1\%$ for an overvoltage $U_{\mathrm{over}} > 1.7$ V (cf. fig. 4.7). Noticeable is also the high gain $M > 6 \cdot 10^6$ which, depending on the application, reduces the need for a preamplifier.

4.4.3. Photo Detection Efficiency (PDE)

The investigated PM33** show high PDE of 49-55% at 405 nm (cf. fig. 4.8) and are therefore matching well with LYSO (420 nm). For the use with GAGG

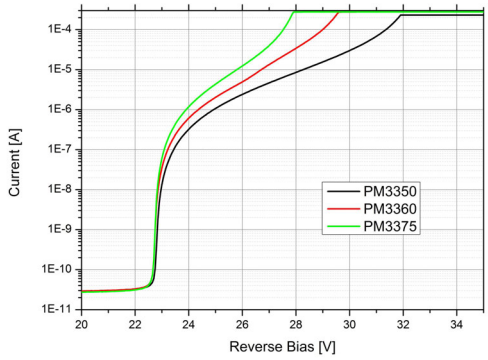

Figure 4.4.: Reverse biasing for PM33**.

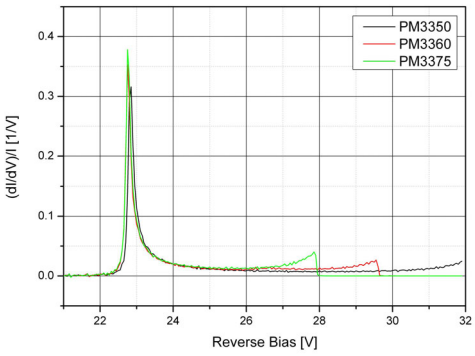

Figure 4.5.: $dI/dV \cdot 1/I$ for PM33**.

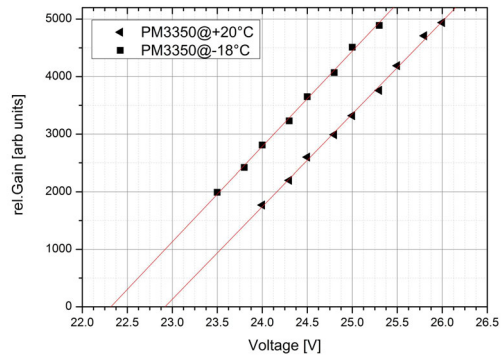

Figure 4.6.: Breakdown voltages of PM3350 determined by the intercept between linear interpolation of the relative gain and the bias voltage axis.

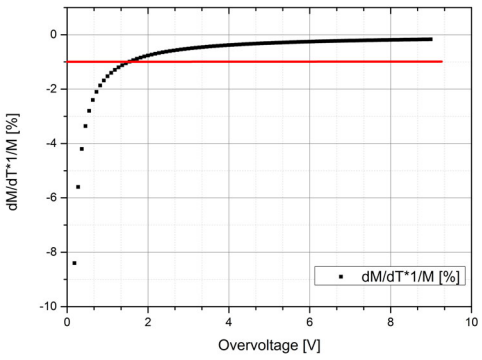

Figure 4.7.: Temperature coefficient of the gain M of PM3350 versus overvoltage.

Table 4.4.: Breakdown voltages, temperature dependency and absolute gain.

	$\mathbf{V_{bd}}$ **@ 20°C** [V]	$\mathbf{V_{bd}}$ **@ -18°C** [V]	**Temp. Dep.** [mV/K]	**Gain @ 4V OV** [10^6]
PM3350	22.86	22.30	14.7	6.7
PM3360	22.77	22.24	14.0	10.1
PM3375	22.65	22.05	15.8	16.3

(520 nm) the PDE is 29-33%. As expected, the PDE of all evaluated SiPMs is proportional to the geometrical efficiency (cf. tab. 4.1). The asymptotic behaviour of the curves at high overvoltages can be interpreted as a saturation of the Geiger probability. In comparison at 420 nm, the HPK MPPC S10362-11-050 (50 μm cells) has a reported maximum PDE of 32% [ESCS+10][VBD+11], latest HPK MPPC S12572-050 (50 μm) has 37% [Ham14], FBK RGB-HD (15 μm) reaches 24% [PFG+13] and SensL MicroB-30035 (35 μm) shows 41% [Sen13]. The relative spectral response of PM3350 is given in fig. 4.9 and can be scaled by the absolute PDE for all evaluated SiPMs. This measurement was performed with the 50 μm device at 3.4 V overvoltage.

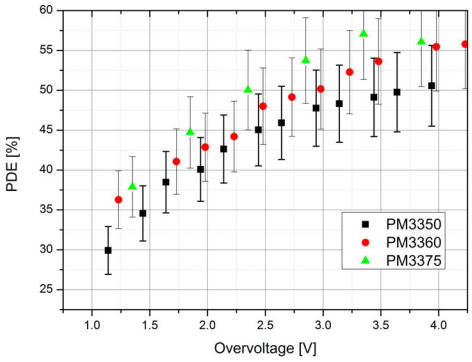

Figure 4.8.: Absolute photodetection efficiency for all tested SiPMs at 405 nm.

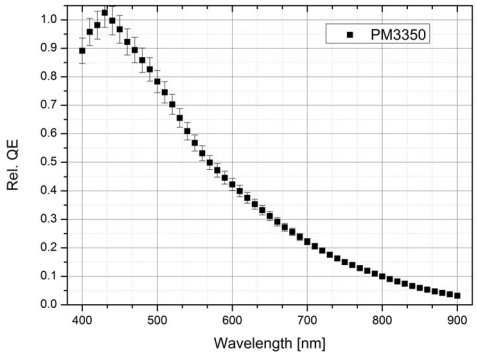

Figure 4.9.: Relative quantum efficiency of PM3350 versus wavelength at 3.4 V overvoltage.

4.4.4. Dark Count Rate (DCR)

The DCR of the SiPMs is between 340 kHz/mm^2 and 450 kHz/mm^2 at 20°C and 3.4 V overvoltage. Fig. 4.10 shows that the PM33** with larger microcells also show higher DCR and fig. 4.11 shows the DCR with increasing threshold level. In comparison at room temperature, HPK MPPCs (S10362-11-050C) show ≈ 1 MHz/mm^2 at an overvoltage of $U_{\text{over}} = 1.3$ V [ESCS+10] and the latest HPK MPPCs S12572-050 show ≈ 100 kHz/mm^2 [Ham14].

4.4.5. Crosstalk Probability (CTP)

Results for the CTP versus the bias voltage are shown in fig. 4.12. The dependency between microcell capacitance C, microcell area A (cf. 4.2) and CTP is reflected, e.g. the ratio $C_{\text{PM3375}}/C_{\text{PM3350}} \sim A_{\text{PM3375}}/A_{\text{PM3350}} = 5625\,\mu\text{m}^2/2500\,\mu\text{m}^2 = 2.25$ and $\text{CTP}_{\text{PM3375}}/\text{CTP}_{\text{PM3350}} = 42\%/20\% = 2.1$ at 3.4 V overvoltage are almost equal. The high gain of the SiPMs results in several hundred photons emitted per

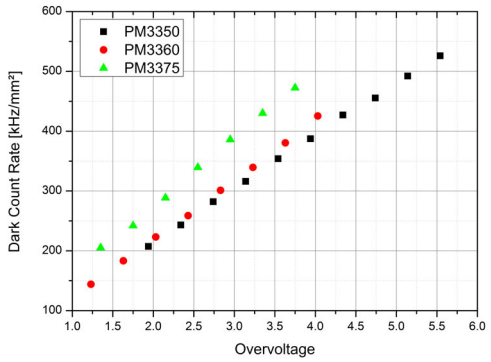

Figure 4.10.: Dark count rates mm^2 of all investigated SiPMs.

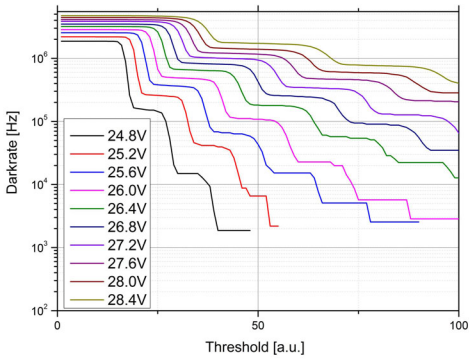

Figure 4.11.: Dark count rate versus threshold level.

avalanche, assuming about 3 photons per 10^5 generated charge carriers according to [aLZBM93].

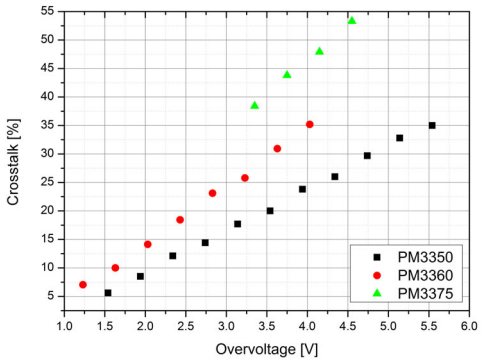

Figure 4.12.: Crosstalk probability versus bias voltage for PM3350.

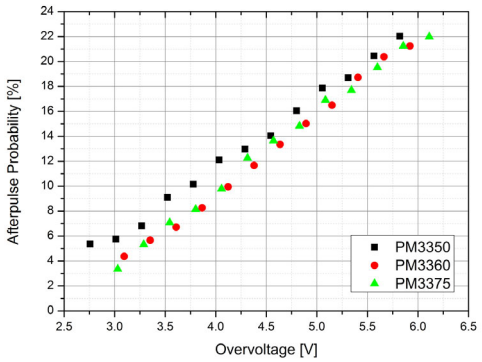

Figure 4.13.: Afterpulse probability versus overvoltage measured at -20°C.

4.4.6. Afterpulse Probability (AP)

Fig. 4.13 shows the AP at -20°C. At a $U_{\mathrm{over}} = 3.4$ V the AP is $< 7 \pm 2\%$ for all three SiPMs. No dependence on the microcell size was observed.

4.4.7. Single Photon Time Resolution (SPTR)

Fig. 4.14 presents the SPTR results where PM3350 performed best with 230 ps. All devices are illuminated over the full active area and only single pe pulses are

taken into account. These results are in agreement with another publication about KETEK SiPMs [BGM+13].

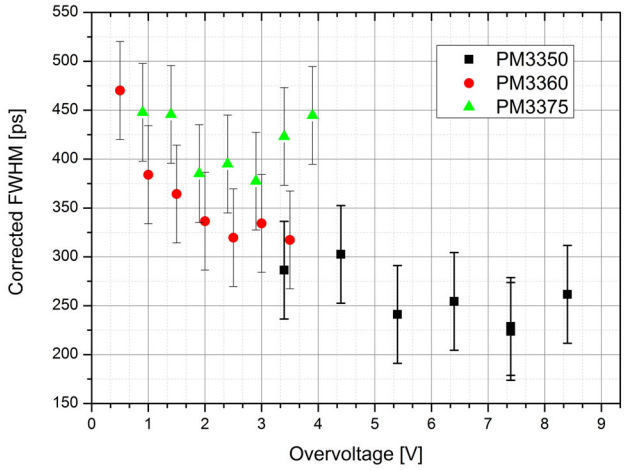

Figure 4.14.: Single photon time resolution as function of overvoltage for all microcell types.

4.4.8. Measurements with LYSO and GAGG

4.4.8.1. Energy Resolution

The energy spectra of ^{22}Na recorded with PM33** and LYSO or GAGG all show the 511 keV photopeak. As expected, saturation effects become visible caused by the limited number of cells compared to the high number of photons emitted from both scintillators. The histograms of the pulse area in fig. 4.15 of e.g. PM3350 at different overvoltages clearly show that the 1.275 MeV photopeak of ^{22}Na is not 2.49 times larger in pulse area as it would be for the linear case. Thus for a comparison the energy resolution is corrected for saturation (cf. tab. 4.5). The FWHM were obtained after subtracting the high-energetic Compton background of ^{22}Na under the photopeak. $\Delta E/E$ is better for higher overvoltages since the PDE increases. GAGG has a better intrinsic energy resolution than LYSO. Therefore, more photons are detected resulting in stronger saturation which is visible in the stronger squeezing of the spectrum (cf. fig. 4.15). In addition, with a decay time of about a factor 2 for GAGG compared to LYSO, the microcells are more likely to recharge during the light emission from the crystal. In the case of LYSO with its faster decay, cells are more likely to be hit by a photon while they are recharging from a previous breakdown. With increasing cell size, the saturation gets stronger due to less cells. PM3360 and PM3375 showed very strong squeezing especially for higher energies making the 1.275 MeV peak of ^{22}Na unidentifiable. This was the reason to exclude those in tab. 4.5.

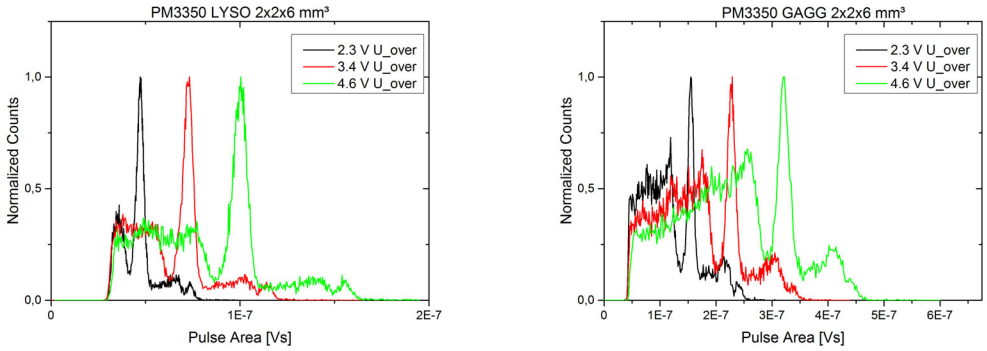

Figure 4.15.: Energy spectra of ^{22}Na recorded by a PM3350 coupled to a LYSO or GAGG scintillator crystal at different overvoltages. Noticeable is the saturation of the SiPM resulting in a non-linear response.

Table 4.5.: Energy resolution of PM33** with LYSO and GAGG at different overvoltages and saturation corrected values.

	$\Delta E/E$ **FWHM** [%] **at 511 keV**					
	uncorrected			saturation corrected		
U_{over}	2.3 V (10%)	3.4 V (15%)	4.6 V (20%)	2.3 V (10%)	3.4 V (15%)	4.6 V (20%)
	LYSO $2 \times 2 \times 6$ mm^3					
PM3350	9.3	8.8	8.4	13.5	12.8	12.3
PM3360	9.2	7.8	7.3	16.2	13.4	14.1
PM3375	8.0	7.1	6.1	14.5	13.5	12.4
	GAGG $2 \times 2 \times 6$ mm^3					
PM3350	7.3	7.2	7.2	10.8	11.1	12.3

4.4.8.2. Coincidence Time Resolution (CTR)

Tab. 4.6 summarizes the results of two SiPMs in coincidence, coupled either to LYSO or GAGG. For GAGG only the measurement with PM3350 could be performed because PM3360 and PM3375 were in saturation which did not allow to set a reliable energy filter for 511 keV. This was also the case for PM3375 with LYSO at 4.6 V overvoltage.

4.4.8.3. Comparison with Reported Values

Tab. 4.7 and 4.8 summarize the best achieved results with PM33** and compare them to reported results in literature for HPK, FBK and Sensl SiPMs. The saturation corrected energy resolution is worse with PM33** compared to the other manufacturers, while the uncorrected values are comparable or better. A higher saturation of PM33** is also indicated by the saturation correction factor for the energy resolution. A reason could be that PM33** has a higher PDE than the other manufacturers which increases the probability to saturate the device

Table 4.6.: Coincidence time resolution of PM33** with LYSO and GAGG at different overvoltages.

	CTR FWHM [ps]			
U_{over}	1.7 V (7.5%)	2.3 V (10%)	3.4 V (15%)	4.6 V (20%)
	LYSO $2 \times 2 \times 6\ mm^3$			
PM3350	245	207	174	187
PM3360	241	178	180	180
PM3375	157	179	158	
	GAGG $2 \times 2 \times 6\ mm^3$			
PM3350	501	491	430	

more. In addition the single cell pulse decay time $\tau > 145$ ns is quite long (cf. tab. 4.4), which makes it very likely that cells are not fully recharged when hit again by a photon during a scintillation event, which results in less detected charge. This leads to effectively less detected photons and thus a worsening in photon statistics respectively energy resolution. In comparison, for HPK MPPCs a decay time value of 11 ns for a 50 μm SiPM has been reported [OOY+07].

Table 4.7.: Comparison of the currently best reported energy resolutions in literature with LYSO and GAGG. In brackets are the corresponding values without saturation correction.

	$\Delta E/E$ **FWHM** [%] **at 511 keV**					
	KETEK			HPK MPPC	FBK	Sensl
	PM3350	PM3360	PM3375	S10362-33-050 [YYD+13]	RGB-HD [FGS+14b]	MicroFB-30035
Crystal [mm^3]	$2 \times 2 \times 6$			$3 \times 3 \times 5$	$3 \times 3 \times 5$	$2 \times 2 \times 6$
LYSO	12.3 (8.4)	13.4 (7.3)	12.4 (6.1)	- (10.1)	9.5 (-)	
GAGG	10.8 (7.3)			7.9 (7.1)	7.0 (-)	10.7 (8.3)

Table 4.8.: Comparison of the currently best reported CTR in literature with LYSO and GAGG.

	CTR FWHM [ps]					
	KETEK			HPK MPPC	FBK	Sensl [DFI13]
	PM3350	PM3360	PM3375	S10362-33-050	RGB-HD [FGS+14b]	MicroFB-30035
Crystal [mm^3]	$2 \times 2 \times 6$			$3 \times 3 \times 5$	$3 \times 3 \times 5$	$3 \times 3 \times 10$
LYSO	174	178	157	138 [SvDV+12]	157	180
GAGG	430			464 [YYD+13]	255	

4.5. Conclusion

Recently developed blue sensitive SIPM have been characterized and show promising performance for the use in PET. PM33** SiPMs have an operating voltage

$>$ 23 V and the devices have a large operation range of up to 6 V overvoltage. PDE, crosstalk, afterpulses and dark count rates are either comparable or better than other available SiPMs. The unique feature of the SiPMs is their small temperature dependency. Together with the large bias operation range, this opens new possibilities in applications where material or occupied space matters, since a bias voltage regulation is not absolutely necessary when operating under temperature changes of several degree K. With a typical gain of $7 - 16 \cdot 10^6$ at an overvoltage of 4 V and using a bright scintillator like LYSO, the signals at 50 Ω have an amplitude of several hundred mV. Depending on the application a further amplification of the signal may not be needed. With these properties, the SiPMs are promising candidates for the use in combined ToF-PET/MRI.

4.6. Acknowledgements

The authors would like to thank Dr. Florian Wiest from KETEK for providing the SiPMs and Prof. Dr. Kei Kamada from C&A Corporation for providing the GAGG crystals.
The research leading to these results has received funding from the European Union Seventh Framework Program (FP7) under Grant Agreement No. 294582 ERC Grant MUMI.

5. Simulation Studies of MADPET4 - A Design Concept for an MRI compatible PET Insert with Individually read out Crystals

Abstract: MADPET4 (Munich Avalanche Photodiode PET) is a PET (positron emission tomography) insert proposed for the use in a 7T small animal MRI (magnetic resonance imaging) scanner. It is a dual layer ring system allowing DOI (depth of interaction) with individually read out LYSO (Lutetium Yttrium Oxyorthosilicate) scintillator crystals with an end face of 1.5×1.5 mm^2. MADPET4 consists in total of 8 axial dual layer rings with 330 crystals per ring and an inner diameter of 98.8 mm. The crystals are arranged such that every crystal is transaxially facing the center of the FOV (field of view), so only photons emitted close to the center of the FOV have the possibility to escape the ring in transaxial direction without passing any crystal volume. Compared to a block-wise approach with crystal arrays, the proposed geometry allows a larger crystal volume in the ring by minimizing the gaps leading to a more uniform sensitivity. Different possible crystal lengths for inner and outer layer have been simulated with GATE (Geant4 Application for Tomographic Emission) to find the optimal configuration with focus on highest possible spatial resolution and still good sensitivity. The total crystal length of inner and outer ring is 20 mm. A configuration with 6 mm long crystals in the inner layer and 14 mm in the outer layer showed the best performance in terms of spatial resolution. A phantom with spherical sources (radius 0.1 mm) embedded in a background activity of 1/200 of the spheres has been simulated. With an iterative MLEM (Maximum Likelihood Expectation Maximization) reconstruction a spatial resolution of < 1 mm in the center of the FOV and < 2.3 mm at 80% of the FOV could be achieved.

5.1. Introduction

5.1.1. System Properties

MADPET4 is designed as an insert for the 7 T MRI Agilent/GE Discovery MR901 for preclinical small animal studies. It is a dual layer PET system with an inner ring composed of 132 scintillator crystals and 198 crystals for the outer ring, providing DOI information by the two layer concept [MPP+05][Spa07]. The functional requirements for the system are maximum channel density, high spatial resolution of < 3 mm for a large FOV (field of view), a total system CTR (coincidence time resolution) < 3 ns and as much as possible uniform sensitivity throughout the FOV. The usable FOV should encompass up to 80% of the inner diameter. Due to the constraints inside the MRI scanner, SiPMs (Silicon Photomultiplier) are the detector of choice since they are insensitive to magnetic fields, compact and show high intrinsic gain $> 10^6$. The inner diameter is 98.8 mm and the outer diameter is 140 mm, measured from the crystal end faces, leaving enough space to place the detectors to fit into the MRI Tx/Rx coil with 150 mm inner diameter. The crystals with an end face of 1.5×1.5 mm^2 are read out individually for high count rate capability, direct interaction localization and the possible use of inter-crystal scattered events. They are not arranged in blocks or arrays as in most traditional approaches but are transaxially facing the center of the field of view with as much symmetry as possible (cf. fig. 5.1) aiming for a more uniform sensitivity due to the minimal gaps. The MRI scanner induces constraints like the magnetic field and space limitations. SiPMs are already proven to work in PET and in simultaneous PET/MRI [DKH+14]. They are compact, have high PDE (photodetection efficiency), a high gain $> 10^6$, are usable without preamplification and therefore no need for active electronic PET components inside the MRI. Latest generation SiPMs have lower temperature dependency of the gain and have a large operating voltage range up to 40% overvoltage [SGS+14]. Both properties lead to less system complexity since many SiPMs can be operated with the same bias voltage and a recalibration of the energy spectra is not needed for the expected temperature variations. Consequently the front end can be kept minimal by consisting of the scintillator crystals and the SiPMs while the PET electronics is planned to be outside the MRI. The complete system will consist of 8 axial rings with a total of 2640 channels. Since the inner diameter from crystal to crystal is only 98.8 mm, time-of-flight measurement is not the main objective. Instead the focus is on best possible spatial resolution with sufficiently good time resolution for randoms suppression and sufficiently good energy resolution for recovering inter-crystal scattered events. The combination of SiPMs and LYSO fulfills these requirements and is compatible to work inside an MRI scanner [DKH+14].

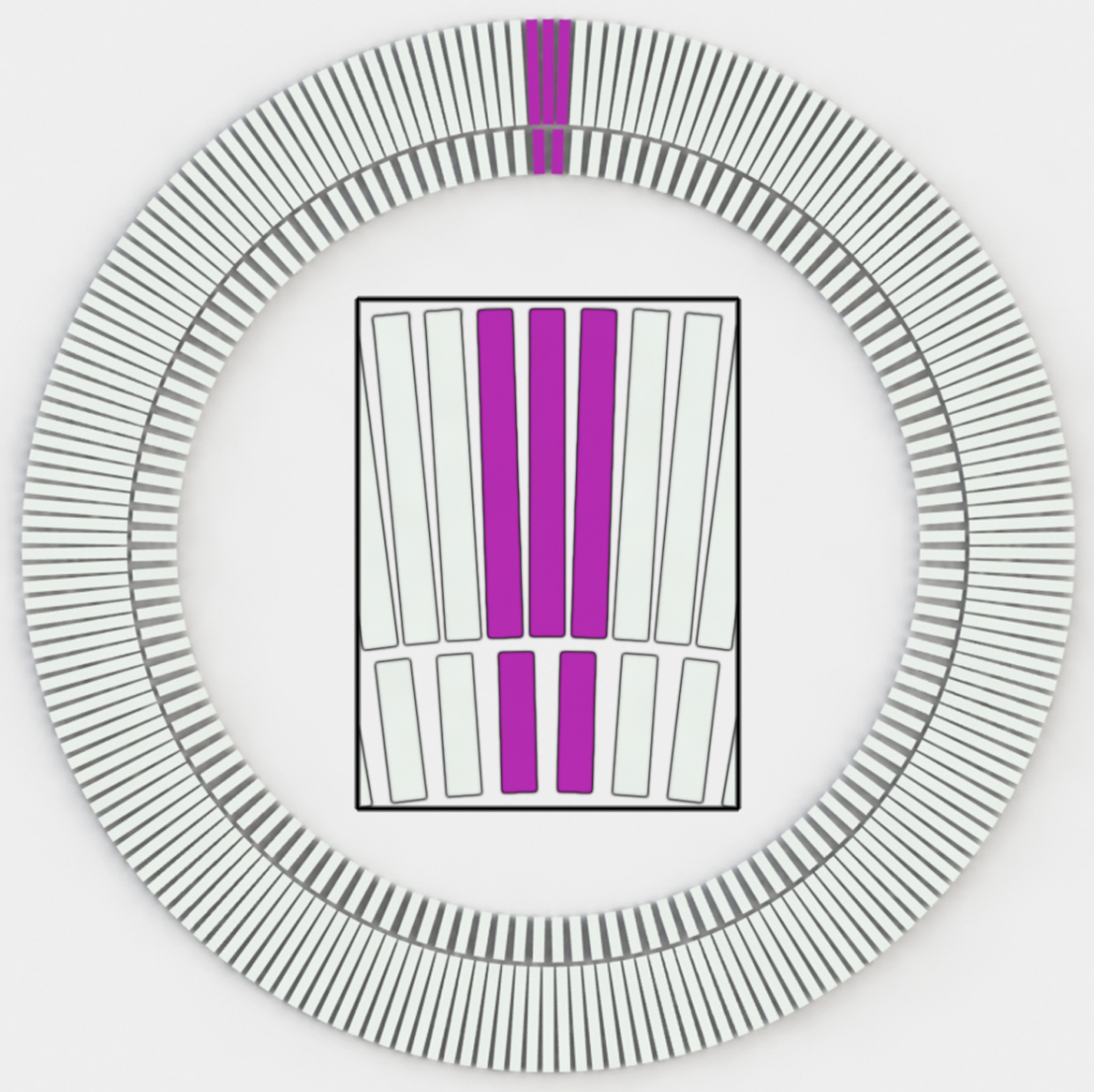

Figure 5.1.: Single PET ring of MADPET4 with 330 crystals (*grey*, end face 1.5×1.5 mm^2). The basic element of the ring is shown in *violet*. Inner diameter is 98.8 mm and outer diameter is 140 mm.

5.1.2. Aim of this Work

The main goal of this simulation was to find the optimal combination of the crystal lengths for inner and outer ring with priority on spatial resolution up to 80% of the FOV. In total five different dual layer combinations of crystal lengths with a total length sum of inner and outer crystal of 20 mm have been investigated (inner-outer lengths in mm): 4-16, 5-15, 6-14, 8-12 and 10-10. For comparison without DOI information, also a single layer variant 0-20 with 20 mm long crystals in the outer layer and no crystal in the inner layer was simulated. The 20 mm total crystal length is the same as e.g. for the Siemens mMR [DFJ+11b] and was chosen as a compromise between sufficient stopping probability and space constraints due to the small ring diameter. The sensitivity should still be as uniform and high as possible. The optimal configuration should also be investigated with a more complex phantom.

5.2. Methods

All simulations were performed using parallel GATE 6.1 [RVAE13] on a 48 core Linux cluster. An energy resolution of 11.75% FWHM (σ = 5%) @ 511 keV, estimated from first measurements with potential SiPM candidates and LYSO, has been set. The time resolution has been conservatively estimated to be 3 ns and a 6 ns coincidence window was used. With a lower energy threshold of 450 keV, which is set to include only events in the photopeak, inter-crystal scattered events are not detected to simplify the analysis. To speed up the computations, the presented results have all been obtained by simulating one ring instead of all 8 of MADPET4, with 330 crystals for the dual layer configurations (4-16,5-15,6-14,8-12,10-10) and 192 crystals for the single layer configuration (0-20).

5.2.1. Analytical Detector Response Function Model

An iterative reconstruction based on Maximum Likelihood Expectation Maximization (MLEM) was used [SV82] with system matrices (SM) analytically calculated with the detector response function (DRF) model (cf. tab. 5.1). The SM generation and the MLEM were implemented on a multi-core architecture [KWS09]. The basic idea of the DRF model presented by Strul et al. [SSD+03] is to calculate the probability $p_c(M, n)$ of a flux of photons from a source point M travelling in direction n being detected by detector crystal c. To evaluate the differences in terms of sensitivity between the investigated geometries, a sensitivity map was calculated which represents the weighting of the voxels in the system matrix.

5.2.2. Phantoms

Spatial Resolution For each scanner geometry, spherical sources (radius 0.1 mm, each sphere 1 MBq) embedded into an ellipsoidal background activity (halfx =

Table 5.1.: Properties of the calculated system matrices for 1 ring of MADPET4.

crystals	330 (for 0-20: 192)
LORs	108900 (for 0-20: 36864)
voxels	$246 \times 246 \times 1$
voxel size	$0.375 \times 0.375 \times 1.5$ mm^3
file size	425 - 716 MB

24.0 mm, halfy = 2.5 mm, halfz = 0.75 mm) were simulated for 60 s (cf. fig. 5.2). One spherical source without added background has been placed exactly in the center of the FOV to confirm the correct localization of the sources in the reconstructed image. The background ellipsoid had an activity concentration of 1/200 of the spheres. The sources were modeled as two monoenergetic 511 keV gammas, back-to-back with isotropic emission. The relative sensitivity of the different geometries was extracted. As a measure for the spatial resolution, Gaussian functions were fitted to the line profile through the reconstructed spherical sources and the FWHM were determined.
To find the optimal number of iterations for this study, the same spherical sources without background have been simulated and reconstructed with 10 to 150 iterations in steps of 10 iterations. Since all spheres have the same activity, their peak heights in a line profile through the central slice of the reconstructed image should be similar. The number of iterations for this study has been chosen according to this.

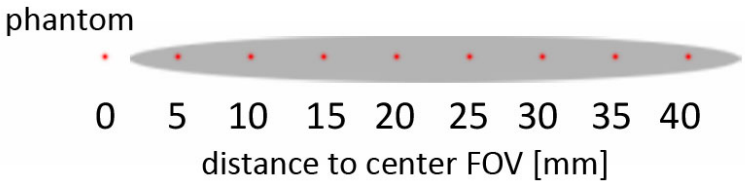

Figure 5.2.: Phantom to investigate the spatial resolution up to 80% of the field of view. The background ellipsoid's (*grey*) activity concentration is 1/200 of the hot spheres (*red*).

Derenzo Phantom To evaluate the performance of the best variant with a more complex phantom, a GATE simulation of a Derenzo phantom with the outermost rod at 87 % of the FOV was performed. The total activity of 37 MBq was distributed to a uniform activity concentration in the hot rods and the phantom has been simulated for 5 min. The sources were two 511 keV gammas, back-to-back with planar emission, and the material of the phantom was defined to be air.

5.3. Results and Discussion

5.3.1. Sensitivity

The different sensitivity maps and line profiles for each geometry are shown in fig. 5.3 and 5.4. The relative sensitivity is highest for the variant 0-20 without DOI which is expected, since it has the largest crystal volume (cf. tab. 5.2). Also lower sensitivity due to smaller crystal volume is seen with shorter crystals in the back layer, since the number of crystals for the outer layer (198) is 1.5 times higher than for the inner layer (132). By calculating the relative standard deviation of the sensitivity up to 80% of the FOV, the uniformity is indicated, where 6-14 and 8-12 show the best performance out of the dual layer variants.

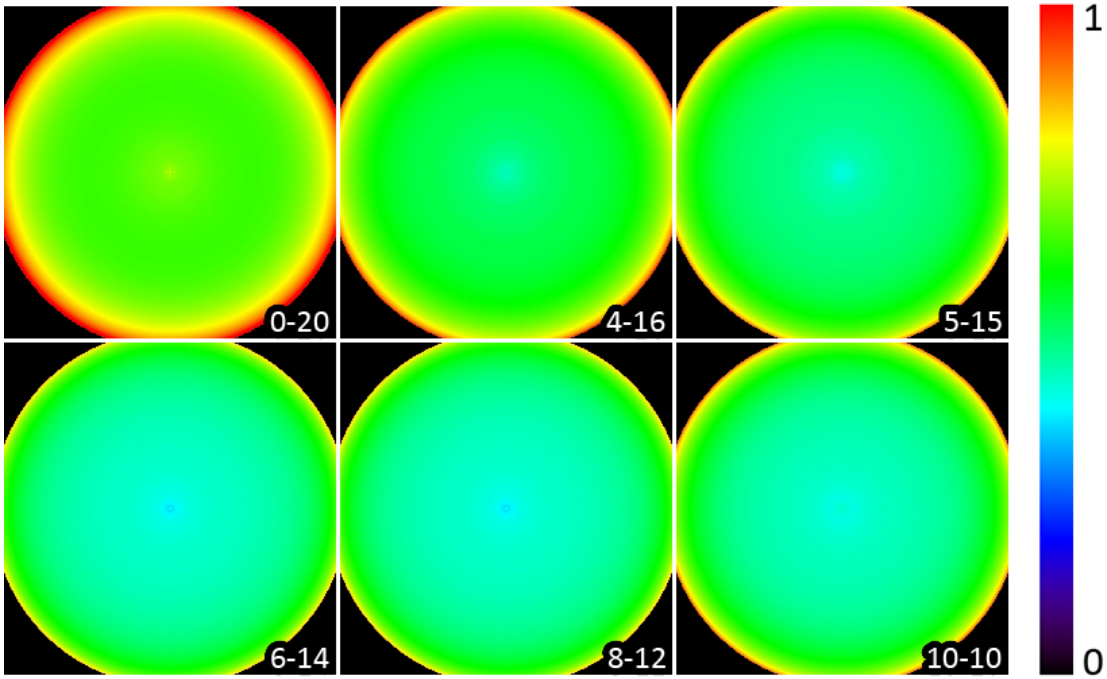

Figure 5.3.: Sensitivity maps of the system matrices computed with the DRF model. Numbers correspond to the different length combinations of inner and outer layer crystals. Plots are normalized to the same color scale.

5.3.2. Spatial Resolution

5.3.2.1. Spherical Sources

Without Background In the case of 50 iterations the peak heights are almost equal (cf. fig. 5.5). Concluding from this, all further simulations have been evaluated at 50 iterations.

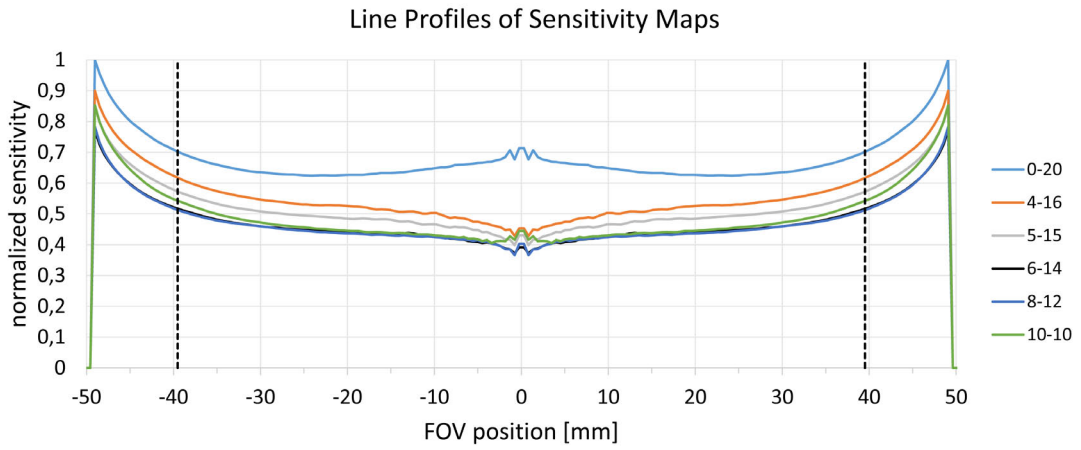

Figure 5.4.: Line profiles through the central slice of the sensitivity maps shown in fig. 5.3. The dashed lines indicate 80% of the FOV.

Table 5.2.: Relative sensitivities of the different geometries and the relative standard deviation of the sensitivity change within 80% of the FOV.

geometry	rel. sens. [%]	rel. std. dev. [%] (80% FOV)
0-20	100.0	3.4
4-16	95.2	7.7
5-15	93.7	7.4
6-14	92.2	6.8
8-12	88.7	6.6
10-10	86.6	7.2

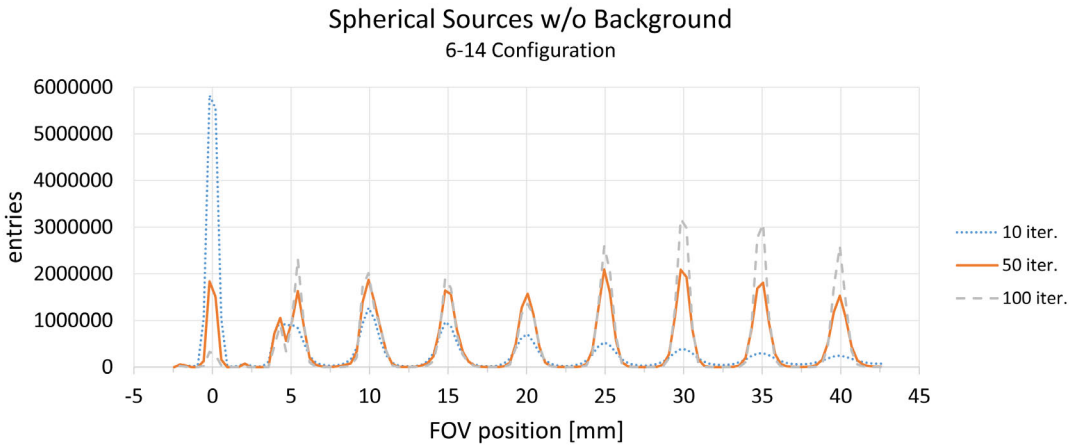

Figure 5.5.: Comparison of the peak heights of a line profile through the MLEM reconstructed spherical sources with different iterations. For better visibility, only 10, 50 and 100 iterations are shown. 50 iterations show the best uniformity between the peak heights.

With Background 1:200 50 iterations MLEM showed the most uniform weighting of the peak heights amongst each other as with 150 iterations no further improvement in the extracted FWHM could be observed. Concluding from figure 5.6, the variant 6-14 outperforms 4-16, 5-15 and 8-12. It shows the lowest parallax effect with all FWHM < 2 mm for 150 iterations and sub-millimeter resolution in the center of the FOV.

Comparison without DOI The geometry (0-20) with no inner crystals and only 20 mm long outer crystals (198 crystals) shows only the 5 innermost spherical sources (from the center of the FOV up to 20 mm away). Further ones could not be distinguished anymore from the background (cf. fig. 5.7). The FWHM at 20 mm distance was already around 4 mm. The 0-20 configuration also does not display the source position correctly anymore, instead there is an outwards shift. From the line profile in comparison with 6-14 with and without background it is clearly visible that the performance would be not acceptable without DOI. Therefore the dual layer concept with DOI is mandatory.

5.3.2.2. Derenzo Phantom

Figure 5.8 shows 50 iterations MLEM of a Derenzo phantom. All rods for 2.3 mm can still be clearly separated, while the rod diameter of 1.85 mm shows the limit of the spatial resolution for the two outermost rods (cf. fig. 5.9). The smallest rods with a diameter of 1.35 mm cannot be resolved anymore. This result confirms that the spatial resolution is < 2.3 mm which is in agreement with the result obtained by the spherical sources.

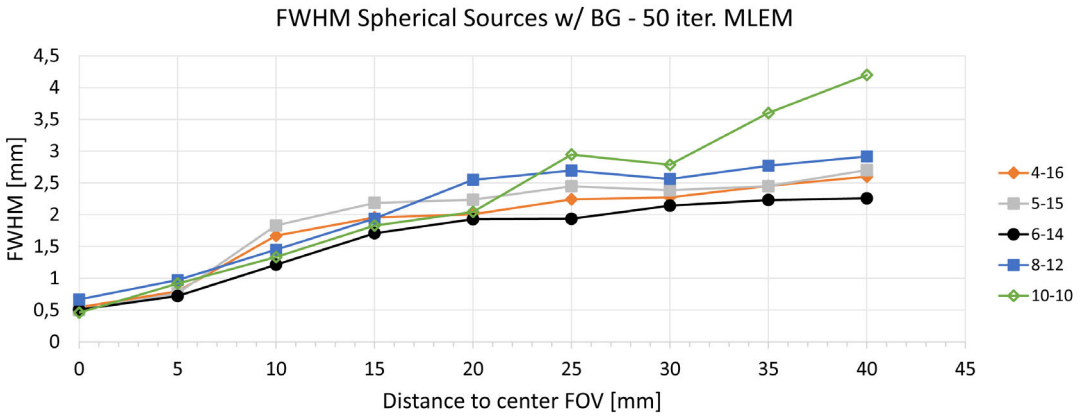

Figure 5.6.: Comparison of the spatial resolution for the different geometries with 50 iterations MLEM.

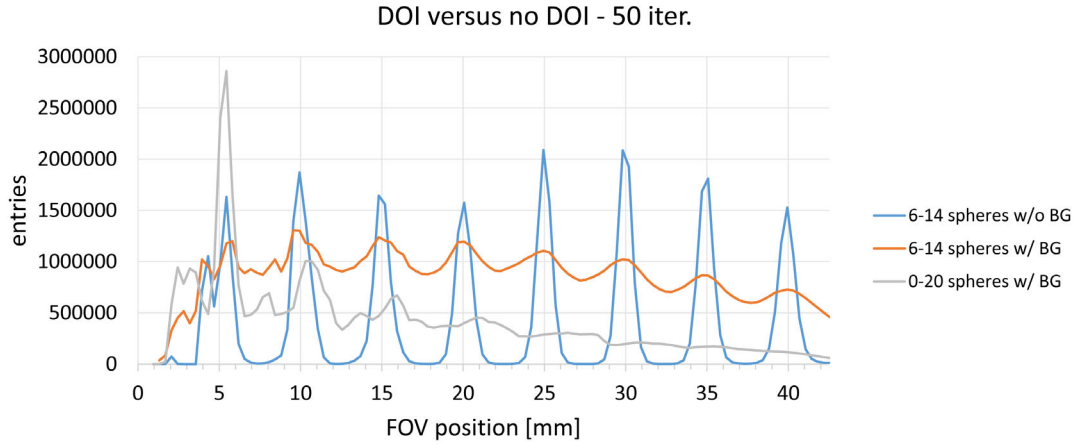

Figure 5.7.: Comparison of the line profiles through the spherical sources with (6-14) and without (0-20) DOI.

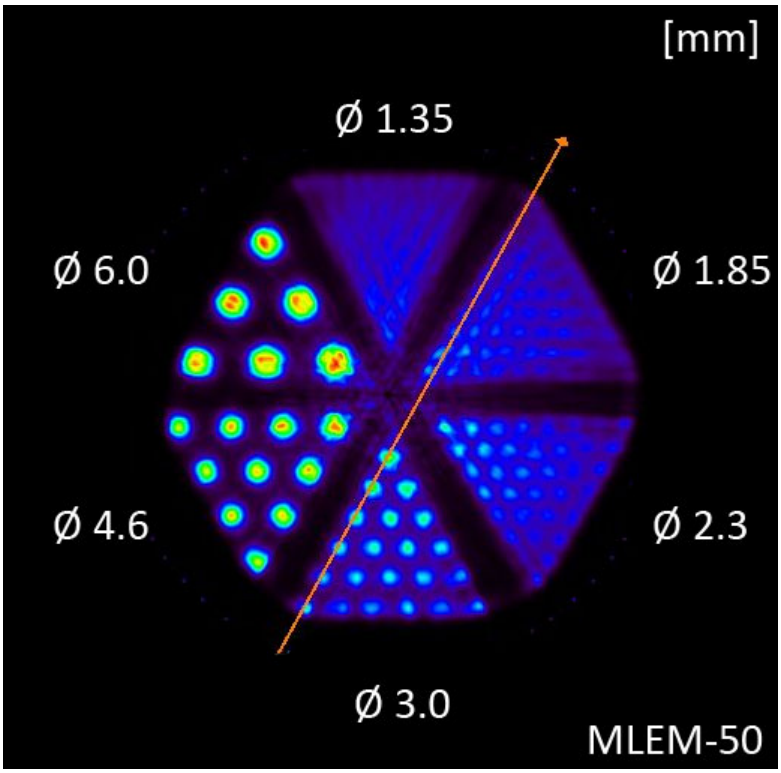

Figure 5.8.: MLEM reconstruction of the Derenzo phantom with 50 iterations.

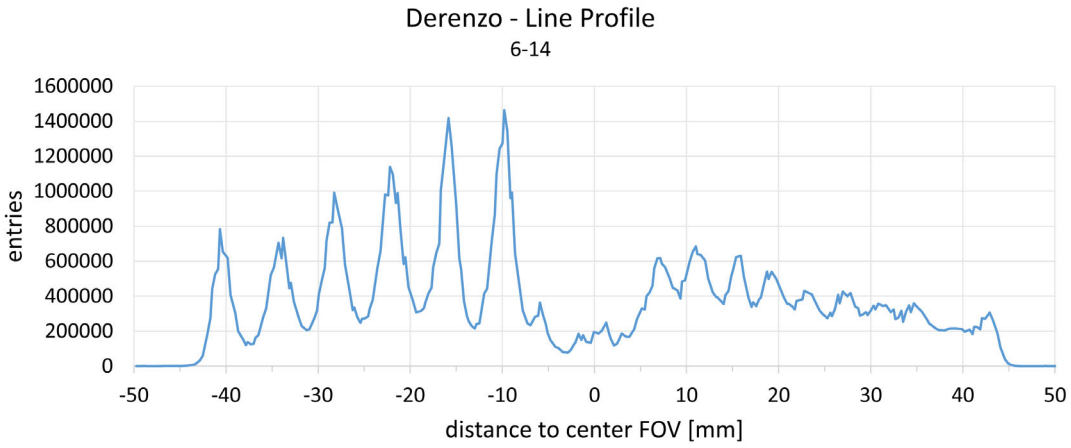

Figure 5.9.: Line profile through the slice indicated in fig. 5.8. All rods except the two outermost ones with a diameter of 1.85 mm can be clearly separated.

5.4. Conclusion and Outlook

The proposed design for a small animal PET scanner shows promising results. Compared to the traditional approach with block wise arranged scintillators in the PET ring [Hoh12, SSSSZ15], the sensitivity is more uniform since the overall crystal volume and placement in the available space are optimized to minimize gaps. DOI information can be extracted by the two layer concept paying off in a good spatial resolution up to 80% of the FOV. The best spatial resolution is shown by the configuration with a length of 6 mm for the inner and a length of 14 mm for the outer ring crystals. The relative sensitivity is comparable to the other variants and is amongst the best in terms of uniformity. The crystal arrangement already takes into account a possible readout with commercially available SiPMs and their package size [KETa]. Encouraged by these results the variant 6-14 is currently under development.

5.5. Acknowledgments

The research leading to these results has received funding from the European Union Seventh Framework Program (FP7) under Grant Agreement No. 294582 ERC Grant MUMI.
The authors also thank Melanie Hohberg for the introduction to the DRF computation.

6. MADPET4: A 3D printed, unshielded, MRI compatible Dual Layer PET Insert

Abstract: MADPET4 is a PET insert for a 7 T MRI Agilent/GE Discovery MR901 for preclinical small animal studies. As described in chapter 5, p. 65, it is a dual layer PET system with an inner layer composed of 132 LYSO crystals and 198 LYSO crystals for the outer layer per ring, providing quantized DOI information [MPP+05, Spa07, Esp08]. The crystals are $1.5 \times 1.5 \times 6$ mm^3 for the inner and $1.5 \times 1.5 \times 14$ mm^3 for the outer layer. Each crystal is read out individually by a KETEK PM1150NT SiPM with an active area of 1.2 mm $\times$ 1.2 mm. The complete system consists of 8 axial rings with 2.6 mm pitch, covering 19.7 mm in axial direction with a total of 2640 channels (cf. fig. 6.1).
The mechanical support structures are made from 3D-printed (laser-sintered) polyamide (PA-2200, $\rho \approx 0.9 - 0.95$ g/cm^3, EOS GmbH, Krailling/München). The complete design was made with CAD (Computer Aided Design, *SolidWorks*) and the manufacturing of the parts was done by *shapeways* [Sha]. The PCBs (Printed Circuit Board) with the SiPMs are mounted to the inner and outer crystal layer. The white printed parts hold the crystals, while the structural parts to mount the PCBs are printed in black for light tightness (cf. fig. 6.4). Altough the front end of MADPET4 is finalized and equipped with all components, with the currently available SADC (Sampling Analog to Digital Converter) DAQ (Data Acquisition) only two opposing modules (80 ch) can be read out. For the first PET only tests, MADPET4 has been set up outside the MRI. Then the insert was tested for its MRI compatibility and finally a simultaneous PET/MRI image was successfully acquired. It works inside the MRI Tx/Rx (Transmission/Receive) coil without any electromagnetic shielding for the PET components. In both cases, Na-22 point sources could be successfully reconstructed with iterative algorithms. The energy resolution at 511keV and CTR are 8.7% and 472 ps for the inner detectors, respectively 10.4% and 861 ps for the outer detectors (all values FWHM, $\Delta E/E$ not corrected for saturation). Currently the 80 MHz SADC read out limits the CTR to 9.6 ns FWHM. The final system will be equipped with TOT-ASICs (Time-over-Threshold Application Specific Integrated Circuit) which showed a CTR of 545 ps FWHM with a first test board and two inner detectors in coincidence. The read out platform for the TOT ASIC is currently under development.

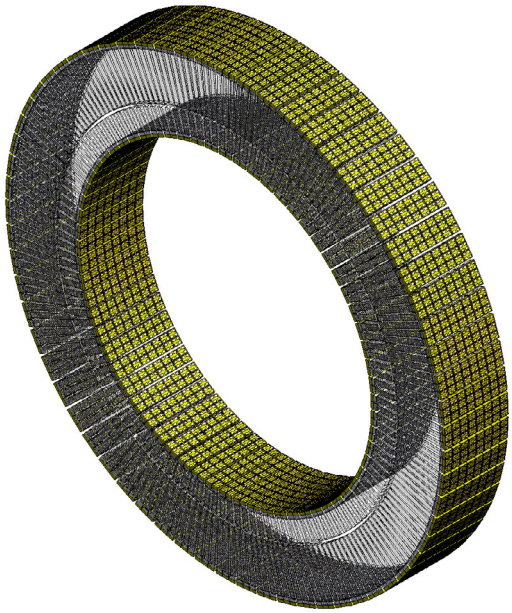

Figure 6.1.: Isometric view of MADPET4 with 2640 crystals (*grey*) read out individually by SiPMs (*green*). Inner ø 98.8 mm and outer ø 140 mm, measured from the crystal end faces.

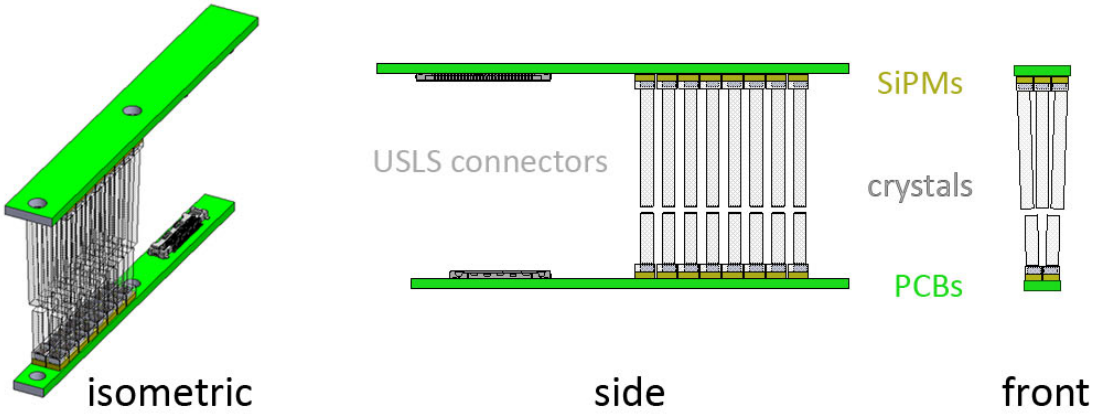

Figure 6.2.: Schematic views of a single module of MADPET4 with in total 40 detector channels. Pitch between the rings in axial direction is 2.6 mm, covering an axial FOV of 19.7 mm.

6.1. Materials and Methods

6.1.1. Technical Specifications of the MRI Scanner

The MRI scanner used is an Agilent/GE Discovery MR901 7T/31 with 7 T and 31 cm bore diameter. MADPET4 is designed to fit into the Tx/Rx coil with inner ø 150 mm. This coil is a Quadrature Actively Decoupled Birdcage optimized for ^{1}H (300 MHz). It is used inside a gradient sub-system with 300 mT/m peak amplitude with ø 210 mm inner bore. The coil has an RF window length of 150 mm, the coil housing itself has a length of 270 mm. The distance from the front face of the coil to the RF isocentre is 100 mm. The RF homogeneity has a linear region of 100×100 mm^2. [GA11]

6.1.2. Photodetectors, Scintillators and System Assembly

SiPMs MRI induces constraints like the magnetic field, radio frequency (298.1 MHz) and space limitations (bore ø150 mm). SiPMs are the detectors of choice since they are already proven to work in PET/MRI [DKH$^+$14, ETF$^+$08]. The used SiPMs are non-magnetic and nickel-free KETEK PM1150NT (NT no trench type) with 576 cells on an active area of 1.2×1.2 mm^2 and 50 μm cell pitch [KETa]. They are compact SMDs (Surface Mount Device) with high internal gain $\approx 8 \cdot 10^6$. Their temperature variation of the gain is $< 1\%$/K. With a bright scintillator like LYSO the pulse height is ~ 100 mV at 50 Ω. With those properties, there is no need for active electronic PET components, like e.g. a preamplifier or temperature compensation circuit, inside the MRI scanner. This allows the digitization of the signals outside the MRI without preamplification. Their typical breakdown voltage is 27.5 ± 0.5 V and they have a large operating voltage range $> 20\%$ overvoltage. Other advantages are their high PDE (Photo Detection Efficiency) of up to 55% at 420 nm and a package size of $2.45 \times 1.95 \times 1.8$ mm^3 [KETa].

Scintillators LYSO is suitable for operation inside an MRI scanner [EFH$^+$10]. The used crystals are produced by Hilger Crystals, UK. Detailed LYSO specifications can be found in section 1.3.3, p. 8.

PCBs The common breakdown voltage of all SiPMs leads to less system complexity since all SiPMs of a PCB (16 for inner, 24 for outer PCB) share a common bias voltage and their signals are routed individually by micro-coaxial cables (0.4 mm pitch, USLS series, KEL Corporation Japan) with 20 pins (inner) and 30 pins (outer PCB). The PCBs have no ground connection to avoid building an antenna inside the MRI which catches. From the inner 20 pins, 16 pins are for the single ended detector signals and 4 for the bias voltage, for the outer 30 pins there are 24 pins used for the signals and 6 for bias. The PCBs consist of 6 layers with 125μm manufacturing precision, have a thickness of 1.25 mm and have been designed with *Altium Designer ECAD*). Figure 6.3 shows the individual parts.

The PCBs are mounted onto the insert structure with the embedded crystals as shown in fig. 6.4 and are also used to hold the parts together. All 80 SiPMs of the two used modules (cf. fig. 6.2) were operated with one common power supply line.

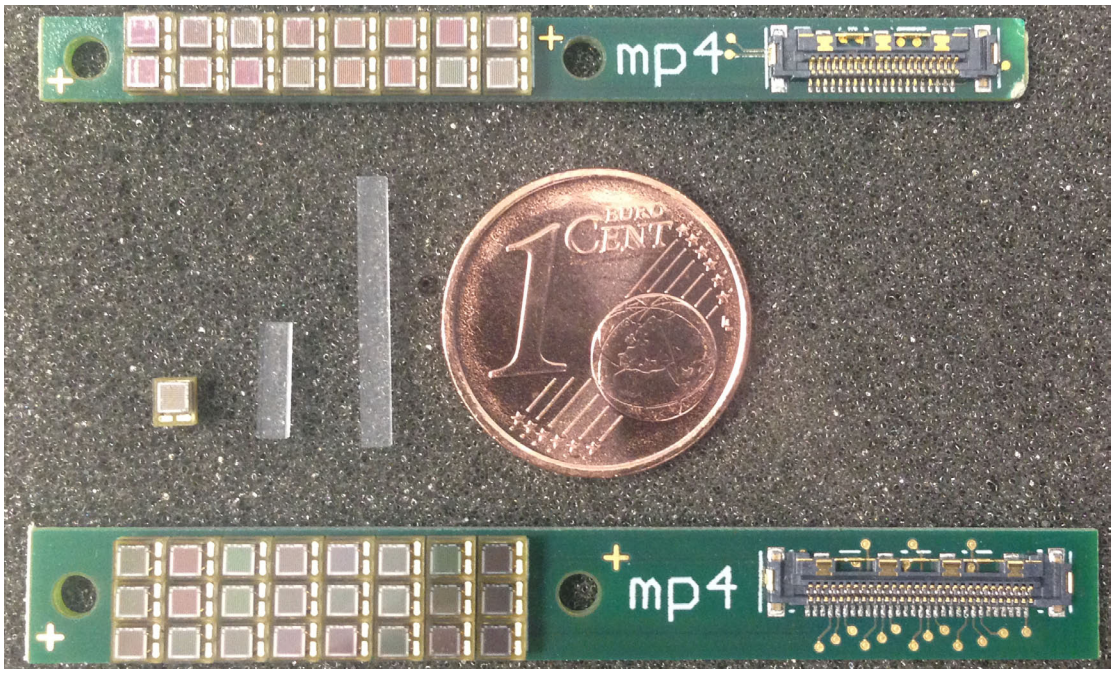

Figure 6.3.: Inner (*top*) and outer (*bottom*) PCBs with SiPMs and USLS connectors, single PM1150NT, $1.5 \times 1.5 \times 6$ mm^3 and $1.5 \times 1.5 \times 14$ mm^3 LYSO crystals and a size comparison to a 1 Cent coin.

Assembly of MADPET4 As a consequence of the aforementioned properties, the insert only consists of the 3D-printed structure, crystals and PCBs with SiPMs while the PET DAQ is outside of the MRI bore. Figure 6.2 shows the basic module, figure 6.4 the crystal assembly of MADPET4. The inner 8 parts hold the crystals in place and act as optical separators between the crystals. The density of the whole structure is $\rho = 0.9 - 0.95$ g/cm^3 which reduces the interaction probability compared to e.g. PTFE (Polytetrafluoroethylene) with a density of $\rho = 2.2$ g/cm^3. All crystals are optically insulated from each other and coupled with optical grease to the SiPMs. Figures 6.5 and 6.6 show the composition of the complete system and the assembly without the cables. The outer diameter is 149.7 mm, inner ø 88.0 mm and the length 263.3 mm.

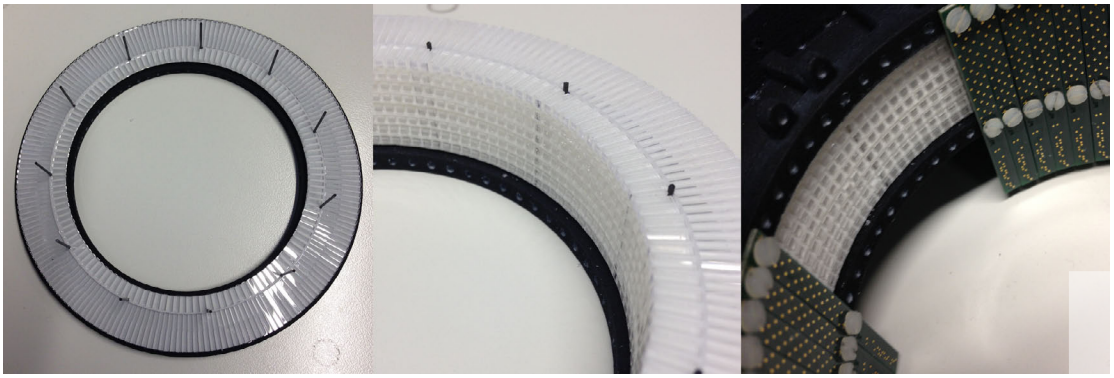

Figure 6.4.: *Left:* Single ring element with 330 crystals in the 3D printed structure (*white*). *Center:* Assembly of the 8 rings with all 2640 crystals. *Right:* PCBs (*green*) mounted to the structure (*black*).

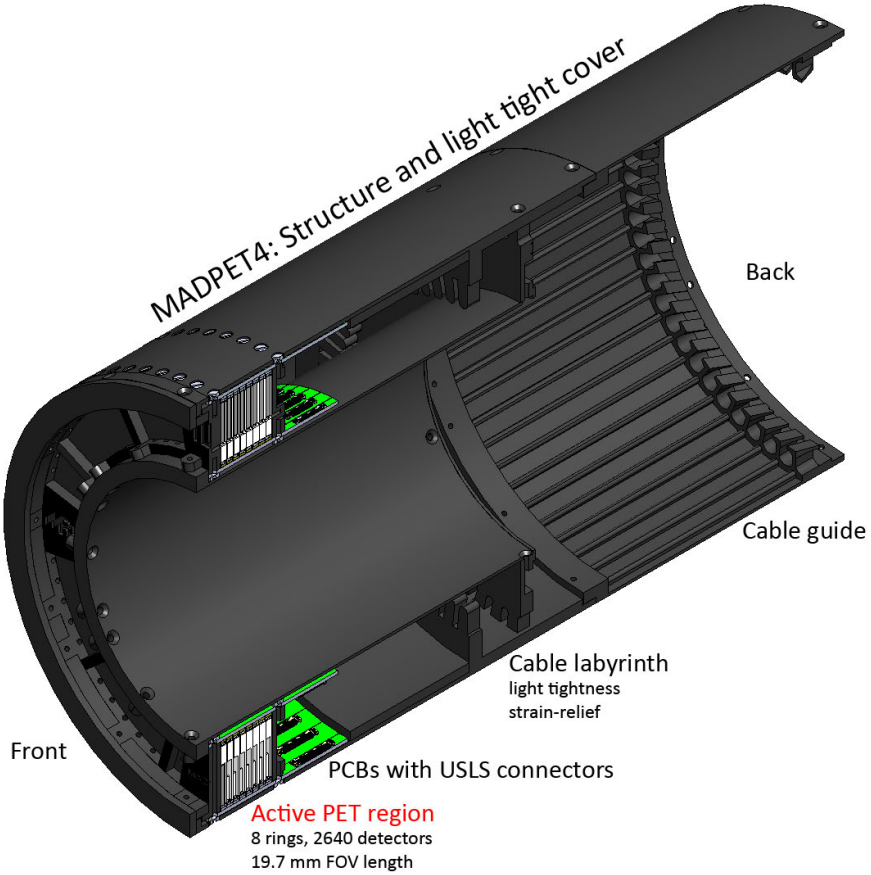

Figure 6.5.: 3D model of MADPET4 with a cut through the sagittal slice. Outer ø 149.7 mm, inner ø 88.0 mm, length 263.3 mm.

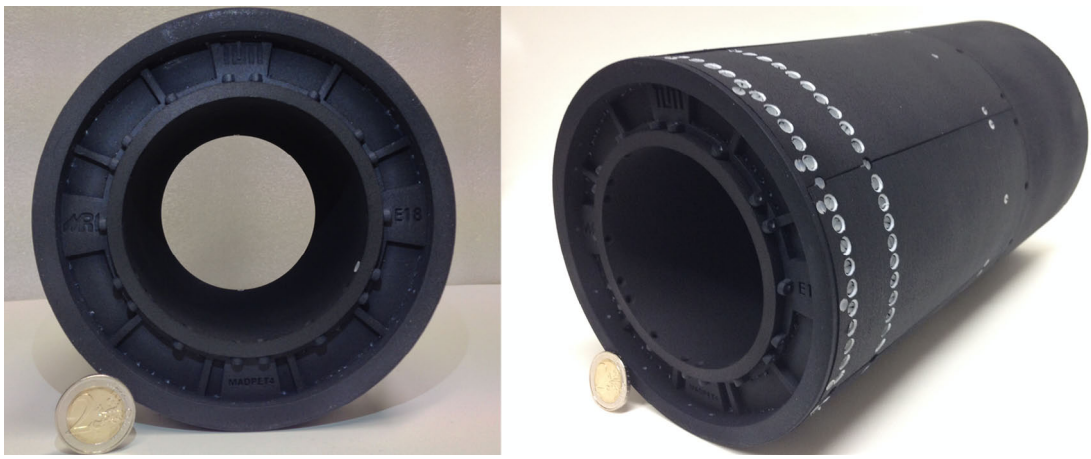

Figure 6.6.: Assembly of MADPET4 with all parts except the USLS cables.

6.1.3. Data Acquisition

For digitization of the signals, SADCs (10 bit, 80 MHz) are used at this stage. Due to the limited number of readout channels available, only two opposing PET modules (each 40 ch) can be read out. The rise time of the SiPM + LYSO signals is with a few ns too fast for this sampling rate and therefore the signals have to be shaped, which degrades the system time resolution. Further description of the SADC can be found in sec. 1.4.1, p. 19.
Currently, a dedicated readout platform based on TOT ASICs and FPGAs is developed, reading all 2640 channels, exploiting the SiPM + LYSO time resolution and digitizing the signals directly after the USLS cables. The principle of the ASIC is described in sec. 1.4.2, p. 20.
The intrinsic performance of the SiPM + LYSO combination has been evaluated with an oscilloscope (LeCroy Waverunner 610Zi).

6.1.4. Image Reconstruction

In general for all reconstructed PET images, the coincidence window was set to 20 ns and the lower energy cut was set to 450 keV.

MADPET4 Outside the MRI An iterative MLEM (Maximum Likelihood Expectation Maximization) reconstruction was used with an analytically computed SM (System Matrix) based on the DRF (Detector Response Function) model [KPS+10]. With 2 facing modules, the covered FOV size is $5.05 \times 5.05 \times 19.7$ mm^3 corresponding to a system matrix with $12 \times 12 \times 54$ voxels with a size of $0.375 \times 0.375 \times 0.375$ mm^3.

Simultaneous PET/MRI On the PET side, One iteration of an OSEM (Ordered Subset Expectation Maximization) reconstruction (8 subsets) using a Monte Carlo

generated SM was performed on CPU (Central Processing Unit) [CR12]. The symmetries of MADPET4 are exploited in the SM. Again with 2 facing modules, the covered FOV size is $5.05 \times 5.05 \times 19.7$ mm^3. Since this SM will be used also for the final MADPET4, it was already calculated for the whole FOV with $262 \times 262 \times 56$ voxels with a size of $(0.375 \text{ mm})^3$.
The MRI images were acquired using 3 different sequences:

- 3D FGRE (Fast Gradient Echo) sequence (256×256 px, 0.7 mm slice thickness, TR 15.8 ms, TE 5.5 ms, scan time 253 s)
- SSFSE (Single Shot Fast Spin Echo) sequence (128×128 px, 2.0 mm slice thickness, TR 2500.0 ms, TE 31.5 ms)
- SEEPI (Spin Echo Echo Planar Imaging) sequence (256×256 px, 1.0 mm slice thickness, TR 2500.0 ms, TE 326.4 ms)

6.1.5. MADPET4 Setup

^{22}Na Point Sources Due to the limited available FOV, all PET measurements were performed with two ^{22}Na point sources (Eckert & Ziegler, MMS04, $3 \times 3 \times 8$ mm^3, active cylinder Ø = 1.0 mm, H = 0.5 mm) One had an activity of 2.8 MBq and the other one 0.6 MBq. An exact placement in the FOV was done with source holders which have been 3D printed from the same material as used for the structure of MADPET4. The holders have 8 slots so that the sources can be placed directly in the center of each ring in transaxial direction.

6.1.5.1. Outside the MRI

To emulate the complete system with the two opposing modules, the point sources are placed on a rotating table in the center of the FOV to cover the missing projections (cf. fig. 6.7). A rotation by 5.45° emulates the complete system with in total 66 modules. Two point like ^{22}Na sources can be positioned by a holder in the center of the FOV. The bias voltage of the SiPMs was set to 34 V in this setup.

6.1.5.2. Simultaneous PET/MRI

For simultaneous PET/MRI scans, the completely assembled MADPET4 was inserted with its center of the FOV matching the RF isocenter of the coil (cf. 6.8). The two opposing modules were connected with 1.50 m USLS cables matched by an adapter to 5 m flat cables, routing the signals outside of the MRI cabin. There the SADC, the common bias supply of 32 V for all SiPMs and the data acquisition laptop are located. In contrast to the measurements outside of the MRI, the phantoms could not be rotated.

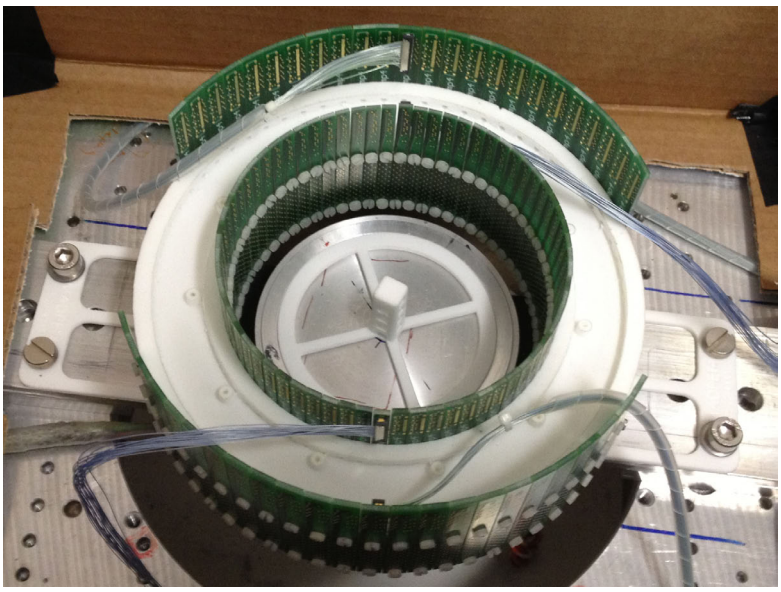

Figure 6.7.: MADPET4 set up as sector tomograph with rotating table in the FOV. Only the two connected modules are active. Point sources can be positioned with help of the holder in the center.

MRI Cubic Grid Phantom To assess the influence on the MR image *with* and *without* the insert, a phantom with a cubic grid (pitch 5 mm, rod thickness 0.7 mm, length 100 mm, ø 48 mm) has been 3D printed (PA-2200) and filled with Gd(aq.) (0.5 μmol/ml) (cf. fig. 6.9).

Simultaneous PET/MRI Phantom Four syringes (5 ml, inner ø 12.5 mm)filled with Gd(aq.) (0.5 μmol/ml) were attached to a structure, which holds two ^{22}Na point sources (center-to-center distance 5.2 mm) in the center of the FOV (cf. fig. 6.10). PET data was acquired at the same time while running the MRI FGRE sequence.

6.2. Results

6.2.1. Energy and Time Resolution

Measurements with Oscilloscope and TOT ASIC Measurements with the LeCroy Waverunner 610Zi (50 Ω, no preamplification) and two PM1150NT + LYSO assembled in MADPET4 showed 8.7% energy resolution and a CTR of 472 ps for the inner detectors, respectively 10.4% and 861 ps for the outer detectors (all values FWHM, $\Delta E/E$ not corrected for saturation). Figure 6.11 shows acquired ^{22}Na energy spectra w/ and w/o flash sequence. A flash sequence was chosen, since it is supposed to induce the most noise to the signals compared to other sequences. It can be seen that for the direct measurement with the oscil-

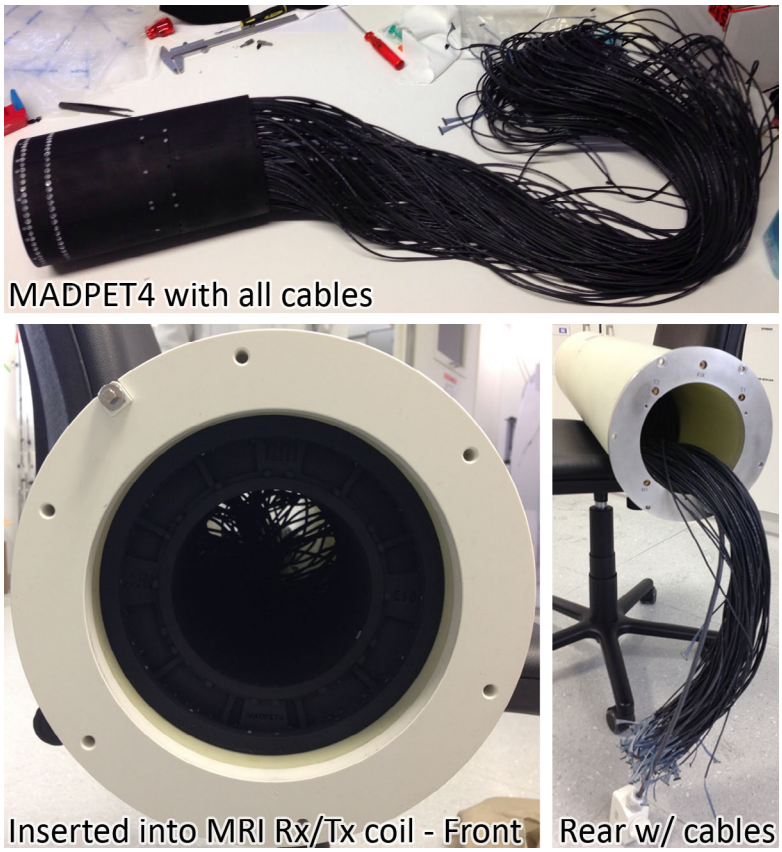

Figure 6.8.: *Top:* Final assembly of MADPET4 with all cables as tested inside the MRI.
Left: MADPET4 inside the MRI Rx/Tx coil with the PET FOV matched to the coil's RF center.
Right: Rear view of the Rx/Tx coil.

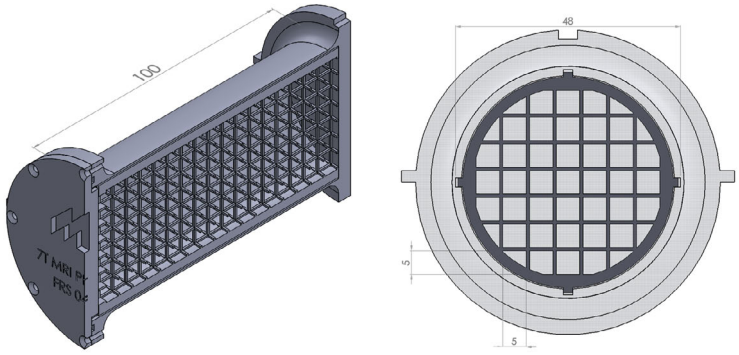

Figure 6.9.: Cubic grid phantom to assess the MRI image quality.
Left: Sagittal cut through the phantom to illustrate the inner structure.
Right: Front (transversal) cut of the phantom with dimensions.

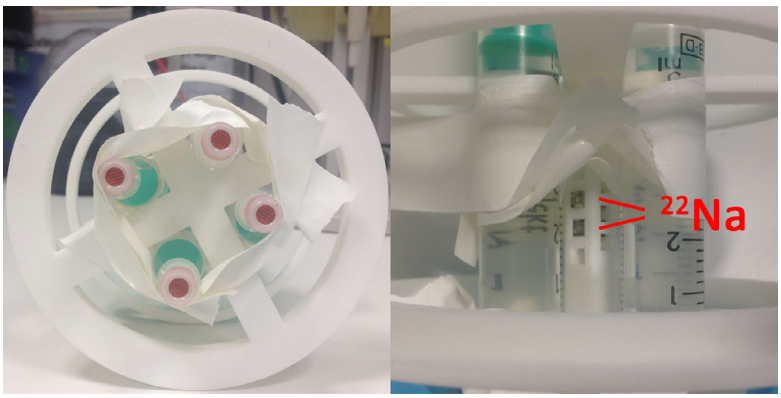

Figure 6.10.: Phantom used for simultaneous PET/MRI measurements. Four syringes filled with Gd(aq.) and two ^{22}Na point sources (distance 5.2 mm).
Left: Front (transversal) view of the phantom.
Right: Top (coronal) view with the point sources.

loscope the running sequence causes a degradation in signal quality and energy resolution. When measuring with the TOT ASIC, no significant impact can bee seen to the ASIC output nor the energy spectrum. With the TOT ASIC, a CTR of 545 ps and $\Delta E/E$ FWHM of 13.4% (not corrected for non-linearity) with a prototype test board and two inner detectors in coincidence could be achieved.

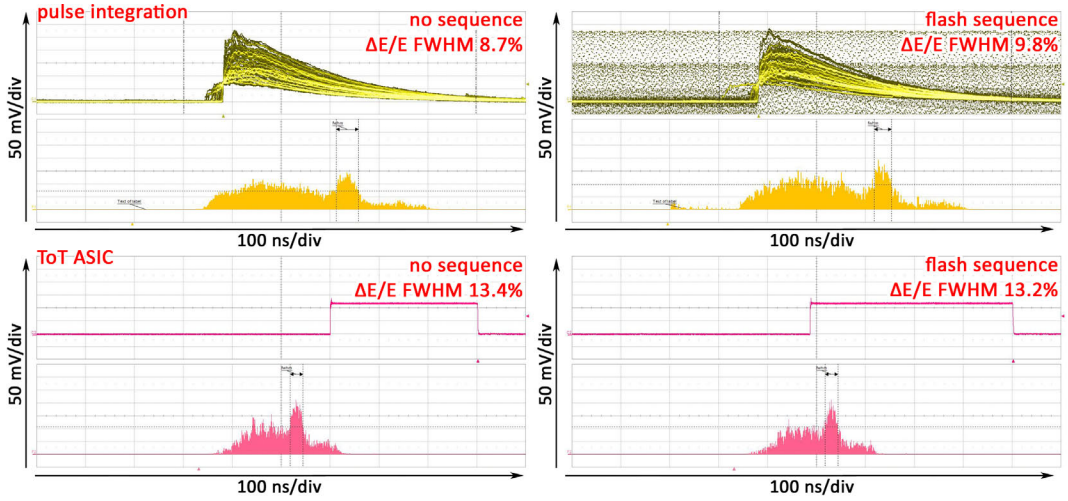

Figure 6.11.: Comparison of ^{22}Na energy spectra w/ and w/o running flash sequence. Results shown for an inner detector (PM1150NT + LYSO 1.5×1.5×6 mm^3)
Top row: Detector signal and a histogram of the pulse area.
Bottom row: TOT ASIC output and histogram of its width.

Measurements with SADC When measuring with the SADC and MADPET4 inside the MRI, there is no difference in the ^{22}Na spectra w/ and w/o running FGRE sequence (240 s meas. time). They show the same photopeak positions

and number of entries (cf. fig. 6.12). Due to the shaping caused by the 6 m long cables and the 80 MHz sampling rate, the global CTR (40 ch vs. 40 ch) degrades to 9.6 ns.

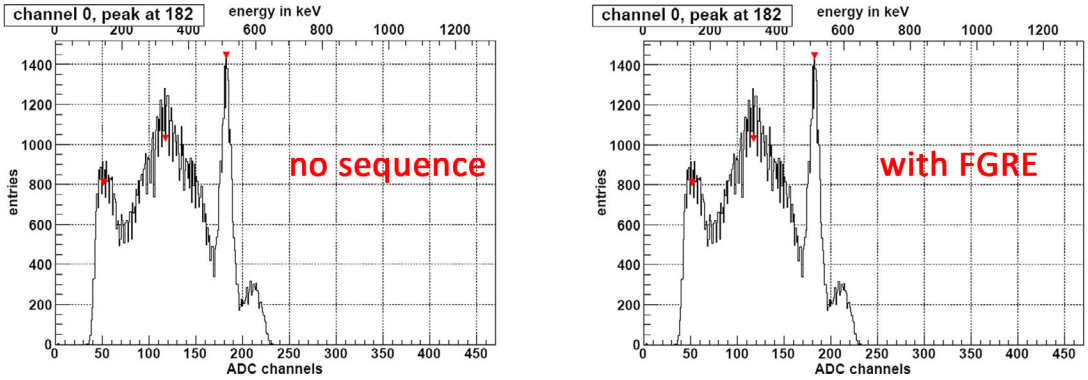

Figure 6.12.: Comparison of the ^{22}Na energy spectra acquired with the SADC for one of the inner detectors (PM1150NT + LYSO 1.5×1.5×6 mm^3).

6.2.2. Image Reconstruction

6.2.2.1. MADPET4 outside the MRI Scanner

Rotated Point Sources The two ^{22}Na point sources could be successfully acquired and the result with 10 iterations MLEM DRF is shown in fig. 6.13. For each of the 33 angular positions the measurement time was 30 s. The sources show different intensities in the image which is expected due to their different activities, although the DRF model is not quantitative. The FWHM of the sources have been extracted along the axis. For source *1* (top source) these are $\mathrm{FWHM}_x = 0.52$ mm, $\mathrm{FWHM}_y = 0.71$ mm and $\mathrm{FWHM}_z = 0.57$ mm. Source *2* (bottom source) with identical dimensions showed $\mathrm{FWHM}_x = 0.67$ mm, $\mathrm{FWHM}_y = 0.61$ mm and $\mathrm{FWHM}_z = 0.30$ mm.

6.2.2.2. MADPET4 inside the MRI Scanner

Cubic Grid Phantom Figure 6.14 shows the impact on the image quality with and without the insert for a FGRE sequence. A degradation of the SNR (Signal-to-Noise Ratio) can be seen. A distortion in spatial resolution is not visible. The distortion in the parallelism of the grid is caused by the MRI and not by the PET insert. When using a flex array surface coil placed on top of the phantom, the SNR could be significantly improved. The slight gradient in the image is due to the surface coil placement. Also the parallelism of the cubic grid is now correctly depicted.
A SSFSE image (cf. fig. 6.15) shows significant degradation of the image quality with the insert. It can be partly recovered when using the flex array surface coil, but still with lower quality than for the reference without insert.

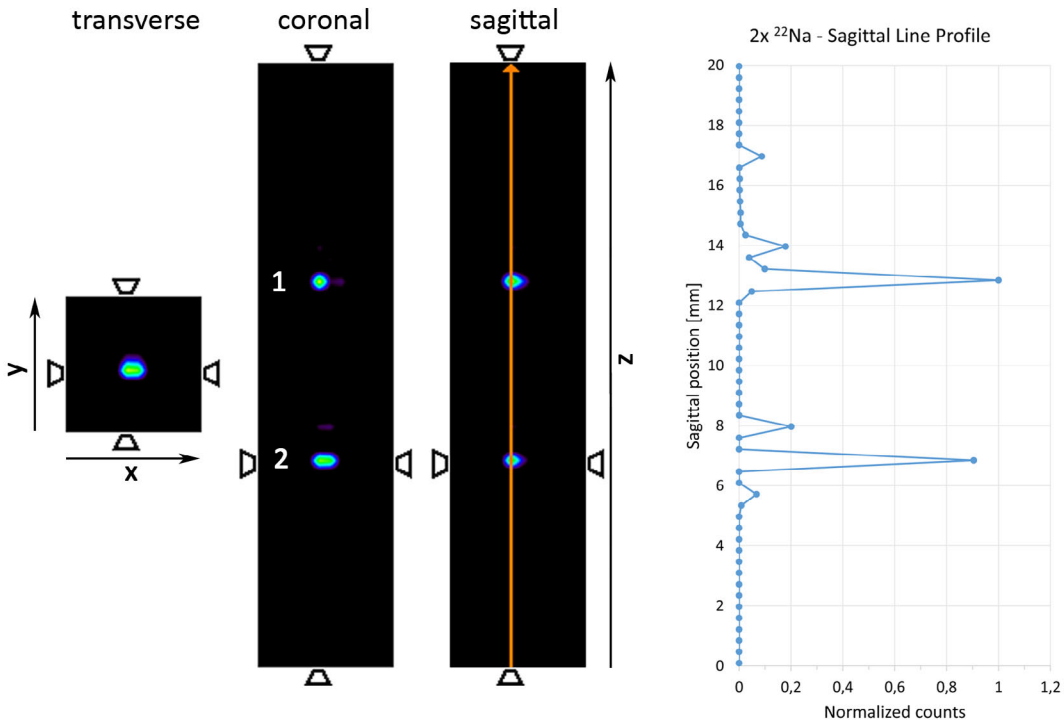

Figure 6.13.: *Left:* Reconstruction of the two rotated ^{22}Na point sources placed in the center of the FOV. MLEM DRF 10 iterations.
Right: Line profile through the indicated slice (*orange*) of the sagittal plane.

The result with an SEEPI sequence is shown in figure 6.16. With the insert in place and without using the flex array surface coil, there is only noise in the image. Using the insert together with the surface coil, the image can be recovered, but shows artifacts.

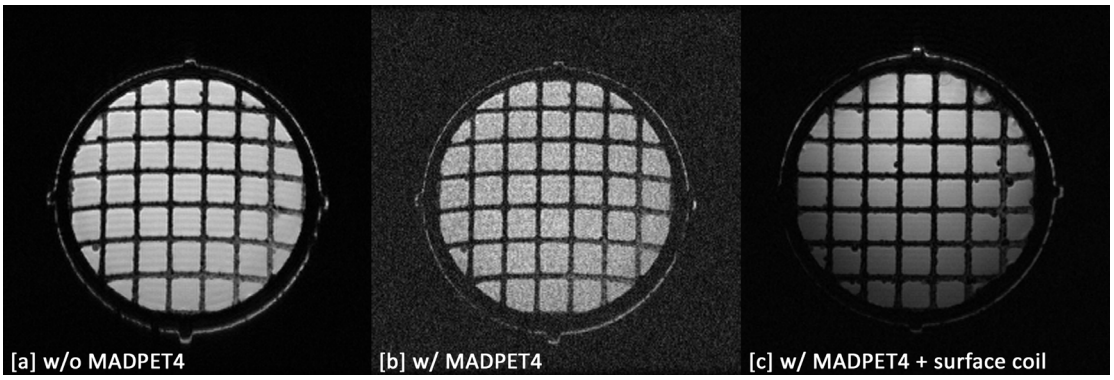

Figure 6.14.: FGRE of the cubic grid phantom.
[a] Without the insert.
[b] With MADPET4 in place, showing the same image slice than *[b]*. A slight degradation in the SNR can be seen.
[c] Image with the insert when using a surface coil on top of the phantom. The SNR is reestablished. Slice is exemplary and not the same than in *[a]* and *[b]*, since the phantom had to be repositioned after placing the surface coil.

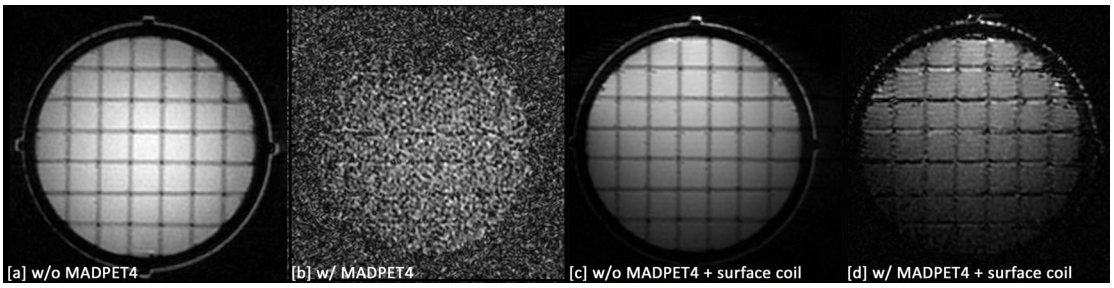

Figure 6.15.: SSFSE of the cubic grid phantom. All images show the same slice.
[a] Without the insert.
[b] With MADPET4 in place. The image quality is degraded.
[c] Removed insert, but with surface coil.
[d] With the insert and surface coil on top of the phantom, the image quality is improved.

Simultaneous PET/MRI Phantom Figure 6.17 shows the fusion of the MRI FGRE image with the simultaneously acquired PET image. Both ^{22}Na point sources are clearly visible and correctly localized. The line profile through the

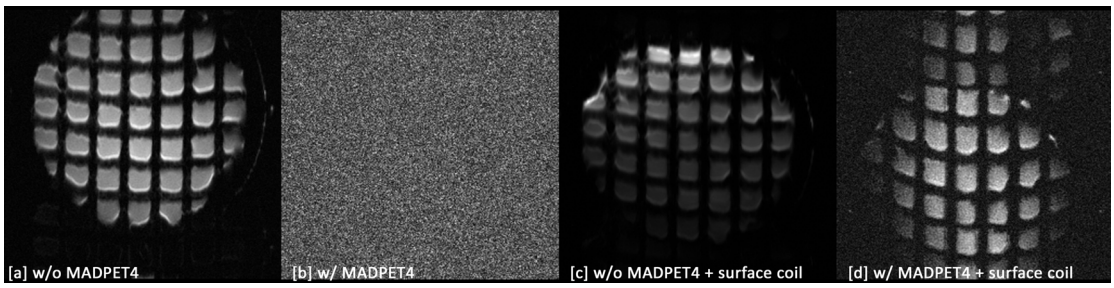

Figure 6.16.: SEEPI of the cubic grid phantom. All images show the same slice.
[a] Without the insert.
[b] With MADPET4 in place, there is no useful MRI signal.
[c] Removed insert, but with surface coil.
[d] With the insert and surface coil on top of the phantom. MRI signal is reestablished.

coronal slice (cf. fig. 6.18) depicts the different source activities and the peak distance of 5.25 mm matches the real distance (5.2 mm).

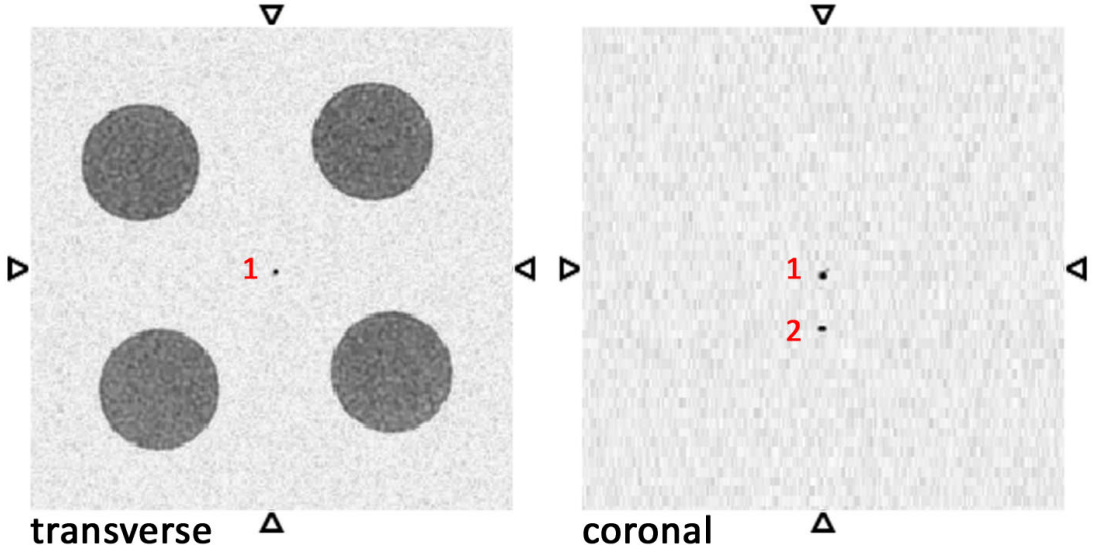

Figure 6.17.: Fusion of the simultaneously acquired PET and MRI images. The two ^{22}Na point sources are clearly visible and correctly localized in the center of the FOV. Sources are numbered in *red*.

6.3. Discussion

The energy and timing performance of the detectors is in the expected range (cf. sec. 4.4.8.3, p. 62). The CTR degradation with the SADC is acceptable for the first tests and will be overcome by the TOT ASIC which is designed not to limit the intrinsic detector CTR. The results with the TOT ASIC while an MRI

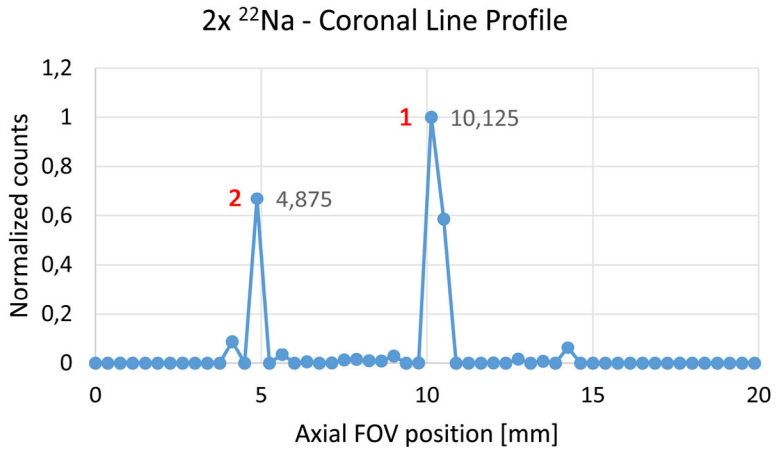

Figure 6.18.: Line profile through the coronal view as shown in fig. 6.17. The numbers right of the peaks are their axial FOV position. Sources are numbered in *red* for correlation with fig. 6.17.

sequence was running, clearly show its usability for simultaneous PET data acquisition. Both the SADC and the TOT ASIC output were not affected by the MRI.
The reconstructions of the ^{22}Na point sources indicate that MADPET4 is capable to reach the expected sub-millimeter spatial resolution in the center of the FOV (cf. sec. 5.3.2.1, p. 70). The variation amongst the extracted FWHM can be explained by the limited number of available data points for the Gauss fit due to the voxel size of 0.375 mm^3 (cf. line profile in fig. 6.13).
Regarding the MRI images with the cubic grid phantom, the FGRE is usable together with MADPET4, even without additional surface coil. Together with the insert, a degradation of SNR is visible but not a spatial distortion. The best FGRE image quality could be achieved when using a surface coil. Consequently, the first simultaneous PET/MR images were taken with a FGRE sequence and without using a surface coil, since the image quality was sufficient. From the SS-FSE and SEEPI images one can conclude, that the MRI signal can be at least partly recovered when using a surface coil. The problem is not the transmission of the RF through MADPET4, as one can see from the images using a surface coil. It seems that the signal from the phantom is blocked by the insert on the way to the outer Tx/Rx coil. Tuning of the MRI measurement parameters may increase the image quality which has to be studied further in more detail.
The degraded image quality with MADPET4 could be caused by the cables, which have a small magnetic shield at the connector. Also for these tests, the cable shielding was connected to ground, which can potentially have an effect as well. The ground can be disconnected outside the MRI for further investigation. The PCB itself has no ground layer. Concerning the guiding of the cables out of the MRI bore, it has to be investigated, whether it is advantageous to guide the cables close to the coil or to consolidate them in the center with maximum distance to

the coil's birdcage.
The PET/MRI studies showed promising results and real simultaneous imaging with both modalities was possible. Unfortunately at the moment with only two modules facing each other, the PET FOV has very small width of 5.05 mm and studies with more complex PET phantoms are not reasonable at the moment. As soon as the first board of the new TOT ASIC platform is working, 6 complete modules can be read out, which increases the FOV width to 16.0 mm. Then together with a rotation of the phantom, more advanced PET studies are possible. In comparison to other PET/MRI systems, currently MADPET4 is the only reported system working with the SiPM technology at 7 T and using one-to-one coupling of photodetector and crystal. All other systems reported use light sharing methods (block detectors). SiPMs have been used up to a maximum field strength of 3 T [HCJ+10, YWW+11, KCH+11, HKK+12, YKK+12, WWD+13]. Other systems use APDs and are either working at at 7 T [GZC+06, KWH+12] or at 9.4 T [MSJ+11, SOPA+13]. Advantages of block detectors are their reduced number of detector channels and the potential to cover a larger FOV.

6.4. Conclusion and Outlook

MADPET4 is the first preclinical PET insert for simultaneous PET/MRI which is based on SiPMs and working in a 7 T MRI scanner. It shows promising results already with two active modules in the simultaneous tests inside the MRI. Especially encouraging is the simultaneous acquisition of both modalities without any RF shielding of the PET and the reasonable image quality of the MRI FGRE even without using a surface coil. A coil for mouse and rat studies is currently under development, which will fit inside MADPET4, making it a versatile instrument for preclinical research. In contrast to the traditional approach with block-wise arranged scintillators in the PET ring, the concept strictly focuses on high spatial resolution and high rate capability due to the individual crystal readout, uniform sensitivity by minimizing gaps in the crystal arrangement and depth of interaction due to the two crystal layers. A readout platform based on TOT ASICs to handle all channels without limiting the detector performance is currently under development. The OSEM reconstruction is already implemented on GPUs (Graphics Processing Unit) with a speedup of a factor 6 compared to CPU (Central Processing Unit).

6.5. Acknowledgments

The research leading to these results has received funding from the European Union Seventh Framework Program (FP7) under Grant Agreement No. 294582 ERC Grant MUMI. Thanks to Geoffrey Topping and Franz Schilling for their MRI measurements and valuable feedback.

7. Summary and Outlook

Within this thesis in total three different PET prototype scanners have been developed and set into operation. With each scanner, images could be successfully reconstructed.

Focusing on the latest available technology, state of the art **SiPMs** were of particular interest in combination with the newly developed **GAGG** scintillator and **LYSO** as the current gold standard. The fundamentals of these new technologies have been evaluated and successfully translated to the use in PET. Different aspects and research topics like e.g. spatial resolution or energy and timing performance have been covered with the first two PET scanners, which prepared the ground for the development of the MRI compatible MADPET4 insert. All three of them have a direct **one-to-one coupling of scintillator to the photodetector** in common, which is up to date still a unique feature in preclinical PET. All other reported systems employ light sharing methods with a mismatch of scintillator size compared to the larger photodetectors [DBK+14]. Only the latest clinical Philips *Vereos Digital PET/CT* introduced in 2014 uses this concept [Kon14]. The advantages compared to block detectors are the higher count rate capability, direct interaction localization, reduced pile-up effects and identification of inter-crystal scattered events which can increase the total system efficiency. In addition the lower limit of the spatial resolution is defined by the size of the single scintillator elements. This comes at the cost of a higher number of detector channels compared to light sharing methods.

The first system developed was **MADPET3**, with the main focus on the feasibility to use SiPMs for PET and to achieve sub millimeter spatial resolution. Both goals could be successfully achieved and verified using a custom-made phantom printed with ^{18}F radioactive ink, resulting in a spatial resolution of 0.8 mm. One of the main conclusions for the future developments was, that the SiPMs should not be assembled in an array with a common epoxy layer, since this introduces undesired optical crosstalk. As an implication, MADPET4 uses single separated photodetectors dedicated to a single crystal.

With the PET prototype based on **digital SiPMs**, this new detector technology was successfully used in combination with GAGG. The DPC platform with the possibility to set exact detector parameters minimizes the detector influence due to the robustness and reproducibility of the settings under different conditions and with different scintillators. This was especially convenient for the comparison

between GAGG with LYSO. Due to the very good intrinsic time resolution of the DPCs when triggering on the first photon, the CTR lower limit is determined by the scintillator and not the photodetector. Very good CTR of 310 ps with GAGG and 171 ps with LYSO could be achieved. Regarding the energy resolution, saturation effects are significant which is common for all SiPMs coupled to bright scintillators. With GAGG 8.5% FWHM and with LYSO 12.6% FWHM could be achieved. Judging by these results, GAGG would also have been a candidate for the use in MADPET4, but unfortunately it is not MRI compatible due to its Gd component.

Since the digital SiPM technology is not usable for a project like MADPET4 because of space constraints, design limitations and MRI compatibility, also intensive studies with **analog SiPMs** have been performed. Particularly the SiPMs from KETEK have been investigated in the 3×3 mm^2 version (PM33) and also in 1.2×1.2 mm^2 (PM11), a size which is only available from KETEK and matches the proposed crystal end face of MADPET4. The KETEK SiPMs showed the best overall performance with regard to the specific application. Highlights are their lowest temperature dependency (15 mV/K, $< 0.5\%$ change of the gain per K) of the SiPMs available at that time in combination with a very high gain ($> 8 \cdot 10^6$), high PDE $> 50\%$ and the small package size of PM11 ($2.45 \times 1.95 \times 1.8$ mm^3). These features were a key to design MADPET4 with its crystal arrangement and without active electronic components at the front end. Since the signal amplitude with LYSO is already ~ 100 mV at 50 Ω, no direct preamplification is needed.

After evaluation of the potential detector, which defines the space constraint for the arrangement of the crystals, design considerations and **simulation studies for MADPET4** to optimize its crystal arrangement have been conducted. Key features are the dual layer concept for DOI information, a highly symmetric arrangement with minimal gaps and a total length sum of 20 mm for inner and outer crystal layer. As a compromise between spatial resolution, number of readout channels and size of the SiPM, a crystal end face of 1.5×1.5 mm^2 has been chosen. A novelty is also, that each crystal is transaxially facing the center of the FOV which has positive effects on the sensitivity uniformity. A symmetric and uniform sensitivity is advantageous for the reconstruction and reduces the size of the generated system matrix [CR12]. With the configuration of 6 mm long crystals for the inner and 14 mm for the outer layer, a spatial resolution < 2.3 mm up to 80% (ø 79 mm) of the FOV and < 1 mm in the center of the FOV was achieved in the simulation.

The realization of **MADPET4 as an MRI compatible insert** with 2640 SiPMs and LYSO crystals started after the promising results from the simulation studies. One of the main tasks involved the development of the whole structure with MRI compatible materials. A cost effective way which provided the required freedom in design was found with a 3D printed (laser-sintered) polyamide, which

is MRI transparent. Of high importance was also the choice for an appropriate cable to connect this high number of channels without degrading the signal quality. The USLS micro coaxial cable with 0.4 mm pitch is an ideal match due to its small size, availability and signal transmission properties. After choosing the individual components for the front end, the PCBs could be developed. They not only have to serve as the electrical connection for the SiPMs and connectors, but also to minimize the amount of material, since they are used as a supporting element to hold the crystals together.
The prototype version of MADPET4 with two active modules first has been evaluated outside the MRI yielding the first PET images. Then the basic functionality was tested inside the MRI with no negative influence to the PET signal quality. The TOT ASIC, on which the future DAQ is based, has been successfully evaluated and is proven to work simultaneously while an MRI sequence is running. After this proof of concept, the insert front end has been finalized with the complete structure, all detectors and all cables. Studies of the MRI image quality showed a slight SNR degradation with the insert for FGRE, which can be recovered when using a surface coil. MADPET4 in its final configuration is capable of simultaneous PET/MRI imaging with acquisition of both modalities at the same time, proofing the functionality of the concept.
The DAQ platform based on the TOT ASIC to read out all 2640 channels is currently under development. It is the next step towards the full integration and first preclinical studies with mice of MADPET4 together with the 7 T MRI. The whole data processing chain for MADPET4 has been developed during this thesis. It can handle input data both from simulations or measurements and attaches seamlessly either to the OSEM reconstruction based on a Monte Carlo generated system matrix or the MLEM reconstruction with an analytically computed DRF system matrix.

The insert can also be used as **a test bench for novel PET detectors**. In the PET community, the use of continuous crystals read out by multiple photodetectors is currently revisited. This approach can potentially provide more exact DOI information at the cost of limiting the count rate. This has been taken into account for the design of MADPET4, where the current 40 single scintillators per module can be easily exchanged with a continuous crystal (cf. fig. 6.1). MADPET4 can be used in the future to study this technology, since the DAQ system or other components of the insert do not need to be changed.

MADPET4 has some **unique features**. It is currently the only MRI compatible PET insert using one-to-one coupled scintillators, which is using the SiPM technology at 7 T. It is working without any RF shielding and the whole structure is made from 3D-printed parts. MADPET4 is capable to work inside the Rx/Tx coil as the innermost part of the combined PET/MRI system. This is possible due to its unique design and makes the insert a versatile tool for preclinical PET/MRI.

A. Appendix

A.1. Publications, Conference Contributions, Teaching

Publications

2015 Schneider, F. R., Hohberg, M., Mann, A. B., Paul, S., Ziegler, S. I.
A Submillimeter Resolution PET Prototype Evaluated With an ^{18}F Inkjet Printed Phantom
IEEE TNS, vol.62, no.5, pp.2043-2047. doi: 10.1109/TNS.2015.2461517

2015 Schneider F. R., Shimazoe K., Somlai-Schweiger I., Ziegler S. I.
A PET detector prototype based on digital SiPMs and GAGG scintillators
Phys Med Biol. 2015 Feb 21;60(4):1667-79. doi: 10.1088/0031-9155/60/4/1667

2015 Somlai-Schweiger I., Schneider F. R., Ziegler S. I.
Performance Analysis of Digital Silicon Photomultipliers for PET
Journal of Instrumentation, 10, P05005P05005. doi:10.1088/1748-0221/10/05/P05005

2014 Schneider F. R., Ganka T. R., eker G., Engelmann E., Renker D., Paul S., Hansch W., Ziegler S. I.
Characterization of blue sensitive 3 x 3 mm^2 SiPMs and their use in PET
Journal of Instrumentation, 9(07), P07027P07027. doi:10.1088/1748-0221/9/07/P07027

2012 Pulko, J., Schneider F. R., Velroyen A., Renker D., Ziegler S. I.
A Monte-Carlo model of a SiPM coupled to a scintillating crystal
Journal of Instrumentation, 7, P02009. doi:10.1088/1748-0221/7/02/P02009

2011 Schneider F. R., Mann A. B., Konorov I., Delso G.
A Positron Emission Tomograph Based on LSO-APD Modules with a Sampling ADC Read-out System for a Students Advanced Laboratory Course
Zeitschrift für Medizinische Physik. doi:10.1016/j.zemedi.2011.09.004

Conference Contributions

2015 IEEE NSS/MIC/RTSD, San Diego, USA
Vortrag: MADPET4 - A 3D printed, unshielded, MRI compatible Dual Layer PET

Insert: First simultaneous PET/ MRI Results
Gefördert durch einen IEEE Trainee Grant

2015 ESMI, Tübingen, Deutschland
Vortrag: MADPET4 - A 3D-printed MRI compatible Dual Layer PET Insert - First Tests with Two Modules

2014 IEEE NSS/MIC/RTSD, Seattle, USA
Poster: MADPET4 - An MRI compatible Dual Layer PET Insert: First Tests with Two Modules
Gefördert durch einen IEEE Trainee Grant

2014 Nuklearmedizin, Hannover, Deutschland
Vortrag: A PET prototype based on digital SiPMs and GAGG scintillators

2013 NIRS-TUM Workshop on PET Physics, Tokyo, Japan
Vortrag: MADPET4 - Design of an MRI compatible PET insert

2013 IEEE NSS/MIC/RTSD, Seoul, Südkorea
Poster: Simulation Studies of MADPET4 - A Design Concept for an MRI compatible PET Insert with Individually Read Out Crystals
Gefördert durch einen IEEE Trainee Grant und das DAAD Kongressreisenprogramm

2013 SNMMI, Vancouver, Kanada
Vortrag: A PET prototype based on digital SiPMs and GAGG scintillators

2012 IEEE NSS/MIC/RTSD, Anaheim, USA
Vortrag: Characterization of a Recently Developed SiPM for PET Applications

2012 IEEE NSS/MIC/RTSD, Anaheim, USA
Poster: A Sub-Millimeter-Resolution PET Scanner Prototype Based on Single LYSO Crystal Readout with SiPMs and MLEM Reconstruction

2012 PhotoDET, Paris-Orsay, Frankreich
Poster: Characterization of Recently Developed SiPMs for PET

2011 Nuklearmedizin, Bregenz, Österreich
Vortrag: Erste Leistungsstudien eines Prototypen PET Scanners für kombiniertes PET/MR basierend auf G-APDs

2010 IEEE NSS/MIC/RTSD, Knoxville, USA
Poster: First Performance Studies of a Prototype SiPM PET Scanner

2010 DGMP, Freiburg, Deutschland
Poster: Positronen-Emissions-Tomographie als studentischer Praktikumsversuch

2010 DPG, Regensburg, Deutschland
Vortrag: Ein 2D Positronen-Emissions-Tomograph für die studentische Ausbildung

Teaching and Supervision

2010 - 2015 Betreuung des studentischen Fortgeschrittenenpraktikums
Klinikum rechts der Isar, Nuklearmedizinische Klinik und Poliklinik
Thema: Positronen-Emissions-Tomographie

2013 Betreuung der Bachelorarbeit von R. Sharma
Physik Department E18, TU München
Thema: Charakterisierung von Silizium Photomultipliern zur Verwendung in der Kleintier-Positronen-Emissions-Tomographie

2012 Betreuung der Bachelorarbeit von A. Kristen
Lehrstuhl für Medizintechnik, TU München
Thema: Evaluierung unterschiedlicher Methoden zur Herstellung radioaktiver Phantome zum Test von hochauflösenden Positronen-Emissions-Tomographen

Bibliography

[ABB+05] V. Andreev, V. Balagura, B. Bobchenko, P. Buzhan, J. Cvach, M. Danilov, E. Devitsin, V. Dodonov, B. Dolgoshein, G. Eigen, L. Filatov, E. Garutti, M. Groll, R. D. Heuer, A. Ilyin, M. Janata, I. Kacl, V. Kantserov, V. Kaplin, A. Karakash, S. Klemin, V. Korbel, V. Kozlov, H. Meyer, R. Mizuk, V. Morgunov, E. Novikov, S. Němeček, R. Pöschl, I. Polák, E. Popova, A. Raspereza, S. Reiche, V. Rusinov, F. Sefkow, P. Smirnov, S. Smirnov, Yu Soloviev, E. Tarkovsky, A. Terkulov, V. Tikhomirov, Š Valkár, J. Weichert, and J. Zálešák. A high-granularity scintillator calorimeter readout with silicon photomultipliers. *Nuclear Instruments and Methods in Physics Research, Section A: Accelerators, Spectrometers, Detectors and Associated Equipment*, 540:368–380, 2005.

[ADA+08] C. Amsler, M. Doser, M. Antonelli, D. M. Asner, K. S. Babu, H. Baer, H. R. Band, R. M. Barnett, E. Bergren, J. Beringer, G. Bernardi, W. Bertl, H. Bichsel, O. Biebel, P. Bloch, E. Blucher, S. Blusk, R. N. Cahn, M. Carena, C. Caso, A. Ceccucci, D. Chakraborty, M. C. Chen, R. S. Chivukula, G. Cowan, O. Dahl, G. D'Ambrosio, T. Damour, A. de Gouvêa, T. DeGrand, B. Dobrescu, M. Drees, D. A. Edwards, S. Eidelman, V. D. Elvira, J. Erler, V. V. Ezhela, J. L. Feng, W. Fetscher, B. D. Fields, B. Foster, T. K. Gaisser, L. Garren, H. J. Gerber, G. Gerbier, T. Gherghetta, G. F. Giudice, M. Goodman, C. Grab, A. V. Gritsan, J. F. Grivaz, D. E. Groom, M. Grünewald, A. Gurtu, T. Gutsche, H. E. Haber, K. Hagiwara, C. Hagmann, K. G. Hayes, J. J. Hernández-Rey, K. Hikasa, I. Hinchliffe, A. Höcker, J. Huston, P. Igo-Kemenes, J. D. Jackson, K. F. Johnson, T. Junk, D. Karlen, B. Kayser, D. Kirkby, S. R. Klein, I. G. Knowles, C. Kolda, R. V. Kowalewski, P. Kreitz, B. Krusche, Yu V. Kuyanov, Y. Kwon, O. Lahav, P. Langacker, A. Liddle, Z. Ligeti, C. J. Lin, T. M. Liss, L. Littenberg, J. C. Liu, K. S. Lugovsky, S. B. Lugovsky, H. Mahlke, M. L. Mangano, T. Mannel, A. V. Manohar, W. J. Marciano, A. D. Martin, A. Masoni, D. Milstead, R. Miquel, K. Mönig, H. Murayama, K. Nakamura, M. Narain, P. Nason, S. Navas, P. Nevski, Y. Nir, K. A. Olive, L. Pape, C. Patrignani, J. A. Peacock, A. Piepke, G. Punzi, A. Quadt, S. Raby, G. Raffelt, B. N. Ratcliff, B. Renk, P. Richardson, S. Roesler, S. Rolli, A. Romaniouk, L. J. Rosenberg, J. L. Rosner, C. T. Sachrajda, Y. Sakai, S. Sarkar, F. Sauli, O. Schneider,

D. Scott, W. G. Seligman, M. H. Shaevitz, T. Sjöstrand, J. G. Smith, G. F. Smoot, S. Spanier, H. Spieler, A. Stahl, T. Stanev, S. L. Stone, T. Sumiyoshi, M. Tanabashi, J. Terning, M. Titov, N. P. Tkachenko, N. A. Törnqvist, D. Tovey, G. H. Trilling, T. G. Trippe, G. Valencia, K. van Bibber, M. G. Vincter, P. Vogel, D. R. Ward, T. Watari, B. R. Webber, G. Weiglein, J. D. Wells, M. Whalley, A. Wheeler, C. G. Wohl, L. Wolfenstein, J. Womersley, C. L. Woody, R. L. Workman, A. Yamamoto, W. M. Yao, O. V. Zenin, J. Zhang, R. Y. Zhu, P. A. Zyla, G. Harper, V. S. Lugovsky, and P. Schaffner. Review of Particle Physics. *Physics Letters, Section B: Nuclear, Elementary Particle and High-Energy Physics*, 667:1–6, 2008.

[aLZBM93] a.L. Lacaita, F. Zappa, S. Bigliardi, and M. Manfredi. On the bremsstrahlung origin of hot-carrier-induced photons in silicon devices. *IEEE Transactions on Electron Devices*, 40(3):577–582, March 1993.

[BGM+13] S E Brunner, L Gruber, J Marton, H. Orth, and K. Suzuki. Time resolution below 100 ps for the SciTil detector of PANDA employing SiPM. *arXiv preprint arXiv: ...*, page 10, December 2013.

[BMR06] I Britvitch, Y Musienko, and D Renker. Investigation of a photon counting avalanche photodiode from Hamamatsu photonics. In *Nuclear Instruments and Methods in Physics Research Section A: Accelerators, Spectrometers, Detectors and Associated Equipment*, volume 567, pages 276–280. Elsevier Science Bv, November 2006.

[BTVM05] Dale L Bailey, David W Townsend, Peter E Valk, and Michael N Maisey. *Positron Emission Tomography*. 2005.

[CD06] S Cherry and M Dahlbom. *PET: Physics, Instrumentation and Scanners*. Springer New York, New York, NY, 2006.

[CDM+07] F Corsi, A Dragone, C Marzocca, A Del Guerra, P Delizia, N Dinu, C Piemonte, M Boscardin, and G F Dalla Betta. Modelling a silicon photomultiplier (SiPM) as a signal source for optimum front-end design. *Nucl. Instrum. Meth. A*, 572(1):416–418, 2007.

[CM09] Cristian C Constantinescu and Jogeshwar Mukherjee. Performance evaluation of an Inveon PET preclinical scanner. *Physics in medicine and biology*, 54:2885–2899, 2009.

[CR12] Jorge Cabello and Magdalena Rafecas. Comparison of basis functions for 3D PET reconstruction using a Monte Carlo system matrix, 2012.

[CSM+09] W Chewpraditkul, L Swiderski, M Moszynski, T Szczesniak, A Syntfeld-Kazuch, C Wanarak, and P Limsuwan. Scintillation properties of LuAG:Ce, YAG:Ce and LYSO:Ce crystals for gamma-ray detection. *IEEE Transactions on Nuclear Science*, 56(6):3800–3805, 2009.

[CSP12] S R Cherry, J A Sorenson, and M E Phelps. *Physics in nuclear medicine*. 2012.

[DBC+10] N Dinu, C Bazin, V Chaumat, C Cheikali, a Para, V Puill, C Sylvia, and J F Vagnucci. Temperature and bias voltage dependence of the MPPC detectors. *IEEE Nuclear Science Symposuim & Medical Imaging Conference*, pages 215–219, October 2010.

[DBK+14] Jonathan a Disselhorst, Ilja Bezrukov, Armin Kolb, Christoph Parl, and Bernd J Pichler. Principles of PET/MR Imaging. *Journal of nuclear medicine : official publication, Society of Nuclear Medicine*, 55(Supplement 2):2S–10S, May 2014.

[DFI13] Sergei Dolinsky, Geng Fu, and Adrian Ivan. Timing Resolution Performance Comparison for Fast and Standard Outputs of SensL SiPM. 2013.

[DFJ+11a] Gaspar Delso, Sebastian Fürst, Björn Jakoby, Ralf Ladebeck, Carl Ganter, Stephan G Nekolla, Markus Schwaiger, and Sibylle I Ziegler. Performance measurements of the Siemens mMR integrated whole-body PET/MR scanner. *Journal of nuclear medicine : official publication, Society of Nuclear Medicine*, 52(12):1914–22, December 2011.

[DFJ+11b] Gaspar Delso, Sebastian Fürst, Björn Jakoby, Ralf Ladebeck, Carl Ganter, Stephan G Nekolla, Markus Schwaiger, and Sibylle I Ziegler. Performance measurements of the Siemens mMR integrated whole-body PET/MR scanner. *Journal of nuclear medicine : official publication, Society of Nuclear Medicine*, 52(12):1914–22, December 2011.

[DKH+14] Gaspar Delso, Mehdi Khalighi, Marlena Hofbauer, Miguel Porto, Patrick Veit-Haibach, and Gustav von Schulthess. Preliminary evaluation of image quality in a new clinical ToF-PET/MR scanner. *EJNMMI Physics*, 1(Suppl 1):A41, 2014.

[DOW13] DOW CORNING. DOW CORNING (R) 1-2577 CONFORMAL COATING. 2013.

[DPF+09] C. Degenhardt, Gordian Prescher, T. Frach, A. Thon, R. de Gruyter, A. Schmitz, and R. Ballizany. The digital Silicon Photomultiplier A novel sensor for the detection of scintillation light. In *2009 IEEE*

Nuclear Science Symposium Conference Record (NSS/MIC), pages 2383–2386. IEEE, October 2009.

[DRT+12] Carsten Degenhardt, Pedro Rodrigues, Andreia Trindade, Ben Zwaans, Oliver Mulhens, Ralf Dorscheid, Andreas Thon, Andre Salomon, and Thomas Frach. Performance evaluation of a prototype Positron Emission Tomography scanner using Digital Photon Counters (DPC). In *2012 IEEE Nuclear Science Symposium and Medical Imaging Conference Record (NSS/MIC)*, pages 2820–2824. IEEE, October 2012.

[DZ09] Gaspar Delso and Sibylle Ziegler. PET/MRI system design. *European Journal of Nuclear Medicine and Molecular Imaging*, 36(0):86–92, 2009.

[DZFdG10] C Degenhardt, B Zwaans, T Frach, and R de Gruyter. Arrays of digital Silicon Photomultipliers Intrinsic performance and application to scintillator readout. In *IEEE Nuclear Science Symposium & Medical Imaging Conference*, pages 1954–1956. IEEE, October 2010.

[EFH+10] S Espana, L M Fraile, J L Herraiz, J M Udias, M Desco, and J J Vaquero. Performance evaluation of SiPM photodetectors for PET imaging in the presence of magnetic fields. *Nuclear Instruments & Methods in Physics Research Section a-Accelerators Spectrometers Detectors and Associated Equipment*, 613(2):308–316, 2010.

[ESCS+10] Patrick Eckert, Hans-Christian Schultz-Coulon, Wei Shen, Rainer Stamen, and Alexander Tadday. Characterisation studies of silicon photomultipliers. *Nuclear Instruments and Methods in Physics Research Section A: Accelerators, Spectrometers, Detectors and Associated Equipment*, 620(2-3):217–226, August 2010.

[Esp08] Irene Torres Espallardo. *Image Reconstruction and Correction Methods for MADPET-II based on Monte Carlo Techniques.* Phd thesis, Universitat de Valencia, 2008.

[ESSCS09] Patrick Eckert, Wei Shen, Hans-Christian Schultz-Coulon, and Rainer Stamen. Characterisation Studies of Silicon Photomultipliers for a Calorimeter for the ILC. *Workshop on New Photon-Detectors (PD09)*, 2009.

[ETF+08] Samuel Espana, Gustavo Tapias, Luis M Fraile, Joaquin L Herraiz, Esther Vicente, Jose Udias, Manuel Desco, and Juan J Vaquero. Performance evaluation of SiPM detectors for PET imaging in the presence of magnetic fields. In *2008 IEEE Nuclear Science Symposium Conference Record*, pages 3591–3595. IEEE, October 2008.

[Eva55] Robley D Evans. *The Atomic Nucleus*. 1955.

[FÖ9] Sebastian Fürst. *Development and Evaluation of Novel Detectors for Combined PET / MR Imaging , Based on SiPMs and Fast Scintillation Crystals*. Diploma thesis, 2009.

[FGS+14a] Alessandro Ferri, Alberto Gola, Nicola Serra, Alessandro Tarolli, Nicola Zorzi, and Claudio Piemonte. Performance of FBK high-density SiPM technology coupled to Ce:LYSO and Ce:GAGG for TOF-PET. *Physics in medicine and biology*, 59(4):869–80, February 2014.

[FGS+14b] Alessandro Ferri, Alberto Gola, Nicola Serra, Alessandro Tarolli, Nicola Zorzi, and Claudio Piemonte. Performance of FBK high-density SiPM technology coupled to Ce:LYSO and Ce:GAGG for TOF-PET. *Physics in medicine and biology*, 59(4):869–80, February 2014.

[Fla08] David Flay. Magnetic Field Effects on 5 PMT, 2008.

[FPD+09] T. Frach, G. Prescher, C. Degenhardt, R. de Gruyter, a. Schmitz, and R. Ballizany. The digital silicon photomultiplier Principle of operation and intrinsic detector performance. *2009 IEEE Nuclear Science Symposium Conference Record (NSS/MIC)*, pages 1959–1965, October 2009.

[FPDZ10] T Frach, G Prescher, C Degenhardt, and B Zwaans. The digital silicon photomultiplier System architecture and performance evaluation. *IEEE Nuclear Science Symposuim & Medical Imaging Conference*, pages 1722–1727, October 2010.

[FPH+12] S Fürst, J Pulko, M Hohberg, a B Mann, and S I Ziegler. Effects of temperature and bias voltage on the properties of a PET detector module based on the individual readout of 1 mm x 1 mm LYSO crystals by monolithic arrays of SiPMs. *Journal of Instrumentation*, 7:P08002–P08002, 2012.

[Fra12] T Frach. Optimization of the digital Silicon Photomultiplier for Cherenkov light detection. *Journal of Instrumentation*, 7(01):C01112–C01112, January 2012.

[GA11] General Electric and Agilent Technologies. Discovery MR901 Preclinical 7T/31 System, 2011.

[GAD+13] S. Gundacker, E. Auffray, N. Di Vara, B. Frisch, H. Hillemanns, P. Jarron, B. Lang, T. Meyer, S. Mosquera-Vazquez, E. Vauthey,

and P. Lecoq. SiPM time resolution: From single photon to saturation. *Nuclear Instruments and Methods in Physics Research Section A: Accelerators, Spectrometers, Detectors and Associated Equipment*, 718:569–572, August 2013.

[GE 14] GE Healthcare. Signa PET/MR, 2014.

[GGCZ03] A.C. Giudice, M Ghioni, S Cova, and F Zappa. A process and deep level evaluation tool: afterpulsing in avalanche junctions. In *ESSDERC '03. 33rd Conference on European Solid-State Device Research, 2003.*, pages 347–350. IEEE, 2003.

[Gol99] V Golovin. Avalanche Photodetector, 1999.

[GZC+06] Ronald Grazioso, Nan Zhang, James Corbeil, Matthias Schmand, Ralf Ladebeck, Markus Vester, Günter Schnur, Wolfgang Renz, and Hubertus Fischer. APD-based PET detector for simultaneous PET/MR imaging. *Nuclear Instruments and Methods in Physics Research, Section A: Accelerators, Spectrometers, Detectors and Associated Equipment*, 569:301–305, 2006.

[Ham] Hamamatsu Photon K K. Picosecond light pulser PLP-10.

[Ham10] Hamamatsu Photon K K. MPPC S10984/S10985 series, 2010.

[Ham14] Hamamatsu. MPPC S12572-025, -050, -100C/P Datasheet. Technical report, 2014.

[HBTV99] E M Haacke, R W Brown, M R Thompson, and R Venkatesan. *Magnetic Resonance Imaging*, volume 5. June 1999.

[HCJ+10] Key Jo Hong, Yong Choi, Jin Ho Jung, Jihoon Kang, Wei Hu, Hyun Keong Lim, Yoonsuk Huh, Sangsu Kim, Ji Woong Jung, Kyu Bom Kim, Myung Sung Song, and Hyun Wook Park. MR insertable brain PET using tileable GAPD arrays. In *IEEE Nuclear Science Symposium Conference Record*, pages 2016–2019, 2010.

[HKK+12] Seong Jong Hong, Han Gyoo Kang, Guen Bae Ko, In Chan Song, June-Tak Rhee, and Jae Sung Lee. SiPM-PET with a short optical fiber bundle for simultaneous PET-MR imaging, 2012.

[Hoh12] Melanie Hohberg. *Monte Carlo Simualtion Studies and Image Reconstructions Methods for a Small Animal PET Scanner*. Phd thesis, TU München, 2012.

[ISS+13] Joanna Iwanowska, Lukasz Swiderski, Tomasz Szczesniak, Pawel Sibczynski, Marek Moszynski, Martyna Grodzicka, Kei Kamada, Kousuke Tsutsumi, Yoshiyuki Usuki, Takayuki Yanagida, and

Akira Yoshikawa. Performance of cerium-doped Gd3Al2Ga 3O12 (GAGG:Ce) scintillator in gamma-ray spectrometry. *Nuclear Instruments and Methods in Physics Research, Section A: Accelerators, Spectrometers, Detectors and Associated Equipment*, 712:34–40, 2013.

[JMW+12] M. a. Janich, M. I. Menzel, F. Wiesinger, E. Weidl, O. Khegai, J. H. Ardenkjaer-Larsen, S. J. Glaser, A. Haase, R. F. Schulte, and M. Schwaiger. Effects of pyruvate dose on in vivo metabolism and quantification of hyperpolarized 13C spectra. *NMR in Biomedicine*, 25(January 2011):142–151, 2012.

[Kam15] Kei Kamada. Private Communications, 2015.

[KCH+11] Jihoon Kang, Yong Choi, Key Jo Hong, Wei Hu, Jin Ho Jung, Yoonsuk Huh, and Byung-Tae Kim. A small animal PET based on GAPDs and charge signal transmission approach for hybrid PET-MR imaging, 2011.

[KETa] KETEK GmbH. KETEK PM1150 Datasheet. Technical report, Munich, GERMANY.

[KETb] KETEK GmbH. KETEK SiPM Technology.

[KETc] KETEK GmbH. Private Communications.

[Kno10] Glenn F Knoll. *Radiation Detection and Measurement, Fourth Edition*. New York, NY, 4th ed. edition, 2010.

[Kon14] Koninklijke Philips N.V. Philips Vereos PET/CT: Truly digital PET imaging, 2014.

[KPN+12] Kei Kamada, Petr Prusa, Martin Nikl, Claudio Piemonte, Alessandro Tarolli, Takayuki Yanagida, Takanori Endo, Kousuke Tsutumi, and Akira Yoshikawa. 2-inch size crystal growth of Ce:Gd3Al2Ga3O12 with various Ce concentration and their scintillation properties. In *2012 IEEE Nuclear Science Symposium and Medical Imaging Conference Record (NSS/MIC)*, pages 1698–1701. IEEE, October 2012.

[KPS+10] Tilman Küstner, Peter Pedron, Jasmine Schirmer, Josef Weidendorfer, and Sibylle I Ziegler. Fast System Matrix Generation Using the Detector Response Function Model on Fermi GPUs, 2010.

[Kuc11] Wojtek Kucewicz. Review of ASIC developments for SiPM signal readout. *Industria-academy matching event on SiPM and ...*, 2011.

[KWH+12] Armin Kolb, Hans F. Wehrl, Matthias Hofmann, Martin S. Judenhofer, Lars Eriksson, Ralf Ladebeck, Matthias P. Lichy, Larry Byars, Christian Michel, Heinz Peter Schlemmer, Matthias Schmand,

Claus D. Claussen, Vesna Sossi, and Bernd J. Pichler. Technical performance evaluation of a human brain PET/MRI system. *European Radiology*, 22:1776–1788, 2012.

[KWS09] Tilman Küstner, Josef Weidendorfer, and Jasmine Schirmer. *Parallel MLEM on Multicore Architectures*, volume 5544 of *Lecture Notes in Computer Science*. Springer Berlin Heidelberg, Berlin, Heidelberg, 2009.

[KYE+11] Kei Kamada, Takayuki Yanagida, Takanori Endo, Kousuke Tsutumi, Yoshiyuki Usuki, Martin Nikl, Yutaka Fujimoto, and Akira Yoshikawa. 2-inch size single crystal growth and scintillation properties of new scintillator; Ce:Gd3Al2Ga3O12. In *2011 IEEE Nuclear Science Symposium Conference Record*, pages 1927–1929. IEEE, October 2011.

[KZ11] Magdy M. Khalil and Pat Zanzonico. *Basic Sciences of Nuclear Medicine*, volume 38. 2011.

[LAG+06] P Lecoq, A Annenkov, A Gektin, M Korzhik, and C Pedrini. *Inorganic Scintillators for Detectors Systems*. 2006.

[LH08] TC Larason and JM Houston. Spectroradiometric detector measurements: ultraviolet, visible, and near-infrared detectors for spectral power. *NIST Special Publication*, 41, 2008.

[Man10] Alexander. B Mann. *Sampling ADC Based Data Acquisition for Positron Emission Tomography*. PhD thesis, 2010.

[MC13] Shingo Mandai and Edoardo Charbon. A 4 4 416 digital SiPM array with 192 TDCs for multiple high-resolution timestamp acquisition. *Journal of Instrumentation*, 8:P05024–P05024, 2013.

[McI66] R.J. McIntyre. Multiplication noise in uniform avalanche diodes. *IEEE Transactions on Electron Devices*, 13(1):164–168, January 1966.

[METV12] R Marcinkowski, S Espa, H Thoen, and S Vandenberghe. Performance of Digital Silicon Photomultipliers for Time of Flight PET Scanners. pages 2825–2829, 2012.

[MFL+15] Claudia T Mendler, Lars Friedrich, Iina Laitinen, Martin Schlapschy, Markus Schwaiger, Hans-Jürgen Wester, and Arne Skerra. High contrast tumor imaging with radio-labeled antibody Fab fragments tailored for optimized pharmacokinetics via PASylation. *mAbs*, 7(1):96–109, 2015.

[MGJ+14] Michael Miller, Jerome Griesmer, David Jordan, Thomas Laurence, Raymond Muzic, Manoj Narayanan, Deepa Natarajamani, Kuan-Hao Su, and Sharon Wang. Initial characterization of a prototype digital photon counting PET system. *Society of Nuclear Medicine Annual Meeting Abstracts*, 55:658, 2014.

[MJC14] Shingo Mandai, Vishwas Jain, and Edoardo Charbon. A 780 800 μm2 multichannel digital silicon photomultiplier with column-parallel time-to-digital converter and basic characterization. *IEEE Transactions on Nuclear Science*, 61(1):44–52, 2014.

[MPP+05] D.P. McElroy, Wendelin Pimpl, B.J. Pichler, Magdalena Rafecas, T. Schuler, and S.I. Ziegler. Characterization and readout of MADPET-II detector modules: validation of a unique design concept for high resolution small animal PET. *IEEE Transactions on Nuclear Science*, 52(1):199–204, February 2005.

[MS05] D. Motta and S. Schönert. Optical properties of bialkali photocathodes. *Nuclear Instruments and Methods in Physics Research, Section A: Accelerators, Spectrometers, Detectors and Associated Equipment*, 539:217–235, 2005.

[MSJ+11] Sri Harsha Maramraju, S David Smith, Sachin S Junnarkar, Daniela Schulz, Sean Stoll, Bosky Ravindranath, Martin L Purschke, Sergio Rescia, Sudeepti Southekal, Jean-François Pratte, Paul Vaska, Craig L Woody, and David J Schlyer. Small animal simultaneous PET/MRI: initial experiences in a 9.4 T microMRI. *Physics in medicine and biology*, 56:2459–2480, 2011.

[Mus07] Y Musienko. Tests and performance of multi-pixel Geiger mode APD's and APD's for the CMS ECAL. *PD07 Workshop Kobe*, 2007.

[Mus11] Yuri Musienko. New photo-sensors for the CMS HCAL upgrade, 2011.

[OOY+07] H Oide, H Otono, S Yamashita, T Yoshioka, H Hano, and T Suehiro. Study of afterpulsing of MPPC with waveform analysis. 2007.

[Ori14a] Tadashi Orita. Private Communications, 2014.

[Ori14b] Tadashi Orita. *Study on a time-width signal processing method of radiation signals*. Phd thesis, University of Tokyo, 2014.

[OSA72] W.G. Oldham, R.R. Samuelson, and P. Antognetti. Triggering phenomena in avalanche diodes. *IEEE Transactions on Electron Devices*, 19, 1972.

[OST12] T Orita, K Shimazoe, and H Takahashi. Dynamic time-over-threshold method for multi-channel APD based gamma-ray detectors. In *2012 IEEE Nuclear Science Symposium and Medical Imaging Conference Record (NSS/MIC)*, pages 824–826. IEEE, October 2012.

[PBB+01] Bernd J Pichler, Florian Bernecker, Guido Böning, Magdalena Rafecas, Wendelin Pimpl, Markus Schwaiger, Eckart Lorenz, and Sibylle I Ziegler. A 4 8 APD array, consisting of two monolithic silicon wafers, coupled to a 32-channel LSO matrix for high-resolution PET. In *IEEE Transactions on Nuclear Science*, volume 48, pages 1391–1396, 2001.

[PBB+07] Claudio Piemonte, Roberto Battiston, Maurizio Boscardin, Gian-Franco Dalla Betta, Alberto Del Guerra, Nicoleta Dinu, Alberto Pozza, and Nicola Zorzi. Characterization of the First Prototypes of Silicon Photomultiplier Fabricated at ITC-irst. *IEEE Transactions on Nuclear Science*, 54(1):236–244, February 2007.

[PBL+98] B Pichler, C Boning, E Lorenz, R Mirzoyan, W Pimpl, M Schwaiger, and S.I. Ziegler. Studies with a prototype high resolution PET scanner based on LSO-APD modules. *IEEE Transactions on Nuclear Science*, 45(3):1298–1302, June 1998.

[PCS+] C A Pelizzari, G T Chen, D R Spelbring, R R Weichselbaum, and C T Chen. Accurate three-dimensional registration of CT, PET, and/or MR images of the brain. *Journal of computer assisted tomography*, 13:20–26.

[PFG+13] Claudio Piemonte, Alessandro Ferri, Alberto Gola, Tiziana Pro, Nicola Serra, Alessandro Tarolli, and Nicola Zorzi. Characterization of the First FBK High-Density Cell Silicon Photomultiplier Technology. *IEEE Transactions on Electron Devices*, 60(8):2567–2573, August 2013.

[Phi12] Philips Digital Photon Counting. The digital Silicon Photomultiplier Product Leaflet., 2012.

[PLZ+10] Ilwoo Park, Peder E Z Larson, Matthew L. Zierhut, Simon Hu, Robert Bok, Tomoko Ozawa, John Kurhanewicz, Daniel B. Vigneron, Scott R. VandenBerg, C. David James, and Sarah J. Nelson. Hyperpolarized 13C magnetic resonance metabolic imaging: Application to brain tumors. *Neuro-Oncology*, 12(2):133–144, 2010.

[PSV+12a] J Pulko, F R Schneider, A Velroyen, D Renker, and S I Ziegler. A Monte-Carlo model of a SiPM coupled to a scintillating crystal. *Journal of Instrumentation*, 7(02):P02009–P02009, February 2012.

[PSV+12b] J Pulko, F R Schneider, A Velroyen, D Renker, and S I Ziegler. A Monte-Carlo model of a SiPM coupled to a scintillating crystal. *Journal of Instrumentation*, 7(02):P02009–P02009, February 2012.

[Pul12] Jozef Pulko. *A Monte-Carlo Model of a Silicon Photomultiplier*. PhD thesis, Technische Universität München, 2012.

[RBP+03] M Rafecas, G Böning, B J Pichler, E Lorenz, M Schwaiger, and S I Ziegler. Inter-crystal scatter in a dual layer, high resolution LSO-APD positron emission tomograph. *Physics in medicine and biology*, 48:821–848, 2003.

[Ren06] D. Renker. Geiger-mode avalanche photodiodes, history, properties and problems. *Nuclear Instruments and Methods in Physics Research Section A: Accelerators, Spectrometers, Detectors and Associated Equipment*, 567(1):48–56, November 2006.

[Ren09] D Renker. New developments on photosensors for particle physics. *Nuclear Instruments and Methods in Physics Research Section A: Accelerators, Spectrometers, Detectors and Associated Equipment*, 598(1):207–212, January 2009.

[RL09] D Renker and E Lorenz. Advances in solid state photon detectors. *Journal of Instrumentation*, 4(04):P04004–P04004, April 2009.

[ROO11] ROOT. A data analysis framework, 2011.

[RSB07] Osman Ratib, Markus Schwaiger, and Thomas Beyer. Atlas of PET/CT Imaging in Oncology, 2007.

[RVAE13] F R Rannou, N Vega-Acevedo, and Z El Bitar. A parallel computational model for GATE simulations. *Computer methods and programs in biomedicine*, August 2013.

[Sad98] Z Sadygov. Avalanche Detector, 1998.

[Sai09] Saint-Gobain Crystals. Scintillation Products Technical Note, 2009.

[Sai14] Saint-Gobain Crystals. Efficiency Calculations for Selected Scintillators. *Document from Saint-Gobain website*, 2014.

[SBA+08] Raffaele Scafe, Paolo Bennati, Paolo Auer, Luigi La Porta, Fabrizio Pisacane, Maria Nerina Cinti, Rosanna Pellegrini, Giuseppe De Vincentis, Gennaro Conte, and Roberto Pani. Multi-printed inkjet phantoms for radionuclide molecular imaging. In *Nuclear Science Symposium Conference Record, 2008. NSS '08. IEEE*, pages 1081–1087, 2008.

[SBP+05] V Sossi, K R Buckley, P Piccioni, A Rahmim, M.-L. Camborde, E Strome, S Lapi, and T J Ruth. Printed sources for positron emission tomography (PET). *Nuclear Science, IEEE Transactions on*, 52(1):114–118, 2005.

[SCF+97] Yiping Shao, Simon R Cherry, Keyvan Farahani, Ken Meadors, Stefan Siegel, Robert W Silverman, and Paul K Marsden. Simultaneous PET and MR imaging. *Physics in Medicine and Biology*, 42(10):1965–1970, October 1997.

[Sch09] F R Schneider. Setup and Commissioning of a Positron Emission Tomograph for a Student's Advanced Laboratory Course. Master's thesis, TU München, 2009.

[Sch11a] Florian Roland Schneider. 2010-IEEE-NSSMIC-MADPET3-Poster-A4.pdf, 2011.

[Sch11b] Ralf Schulze. The PDPC Technology Evaluation Kit, 2011.

[Sch13] Ralf Schulze. PDPC-TEK User Manual v0.19, 2013.

[Sch15] Florian Roland Schneider. *Development of a PET Insert for Simultaneous Preclinical PET / MR at 7 T*. Phd thesis, submitted 18. june 2015, Technische Universität München, 2015.

[Sen13] Sensl. B Series. Fast, Blue-Sensitive Silicon Photomultiplier Sensors Datasheet. Technical report, 2013.

[SG04] Saint-Gobain. PreLude 420 Datasheet, 2004.

[SGS+14] F R Schneider, T R Ganka, G Seker, E Engelmann, D Renker, S Paul, W Hansch, and S I Ziegler. Characterization of blue sensitive 3 mm x 3 mm SiPMs and their use in PET. *Journal of Instrumentation*, 9(07):P07027–P07027, July 2014.

[SgSJ+14] Lise Vejby Sø gaard, Franz Schilling, Martin a. Janich, Marion I. Menzel, and Jan Henrik Ardenkjæ r Larsen. In vivo measurement of apparent diffusion coefficients of hyperpolarized 13C-labeled metabolites. *NMR in Biomedicine*, 27(January):561–569, 2014.

[Sha] Shapeways. Strong and Flexible Plastics.

[SKM+13] T. Szczesniak, M. Kapusta, M. Moszynski, M Grodzicka, M. Szawlowski, D Wolski, J Baszak, and N Zhang. MPPC arrays in PET detectors with LSO and BGO scintillators. *IEEE Transactions on Nuclear Science*, 60(3):1533–1540, 2013.

[SMK+10] Florian R Schneider, Alexander B Mann, Igor Konorov, Stephan Paul, Gaspar Delso, and Sibylle I Ziegler. First Performance Studies of a Prototype SiPM PET Scanner. Technical report, 2010.

[SMK+11] Florian R Schneider, Alexander B Mann, Igor Konorov, Gaspar Delso, Stephan Paul, and Sibylle I Ziegler. A Positron Emission Tomograph Based on LSO-APD Modules with a Sampling ADC Read-out System for a Students' Advanced Laboratory Course. *Zeitschrift fur medizinische Physik*, October 2011.

[SMKD11] FR Schneider, AB Mann, Igor Konorov, and Gaspar Delso. A Positron Emission Tomograph Based on LSO-APD Modules with a Sampling ADC Read-out System for a Students' Advanced Laboratory Course. 2011.

[SMO+07] V C Spanoudaki, a B Mann, a N Otte, I Konorov, I Torres-Espallardo, S Paul, and S I Ziegler. Use of single photon counting detector arrays in combined PET/MR: Characterization of LYSO-SiPM detector modules and comparison with a LSO-APD detector. *Journal of Instrumentation*, 2(12):P12002–P12002, December 2007.

[SOPA+13] N. Jon Shah, Ana Maria Oros-Peusquens, Jorge Arrubla, Ke Zhang, Tracy Warbrick, Jörg Mauler, Kaveh Vahedipour, Sandro Romanzetti, Jörg Felder, Avdo Celik, Elena Rota-Kops, Hidehiro Iida, Karl Josef Langen, Hans Herzog, and Irene Neuner. Advances in multimodal neuroimaging: Hybrid MR-PET and MR-PET-EEG at 3 T and 9.4 T. *Journal of Magnetic Resonance*, 229:101–115, 2013.

[Spa07] Virginia Charalampous Spanoudaki. *Development and Performance Studies of a Small Animal Positron Emission Tomograph with Individual Crystal Readout and Depth of Interaction Information and Studies of Novel Detector Technologies in Medical Imaging*. PhD thesis, Technische Universität München, 2007.

[SPS+08] Heinz-Peter W Schlemmer, Bernd J Pichler, Matthias Schmand, Ziad Burbar, Christian Michel, Ralf Ladebeck, Kirstin Jattke, David Townsend, Claude Nahmias, Pradeep K Jacob, Wolf-Dieter Heiss, and Claus D Claussen. Simultaneous MR/PET imaging of the human brain: feasibility study. *Radiology*, 248(3):1028–1035, 2008.

[SSD+03] D Strul, R B Slates, M Dahlbom, S R Cherry, and P K Marsden. An improved analytical detector response function model for multilayer small-diameter PET scanners. *Physics in Medicine and Biology*, 48(8):979–994, April 2003.

[SSS+14] Florian R Schneider, Gizem Seker, Kenji Shimazoe, Tadashi Orita, Hiroyuki Takahashi, Stephan Paul, and Sibylle I Ziegler. MADPET4

- A MRI compatible Dual Layer PET Insert First Tests with Two Modules. *IEEE NSS/MIC*, 2014.

[SSSS+13] Ian Somlai-Schweiger, Florian R Schneider, Kenji Shimazoe, Hiroyuki Takahashi, and Sibylle I Ziegler. Performance Analysis of Digital Silicon Photomultipliers for PET. In *IEEE NSS MIC*, Seoul, 2013.

[SSSSZ15] F R Schneider, K Shimazoe, Ian Somlai-Schweiger, and S I Ziegler. A PET detector prototype based on digital SiPMs and GAGG scintillators. *Phys. Med. Biol.*, 60:1667, 2015.

[SSSZ15] I. Somlai-Schweiger, F.R. Schneider, and S.I. Ziegler. Performance analysis of digital silicon photomultipliers for PET. *Journal of Instrumentation*, 10:P05005–P05005, 2015.

[SV82] L A Shepp and Y Vardi. Maximum likelihood reconstruction for emission tomography. *IEEE transactions on medical imaging*, 1(2):113–22, January 1982.

[SvDV+12] Stefan Seifert, Herman T. van Dam, Ruud Vinke, Peter Dendooven, Herbert Lohner, Freek J. Beekman, and Dennis R. Schaart. A Comprehensive Model to Predict the Timing Resolution of SiPM-Based Scintillation Detectors: Theory and Experimental Validation. *IEEE Transactions on Nuclear Science*, 59(1):190–204, February 2012.

[SWT+11] K. Shimazoe, Y. Wang, H. Takahashi, K. Kamada, M. Yoshino, J. Kataoka, Y. Yamaya, T. Yanagida, A. Yoshikawa, and K. Kumagai. Time over Threshold based digital animal PET (TODPET). In *2011 IEEE Nuclear Science Symposium Conference Record*, pages 3267–3271. IEEE, October 2011.

[TERS+08] I Torres-Espallardo, M Rafecas, V Spanoudaki, D P McElroy, and S I Ziegler. Effect of inter-crystal scatter on estimation methods for random coincidences and subsequent correction. *Physics in medicine and biology*, 53(9):2391–411, May 2008.

[TGGM06] Stefaan Tavernier, Alexander Gektin, Boris Grinyov, and William W Moses. *Radiation Detectors for Medical Applications*. Springer Netherlands, 2006.

[TLB+15] M.-A. Tetrault, E. Desaulniers Lamy, A Boisvert, C Thibaudeau, M Kanoun, F Dubois, R Fontaine, and J.-F. Pratte. Real-Time Discrete SPAD Array Readout Architecture for Time of Flight PET. *IEEE Transactions on Nuclear Science*, pages 1–1, 2015.

[Tow09] David W Townsend. Combined PET / CT : the historical perspective. *Seminars in Ultrasound, CT, and MRI*, 29(4):232–235, 2009.

[VBD+11] A Vacheret, G.J. Barker, M Dziewiecki, P Guzowski, M.D. Haigh, B Hartfiel, A Izmaylov, W Johnston, M Khabibullin, A Khotjantsev, Yu. Kudenko, R Kurjata, T Kutter, T Lindner, P Masliah, J Marzec, O Mineev, Yu. Musienko, S Oser, F. Retire, R.O. Salih, A Shaikhiev, L.F. Thompson, M.A. Ward, R.J. Wilson, N Yershov, K Zaremba, and M Ziembicki. Characterization and simulation of the response of Multi-Pixel Photon Counters to low light levels. *Nuclear Instruments and Methods in Physics Research Section A: Accelerators, Spectrometers, Detectors and Associated Equipment*, 656(1):69–83, November 2011.

[VBTM03] Peter E Valk, Dale L Bailey, David W Townsend, and Michael N Maisey. *Positron Emission Tomography: Basic Science and Clinical Practice*. Springer, London, 2003.

[Vel10] A Velroyen. Development of a Novel Detector Module for PET/MR Imaging Based on SiPMs and Fast Scintillation Crystals. Master's thesis, LMU München, Klinikum rechts der Isar der TU München, 2010.

[VM15] Stefaan Vandenberghe and Paul K Marsden. PET-MRI: a review of challenges and solutions in the development of integrated multimodality imaging. *Physics in Medicine and Biology*, 60:R115–R154, 2015.

[VVS+11] Sergey Vinogradov, Tatiana Vinogradova, Vitaly Shubin, Dmitry Shushakov, and Constantin Sitarsky. Efficiency of solid state photomultipliers in photon number resolution. In *IEEE Transactions on Nuclear Science*, volume 58, pages 9–16, 2011.

[Wie11] Florian Wiest. SiPM Developments at KETEK KETEK SiPM Technology and Device Characteristic. *HEPTech Workshop*, 2011.

[WWD+13] Jakob Wehner, Bjoern Weissler, Peter Dueppenbecker, Pierre Gebhardt, David Schug, Walter Ruetten, Fabian Kiessling, and Volkmar Schulz. PET/MRI insert using digital SiPMs: Investigation of MR-compatibility. *Nuclear Instruments and Methods in Physics Research Section A: Accelerators, Spectrometers, Detectors and Associated Equipment*, pages 1–6, September 2013.

[WWD+14] Jakob Wehner, Bjoern Weissler, Peter Dueppenbecker, Pierre Gebhardt, David Schug, Walter Ruetten, Fabian Kiessling, and Volkmar Schulz. PET/MRI insert using digital SiPMs: Investigation of MR-compatibility. *Nuclear Instruments and Methods in Physics Research, Section A: Accelerators, Spectrometers, Detectors and Associated Equipment*, 734:116–121, 2014.

[YCN13] A. Yoshikawa, V. Chani, and M. Nikl. Czochralski growth and properties of scintillating crystals. *Acta Physica Polonica A*, 124(2):250–264, 2013.

[YKK+12] H. S. Yoon, G. B. Ko, S. I. Kwon, C. M. Lee, M. Ito, I. Chan Song, D. S. Lee, S. J. Hong, and J. S. Lee. Initial Results of Simultaneous PET/MRI Experiments with an MRI-Compatible Silicon Photomultiplier PET Scanner, 2012.

[YWW+11] Seiichi Yamamoto, Tadashi Watabe, Hiroshi Watabe, Masaaki Aoki, Eiji Sugiyama, Masao Imaizumi, Yasukazu Kanai, Eku Shimosegawa, and Jun Hatazawa. Simultaneous imaging using Si-PM-based PET and MRI for development of an integrated PET/MRI system, 2011.

[YYD+13] Jung Yeol Yeom, Seiichi Yamamoto, Stephen E. Derenzo, Virginia Ch. Spanoudaki, Kei Kamada, Takanori Endo, and Craig S. Levin. First Performance Results of Ce:GAGG Scintillation Crystals With Silicon Photomultipliers. *IEEE Transactions on Nuclear Science*, 60(2):988–992, April 2013.

[Zai14] Habib Zaidi. *Molecular Imaging of Small Animals*. 2014.

[Zie05] Sibylle I. Ziegler. Positron emission tomography: Principles, technology, and recent developments, 2005.

[ZMZ07] Liyuan Zhang, Rihua Mao, and Ren Yuan Zhu. Emission spectra of LSO and LYSO crystals excited by UV light, X-ray and gamma-ray. In *IEEE Nuclear Science Symposium Conference Record*, volume 6, pages 4574–4580, 2007.

[ZOM+11] H Zaidi, N Ojha, M Morich, J Griesmer, Z Hu, P Maniawski, O Ratib, D Izquierdo-Garcia, Z a Fayad, and L Shao. Design and performance evaluation of a whole-body Ingenuity TF PET-MRI system. *Physics in medicine and biology*, 56(10):3091–106, May 2011.

[ZPB+01] Sibylle I. Ziegler, Bernd J. Pichler, Guido Boening, Magdalena Rafecas, Wendelin Pimpl, Eckart Lorenz, Norbert Schmitz, and Markus Schwaiger. A prototype high-resolution animal positron tomograph with avalanche photodiode arrays and LSO crystals. *European Journal of Nuclear Medicine and Molecular Imaging*, 28(2):136–143, February 2001.

[ZSW+13] M Zhuravleva, L Stand, H Wei, C Hobbs, L A Boatner, Senior Member, J O Ramey, K Shah, A Burger, E Rowe, P Bhattacharya, E Tupitsyn, C L Melcher, Senior Member, and A Scintillator Samples. Hygroscopicity evaluation of halide scintillators. In *2013 IEEE*

Nuclear Science Symposium and Medical Imaging Conference (2013 NSS/MIC), pages 1–5, 2013.

Acknowledgments

First of all I thank Prof. Sibylle Ziegler for the interesting topic, her supervision, her advices, mentoring and continuous support during this eventful journey. I am grateful for her open mind, that she let me realize my own ideas and do research in an autonomous way. This was extremely important for me. Always having her backup and her valuable feedback allowed me to develop myself. Many thanks for the opportunity to travel to many worldwide conferences which was great to extend my knowledge and horizon. She truly enabled me to improve professionally and personally.
Sincere thanks also to Prof. Stephan Paul for the opportunity to work and educate myself at his chair since the beginning of 2006. He not only prepared the ground for me to do experimental research on PET, but also I could meet awesome people and make friends at E18 which formed me as a scientist. He was always open to new ideas and I always had his support for my projects.
I am grateful to both for the fruitful and uncomplicated interdisciplinary collaboration between their departments.

I am also indebted to my bright mentors Alexander Mann and Dieter Renker. Each of them supported me with all his knowledge and ideas. Alexander was a great supervisor already when I started with PET and he encouraged me to go on in this field. With Dieter I was lucky to have the best expert about solid state photodetectors as a teacher. He also was at hand with the right advices and help for me at the right times.

Arigatou to Prof. Kenji Shimazoe from University of Tokyo. For everything you did for me, for always sharing your knowledge and the uncomplicated co-working. For the great time we spent at many different places all over the world.

Thanks to my closest colleagues during the last years Jožef Pulko, Melanie Hohberg, Ian Somlai-Schweiger and Jorge Cabello. They all contributed with their discussions and valuable feedback and it was always an exciting pleasure to work with them in our common projects.

For all their support, shared knowledge, close collaboration, always open minded discussions and the positive outcome from the work together, I thank Thomas Ganka, Florian Wiest and Werner Hartinger from KETEK.

Muchas gracias to José Gardiazabal for his valuable input, unbiased and fresh view to things, brainstorming with great ideas and helping me out.

Merci to Rupert Trager, for his support with any hardware I needed, trust, talking the same language and our fruitful discussions.

For the open and reliable cooperation also beyond electronics, I thank Igor Konorov and Martin Losekamm.

More than grateful I am to my family. Especially to my everything Gizem, who makes me better in every aspect, makes me proud and completes me.